

We are IntechOpen, the world's leading publisher of Open Access books Built by scientists, for scientists

6,900

Open access books available

186,000

International authors and editors

200M

Downloads

Our authors are among the

154

Countries delivered to

TOP 1%

most cited scientists

12.2%

Contributors from top 500 universities



WEB OF SCIENCE™

Selection of our books indexed in the Book Citation Index
in Web of Science™ Core Collection (BKCI)

Interested in publishing with us?
Contact book.department@intechopen.com

Numbers displayed above are based on latest data collected.
For more information visit www.intechopen.com



Geometric and Spectroscopic Properties of Carbon Nanotubes and Boron Nitride Nanotubes

Metin Aydin¹ and Daniel L. Akins²

¹*Department of Chemistry, Faculty of Art and Sciences,
Ondokuz Mayıs University, Samsun*

²*Center for Analysis of Structures and Interfaces (CASI), Department of Chemistry,
The City College of The City University of New York, New York*

¹Turkey

²USA

1. Introduction

Carbon, the first element in Group 4A, is a nonmetal and has $1s^2 2s^2 2p^2$ electronic configuration, in which four valence electrons allow it to form a number of hybridized atomic orbitals. Therefore, carbon atoms in the elemental substances bonds to each other covalently by the sharing of electron pairs, in which the covalent bonds have directional properties. This in turn provides carbon capability to adapt into various molecular and crystalline structures. The natures of these bonds underlie the varied chemical properties and physical properties of the carbon allotropes. Pure carbon-based materials are not only diamonds (as shown in Figure 1.1a), and graphite (Figure 1.1b) but also fullerenes (Figure 1.1c), carbon nanotubes (CNT) (see Figure 1.2), and amorphous carbon. These allotropes have been considered some of the most important materials in nanotechnology.

The unique properties of single-walled carbon nanotubes originate from their distinctive structure, which is composed of C-C bonds more closely related to that in graphite rather than in diamond. Specifically, despite the fact that diamond has a coordination number of four with sp^3 hybridization, the sp^2 hybridization in graphite links carbon atoms in a two-dimensional (2D) layer of hexagons that lead to each layer in graphite being a planar structure in the ideal cases. In the latter case, each carbon atom contributes three electrons to the sigma bonds within the plane and has one electron left in the p_z orbitals. These p_z orbitals cooperatively allow the electron to delocalize over the entire plane, giving rise to a molecular orbital that is perpendicular to the plane of graphene, which allows the fourth valence electron in carbon atoms to move freely on the plane. Within the layers, the carbon-carbon bond distance is similar to the bond length in benzene (the carbon atoms are strongly bound to each other and carbon-carbon distance is about 0.14 nm), leading to a very large inplane value for Young's modulus. The distance between layers (about 0.34 nm) is too large to permit significant orbital overlap; layers are bounded to each other mainly by weak long-range Van der Waals type interactions. The weak interlayer coupling gives graphite the

property of a seemingly very soft material, the property that allows using graphite in a pen for writing. In diamond, all valence electrons are localized around the carbon atoms. These structural differences produce profound effects on the electrical properties of graphite and diamond: graphite is a semimetal, and diamond is an insulator with a band gap around 6 eV. Since carbon nanotubes' (CNTs) discovery in 1991 [1], they have received extensive attention due to many unique physical and chemical properties. Considering that CNTs are the subject of one of the most important areas of research in nanotechnology due, to their unique properties and potential for precious profitable applications – varying from electronics to chemical process control – a massive amount of effort has been invested on investigation of nanotubes' active components. Indeed, their discovery has resulted in a variety of technological uses, namely, nanotechnology, functional nanodevices, [2,3,4] materials science, heat conduction, [5,6] electronics, [7,8] molecular memories,[9] optics, [10,11,12] unique electrical properties, transistors, electrically excited single-molecule light sources, [13,14,15,16] DNA functionalization, [17,18] high-performance adsorbent electrode material for energy-storage device, [19] and proteins.[20,21] Most of the research has been invested to understand their optical and structural properties as well as the development and advancement of carbon nanotubes.

Carbon nanotubes (CNTs) are in the structural family of fullerene. They are molecules composed entirely of carbon atoms. The carbon atoms are usually arranged in a hexagonal pattern, bonded together with extremely strong covalent bonds. A carbon nanotube bundle can be visualized as a finite number of carbon graphite shells arranged around a hollow center axis with a constant spacing of around 0.34 nm, with a tubular diameter normally ranging up to several nanometers from 1.4 nm, and with lengths up to several microns. This number of graphite shells is the basis for the key division in carbon nanotubes, such as single-walled nanotubes (SWNTs) and multi-walled nanotubes (MWNTs). The concept of either single-walled or multi-walled carbon nanotubes is important since the properties change significantly with respect to each other. One of the goals of the research focused on CNTs is to understand how well electrons flow through carbon nanotubes. As it turns out, many of the results were inconsistent.

In general, multi-walled nanotubes have individually different properties, even if they are made under the same experimental conditions. Because of uncontrollable inconsistencies between each individual nanotube, it is difficult to construct a consistent theory of electric flow because of structural defects. In general, the amounts of structural defects in any tube significantly affect the flow of electrons in any other CNT. These defects are not yet fully understood, therefore, many investigators have investigated how to eradicate these defects, so as to obtain the highest performance for nanotube conductance. Furthermore, in optics, strong Coulomb effects [14,15,16,22,23,24] in carbon nanotubes bring about formation of the exciton states that are allegedly a "bright" (allowed one-photon electronic transition) and "dark" (forbidden one-photon transition), and dramatically decrease the efficiency of one-photon light emission via trapping of the carriers by "dark" excitons [13,22, 25,26,27,28,33]. However, a proper use of these "bright" and "dark" exciton states, which have distinctively different recombination times may benefit the use of which quantum coherence [29,30,31,32] and multiphoton schemes of excitation potentially not only allowing one to efficiently manipulate the dark states, but may also create conditions for efficient light generation in different frequency regions; i.e., producing "slow" or "fast" light, thus implementing

quantum light storage media with a negative refractive index,[33,34] and other quantum-optical regimes [33,35,36]. Possible quantum-optical carbon nanotube devices have a potential for suitable performance at elevated temperatures, because the binding energies of excitons in single-walled nanotubes (SWCNTs) are up to hundreds of meV [23, 24, 16, 37, 38, 39, 40].

CNTs are not only used for electron transport, but also used as an ideal carbon fiber [41] and as a storage units for hydrogen for use in hydrogen fuel cells,[41,42]. From a mechanical perspective, the strength of CNTs illustrates their material properties, where the majority defects can be neglected, that make it possible to view each nanotube as an ideal carbon fiber. In nature, the strong C-C bonds in CNTs are some of the strongest bonds, thus making a carbon nanotube one of the strongest materials in nature. For instance, for an ideal carbon nanotube, Young modulus of 1000 GPa and tensile strength of 60 GPa have been measured from individual structure, which is an order of magnitude higher than ordinary engineering plastics. High electrical and thermal conductivity have also been determined experimentally, [43,44,45,46], with value close to or better than metals. With such a combination of properties and a product form compatible with modern polymer processing technologies, the possibilities of creating new engineered materials are enormous [48][47]. The use of carbon nanotubes for antistatic and conductive applications in polymers is already a commercial reality and is growing in sectors such as electronics and the automotive industry. The loading for achieving electrical percolation with multi-wall carbon nanotubes (MWCNTs) may be lower than with conductive carbon black grades.

Carbon nanotubes can be synthesized by various methods, including arc-discharge, laser ablation, and chemical vapor deposition [24]. In the arc-discharge method, carbon atoms are evaporated by a plasma of helium gas ignited by high currents passing through a carbon anode and cathode assembly. The carbon atoms nucleate on a metal catalyst and grow to several micrometers in length. A similar principle is adopted in the laser ablation method where intense laser pulses are used to ablate a carbon target containing metal catalysts. During laser ablation, a flow of inert gas is passed through the growth chamber to carry the nanotube downstream to a cold collection finger. The produced SWCNTs mostly crystallize in the form of ropes having tens of individual nanotubes close-packed into hexagons via Van der Waals interactions. In chemical vapor deposition, a flowing hydrocarbon gas is decomposed by metal catalysts. The precipitation of carbon from the saturated phase in metal particles leads to the formation of a tubular carbon solid.

Boron nitride nanotubes (BNNTs) are among the nanocomposites, which have been synthesized successfully [48,49,50] following the syntheses of carbon nanotubes (CNTs). The electronic properties of boron nitride nanotubes differ from carbon nanotubes. While carbon nanotubes can be either metallic or semiconducting, depending on their chirality and the diameter [51], all boron nitride nanotubes (BNNTs) are found to be semiconducting materials having the large band gaps[53], with band gaps only weakly depending on the diameter, chirality, and the number of the walls of the tube. Because of their semiconducting behavior, BNNTs are very interesting materials for application in nanoscale devices and are considered remarkable alternatives to CNTs [52,53]. Modification of the electronic properties of nanotubes by doping and functionalization is also an important subject for nano-devices. The doped nanotubes may exhibit a dramatic change with regard to the isolated nanotube. Furthermore, because of the strong interactions between electrons and holes in BNNTs [54,55], the excitonic effects in are

more important than in CNTs. Bright and dark excitons in BNNTs qualitatively alter the optical response [57].

The optical properties of carbon nanotubes are uniquely connected with the absorption, photoluminescence, and Raman scattering of carbon nanotubes. Spectroscopic methods are used for the characterization of large quantities of nanotubes without damaging them. Optical absorption, photoluminescence and Raman spectroscopies permit a reliable characterization for the quality of nanotube such as chirality, size, and structural defect of the produced nanotubes. These characterization shed light on other properties, such as optical, mechanical, and electrical properties. Raman spectroscopy, or light scattering, is a powerful technique used to investigate their spectroscopic and structural properties and provides significant insight into the fundamental physical processes that occur. Even though a large number of phonon modes in the Raman spectra of carbon nanotubes would be expected, most are Raman inactive due to the selection rules, as a consequence of the high symmetry properties of the nanotubes. The Raman spectrum of a carbon nanotube exhibits a few characteristic modes that can be used to determine the size of nanotubes and to classify the type of the nanotubes, such as semiconducting and metallic. For example, in the low frequency region, one type is called the radial breathing mode (RBM), which is in the radial direction with the same phase as a result of the vibration of the entire tube. This mode is strongly diameter dependent. The RBM is used to determine the size of the nanotube. There are two characteristic Raman bands that lie in the range of 1300-1650 cm^{-1} , which are called tangential modes. The line shape of these Raman modes may be used to classify whether the nanotube is metallic or semiconducting. These Raman modes in the high energy region are also slightly diameter dependent.

Theoretical calculations may be very useful to understand the nature of optical properties as well as their storage mechanisms. For a better understanding of the physical and optical properties of nanotubes, theoretical calculation may be needed to specify the material properties due to the dependence of their spectroscopic properties on the size of the nanotubes. The electronic structures of the single-walled boron nitride nanotubes (SWBNNTs) were theoretically investigated by Rubio *et al.* [56] using the tight binding approximation. All SWBNNTs were found to be semiconducting materials with the band gaps greater than 2 eV. BNNTs with larger diameters have a larger band gap, with a saturation value corresponding to the band gap of a hexagonal boron nitride [56,57]. The local-density-functional (LDA) calculations [58] indicated that the folding of a hexagonal boron nitride sheet into a BNNT is energetically more favorable than to form a CNT from a graphite sheet [57]. Molecular dynamics simulations have been applied to explore the interactions between molecules and BNNTs in addition to structural and thermal stability of the BNNTs [59]. It has been reported that the (5, 5) boron nitride nanotube transport water, although the (5, 5) CNT is not able to do so because of much larger energy barrier. The Van der Waals interactions between water molecules and nitrogen atoms decrease the energy barrier of the BNNTs. For reason, BNNTs with the small diameter were suggested as an aspirant for a synthetic aquaporin-1 water channel [57]. A variety of subjects of BNNTs have been investigated by theoretical methods, including hydrogen storage [60,61,62,63,64,65, 66], magnetism [67,68,69,70,71,72,73], phonon characteristics [74,75,76], stability [77,78,79], molecular dynamics [80,81,82,83], field-electron emission [84], scanning tunneling microscopy simulation [85], electron transport [86], symmetry breaking [87], work function [88], spin-splitting [89] and quantum computing [90,91].

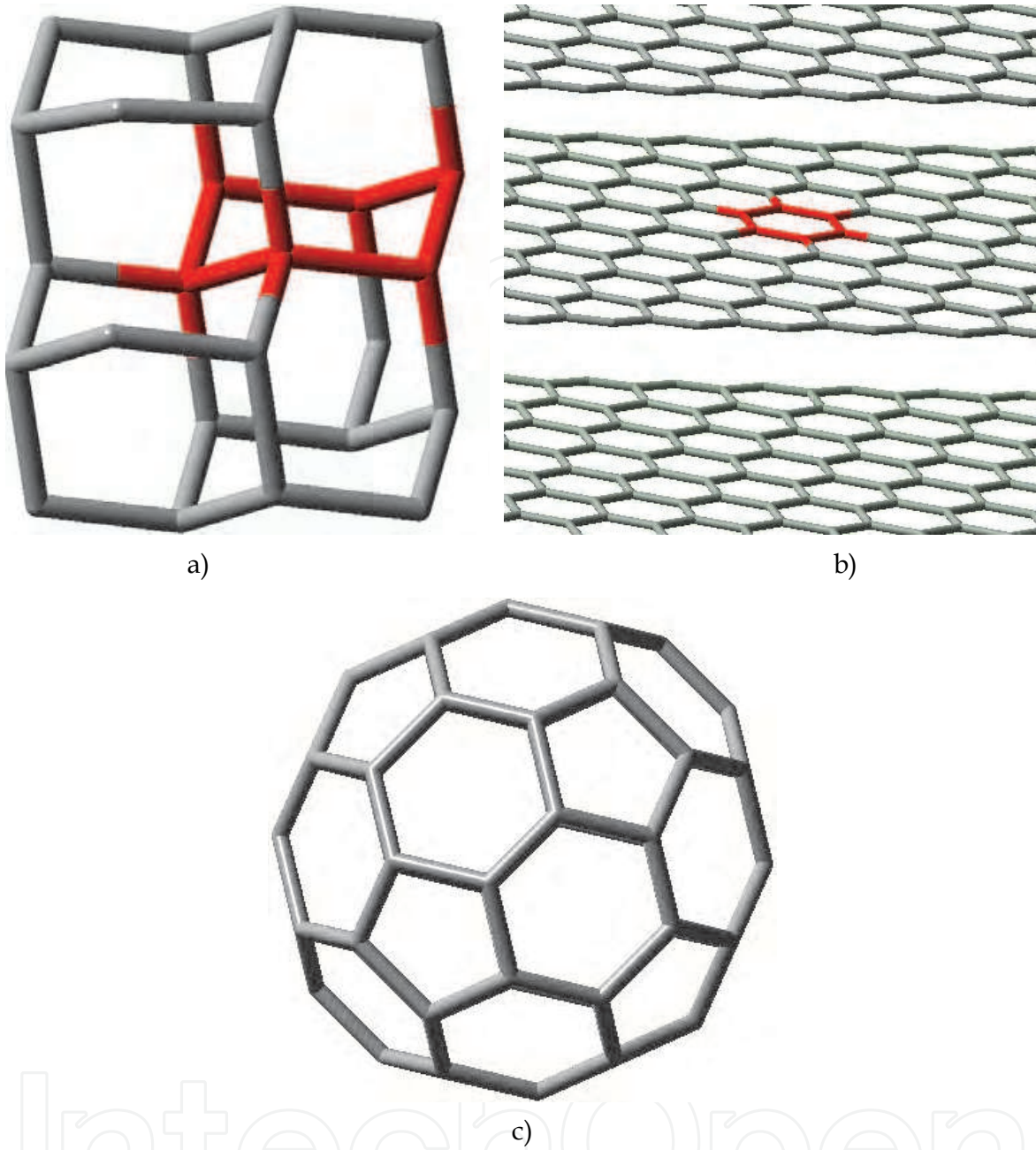


Fig. 1.1. a. Diamond, b. Graphite, c. C_{60} fullerenes

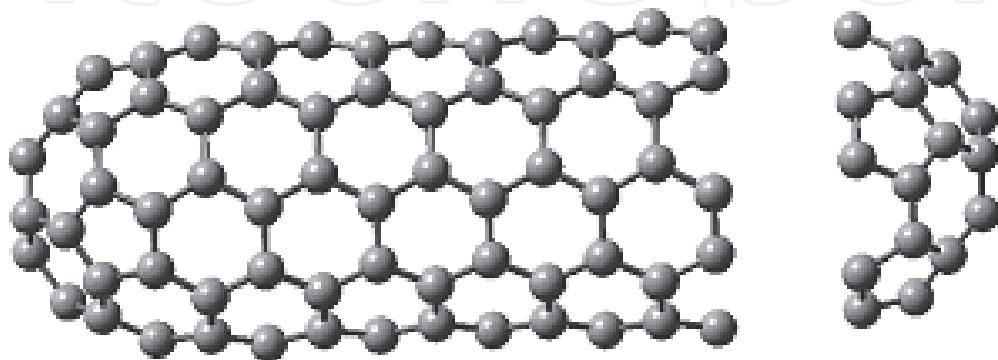


Fig. 1.2. (5,5)-single-wall carbon nanotube (SWCNT)

2. Geometrical structure

As is well known, a carbon nanotube can be visualized as being formed by rolling up a well-defined projected area within the hexagonal lattice of a graphene sheet in a seamless fashion such that all carbon-carbon (C-C) valences are satisfied, and the direction in which the roll up is performed transforms into the circumference of the tube. The projected area is in fact a homomorphic representation of a particular carbon nanotube.

There are many possible ways to roll up a graphene sheet into a cylinder with the hexagons to be completed. Figure 2.3A illustrates such an example of tube construction. The roll-up vector is also termed the chiral vector (\vec{C}) and is defined as $n\vec{a}_1 + m\vec{a}_2$, where \vec{a}_1 and \vec{a}_2 are the basis vectors of the graphene lattice; n and m are the so-called chiral indices. By using unit vectors \vec{a}_1 and \vec{a}_2 with the chiral indices n and m , geometric parameters of a carbon nanotube can be defined. In general, an infinite number of nanotube geometries are possible, with specific nanotubes characterized by chiral indices (n,m) , which, in turn, define the chiral angle (θ) and tube diameter (d_t); the latter is also dependent on the C-C bond length of the hexagonal lattice. For $n = m$, the nanotube is said to have the "armchair" conformation; for $n \neq 0$ and $m = 0$, the conformation is called "zigzag"; while for $n \neq 0$ and $m \neq 0$ the conformation is termed "chiral." As seen in Figure 2.3E-F, double-walled carbon nanotubes (DWCNTs) are in the border between single-walled carbon nanotubes (SWCNT) and multi-walled carbon nanotubes (MWCNT).

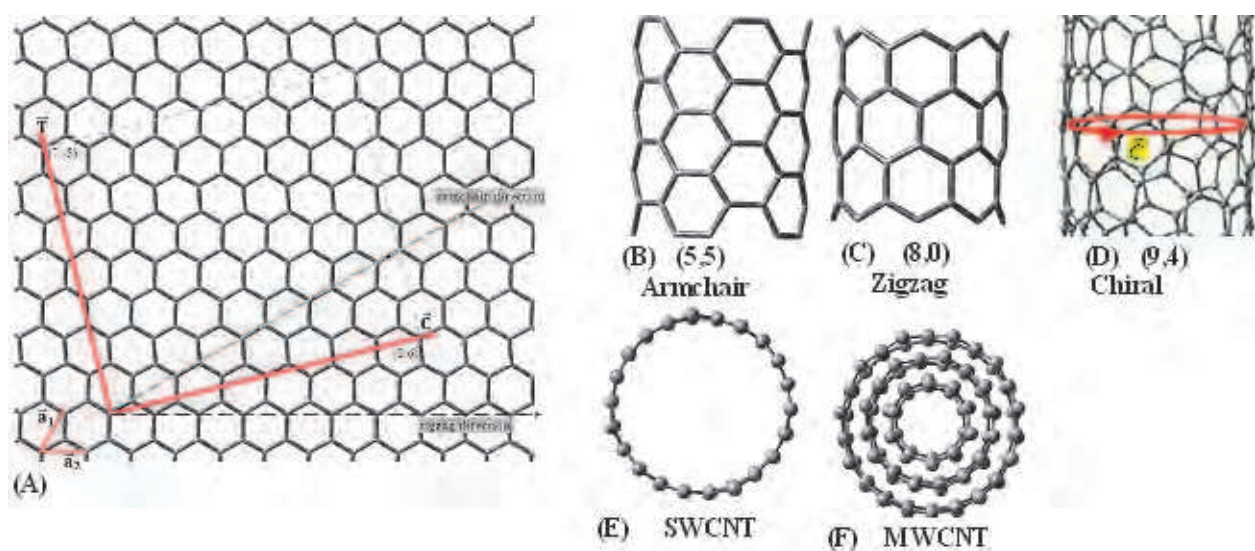


Fig. 2.3. The graphene honeycomb sheet and the schematically represented nanotube that can be obtained by rolling up the graphene layer along the chiral vector \vec{C} turns into the circumference of the cylinder, and the translation vector \vec{T} is aligned along the cylinder axis and represents the unit cell of a carbon nanotube.

As mentioned above, the chiral vector \vec{C} is defined by the use of the real space unit vectors \vec{a}_1 and \vec{a}_2 of the hexagonal lattice as follows:

$$\vec{C} = n\vec{a}_1 + m\vec{a}_2 \quad (2.1)$$

Here the angle between the unit vectors \vec{a}_1 and \vec{a}_2 is 60 degree and $|\vec{a}_1| = |\vec{a}_2| = a = \sqrt{3}a_{CC}$ where $a_{CC} (\cong 0.142 \text{ nm})$ is the average C-C bond distance in two dimensional network (2D) of the graphene lattice and n and m are integer numbers. The magnitude of chiral vector \vec{C} can be given by equation 2.2

$$|\vec{C}| = a\sqrt{n^2 + m^2 + nm} \quad (2.2)$$

Since the single wall carbon nanotube is formed by rolling up the sheet along the direction of the chiral vector \vec{C} , the circumference of cylindrical carbon nanotube equal to the length of the chiral vector \vec{C} . For a given pair of integers (n, m) , the diameter d_t of a carbon nanotube may be derived from the length of the chiral vector \vec{C} as follows:

$$d_t = \frac{|\vec{C}|}{\pi} = \frac{a\sqrt{n^2+m^2+nm}}{\pi} \quad (2.3)$$

The angle (θ) between the chiral vectors \vec{C} and the primitive lattice translation vector \vec{a}_1 is called as chiral angle, which is in the range of 0 to 30 degree and can be expressed by the pair of integers (n, m) , and defined by using the scalar product of the vectors \vec{a}_1 and \vec{C} :

$$\cos(\theta) = \frac{\vec{a}_1 \cdot \vec{C}}{|\vec{a}_1| |\vec{C}|} = \frac{2n+m}{2\sqrt{n^2+m^2+nm}} \quad (2.4)$$

The chiral angle θ can be given in tangential form as well by the vector and scalar product of the vectors \vec{a}_1 and \vec{C} as follow:

$$\tan(\theta) = \frac{|\vec{a}_1 \otimes \vec{C}|}{|\vec{a}_1 \cdot \vec{C}|} = \frac{\sqrt{3}m}{2n+m} \quad (2.5)$$

Furthermore, it may be useful to specify the unit cell of a carbon nanotube (CNT), which is a part of a nanotube containing non-equivalent atoms. CNT can be naturally defined as a cylinder built on two orthogonal vectors \vec{C} and \vec{T} , where \vec{T} is the translation vector parallel to the nanotube axis and perpendicular to \vec{C} as seen in Figure 2.3A. The translation vector \vec{T} can be expressed in term of the basis vectors \vec{a}_1 and \vec{a}_2 as follows:

$$\vec{T} = t_1\vec{a}_1 + t_2\vec{a}_2 \equiv (t_1, t_2) \quad (2.6)$$

Since the \vec{T} and \vec{C} vectors are orthogonal to each other and their scalar product should be zero,

$$\vec{T} \cdot \vec{C} = (t_1\vec{a}_1 + t_2\vec{a}_2) \cdot (n\vec{a}_1 + m\vec{a}_2) = t_1(n + m/2) + t_2(n/2 + m) = 0 \quad (2.7)$$

$$t_1 = -\left(\frac{n+2m}{2n+m}\right)t_2 \quad (2.8)$$

In Figure 2.3A the unit cell of the graphite is the rhombus specified by the vectors \vec{a}_1 and \vec{a}_2 and containing two carbon atoms. The number of hexagons (N) per unit cell of a carbon nanotube can be obtained dividing the area of the nanotube unit cell ($|\vec{T} \otimes \vec{C}|$) by the area of the graphite unit cell ($|\vec{a}_1 \otimes \vec{a}_2|$, the area of the rhombus is equal to the area of the hexagon):

$$N = \frac{|\vec{T} \otimes \vec{C}|}{|\vec{a}_1 \otimes \vec{a}_2|} = \frac{|(t_1 \vec{a}_1 + t_2 \vec{a}_2) \otimes (n \vec{a}_1 + m \vec{a}_2)|}{|\vec{a}_1 \otimes \vec{a}_2|} = |(mt_1 - nt_2)| \frac{|\vec{a}_1 \otimes \vec{a}_2|}{|\vec{a}_1 \otimes \vec{a}_2|} = |(mt_1 - nt_2)| \quad (2.9)$$

$$mt_1 - nt_2 = \pm N \quad (2.10)$$

Substituting Eq. 2.8 into 2.10 and by setting $d_R = \frac{2(n^2+m^2+nm)}{N}$, we found that

$$t_1 = \pm \frac{n+2m}{d_R} \text{ and } t_2 = \mp \frac{2n+m}{d_R} \quad (2.11)$$

Here d_R is called the greatest common divisor (GCD) and may be defined in terms of the greatest common divisor of n and m as given by Eq. 2.12,

$$d_R = \begin{cases} \text{GCD}(2n + m, n + 2m) \\ \text{or} \\ 3M, \text{ if } n - m = 3l \\ M, \text{ if } n - m \neq 3l \\ \text{here } l = 0, 1, 2, \dots \end{cases} \quad (2.12)$$

2.2 Electronic structure of SWNTs

Before examining the electronic properties of carbon nanotubes, we briefly discuss the electronic structure of graphene investigated which also underline the band structure of the nanotubes. For more detail see Ref.92. Graphene is characterized by two types of chemical bonds which are linked to the sp^2 hybridization of the carbon atomic orbitals. The energy band of the three strong σ - bonds within the honeycomb lattice are far from the Fermi level. Therefore, these bonds do not have any contribution to the electronic transport properties of graphene and nanotubes.

The remaining p_z orbitals, pointing out of the σ -bond plane, cannot couple with the σ - states for symmetry arguments. The lateral interaction with neighboring p_z orbitals creates delocalized π - (bonding) and π^* (antibonding) states, which determine the energy bands around the Fermi energy E_F .

The two-dimensional graphene lattice in real space can be formed by translating one unit cell of graphene defined by two basis vectors: $\vec{a}_1 = \frac{a}{2}(\sqrt{3}\hat{x} + \hat{y})$ and $\vec{a}_2 = \frac{a}{2}(\sqrt{3}\hat{x} - \hat{y})$, where $|\vec{a}_1| = |\vec{a}_2| = a = \sqrt{3}a_{CC}$ is the length of the basis vector and $a_{CC} (\approx 0.142 \text{ nm})$ is the nearest neighbor C-C bonding distance. The unit cell of graphene consists of two atoms, A and B, as seen in Fig. 2.3a. A and B atoms form two complementary, hexagonal sublattices. The basis vectors \vec{b}_1 and \vec{b}_2 in the reciprocal lattice as shown in Fig. 2.3b, satisfies the condition $\vec{a}_i \cdot \vec{b}_j = 2\pi\delta_{ij}$ allows one to find the reciprocal-lattice vectors \vec{b}_1 and \vec{b}_2 : $\vec{b}_1 = \frac{2\pi}{a}(\frac{\hat{x}}{\sqrt{3}} + \hat{y})$ and $\vec{b}_2 = \frac{2\pi}{a}(\frac{\hat{x}}{\sqrt{3}} - \hat{y})$.

A tight binding approximation (TBA) takes into consideration the interactions between only the nearest neighbor atoms for the band structure of graphene (Figure 2.3c), the remaining interactions are ignored, and only one p_z orbital per carbon atom is allowed for in calculations. It should be pointed out that tight-binding approximation gives reliable results at the energy range near the Fermi level of the graphene sheet, which is the region of interest for electronic transport [93]. By considering two independent wave functions (adhering to the Bloch theorem) for the electrons corresponding to the two complementary sublattices

and neglecting the overlap matrix elements $S = \langle \psi(p_z, A) | \psi(p_z, B) \rangle$ one obtains the following relation for the energy dispersion of the bands in graphene:

$$E^\pm(\vec{k}) = \pm \gamma \sqrt{3 + 2[\cos(\vec{k} \cdot \vec{a}_1) + \cos(\vec{k} \cdot \vec{a}_2) + \cos(\vec{k} \cdot \vec{a}_1 - \vec{k} \cdot \vec{a}_2)]} \quad (2.13)$$

Where $\gamma = 2.9 \pm 0.2$ eV is the interaction energy between the nearest neighbor atoms A and B. The $\vec{k} = k_x \hat{x} + k_y \hat{y}$ vectors, which belong to the first Brillouin zone (BZ) of the hexagon, as seen in Fig. 2.3b, represent the ensemble of available electronic momenta.

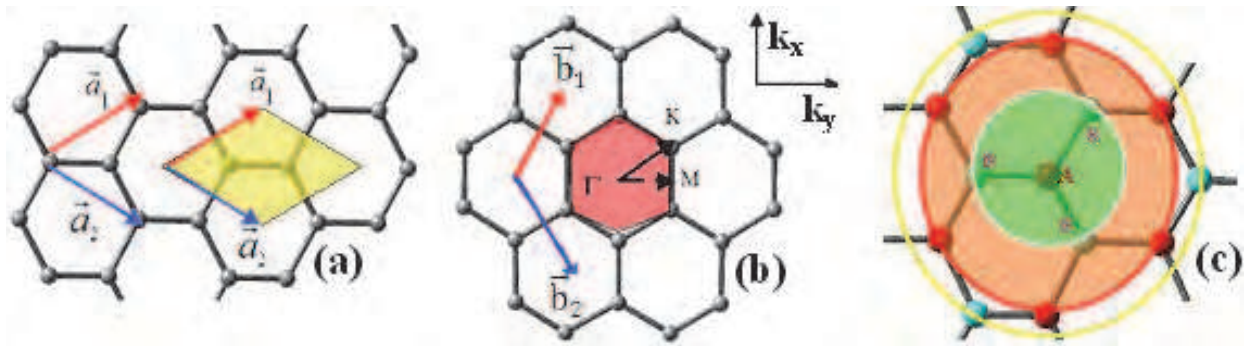


Fig. 2.3. **a)** Unit cell of graphene containing two atoms A and B defining two complementary sublattices; **b)** the hexagonal Brillouin zone (BZ) of graphene with the reciprocal lattice vectors \vec{b}_1 and \vec{b}_2 : $\vec{b}_1 = \frac{2\pi}{a}(\frac{\hat{x}}{\sqrt{3}} + \hat{y})$ and $\vec{b}_2 = \frac{2\pi}{a}(\frac{\hat{x}}{\sqrt{3}} - \hat{y})$. The Γ , K and M represent the high symmetry points; **c)** Atom A (in red color) has three the nearest atoms B (in light blue colour), six second nearest atoms A and three third nearest atoms B as shown in the shaded area in the figure. Here \vec{a}_1 and \vec{a}_2 are the unit cell vectors: $\vec{a}_1 = \frac{a}{2}(\sqrt{3}\hat{x} + \hat{y})$ and $\vec{a}_2 = \frac{a}{2}(\sqrt{3}\hat{x} - \hat{y})$.

Figure 2.4a-b shows a three-dimensional plot of the energy dispersion $E(k)$ along the high symmetry directions of the BZ, defined by the Γ , M and K points. The conduction and valence bands touch and are degenerate at the six K points at the corners of the first BZ, thus allowing the classification of graphene as a semimetal. Three out of the six K points are equivalent due to the spatial symmetry of the hexagonal lattice, thus two distinguishable points remain called K and K' . The bonding bands are completely filled and the antibonding bands are empty at zero temperature. The undoped state, where the Fermi surface contains only the six K points, is called the “charge neutrality point”. In the region of the Fermi, Taylor expansion of Eq. 2. 13 provides a simplified linear energy dispersion relation:

$$E(\vec{k}) = \frac{\sqrt{3}a\gamma}{2} |\vec{k} - \vec{k}_F| \quad (2.14)$$

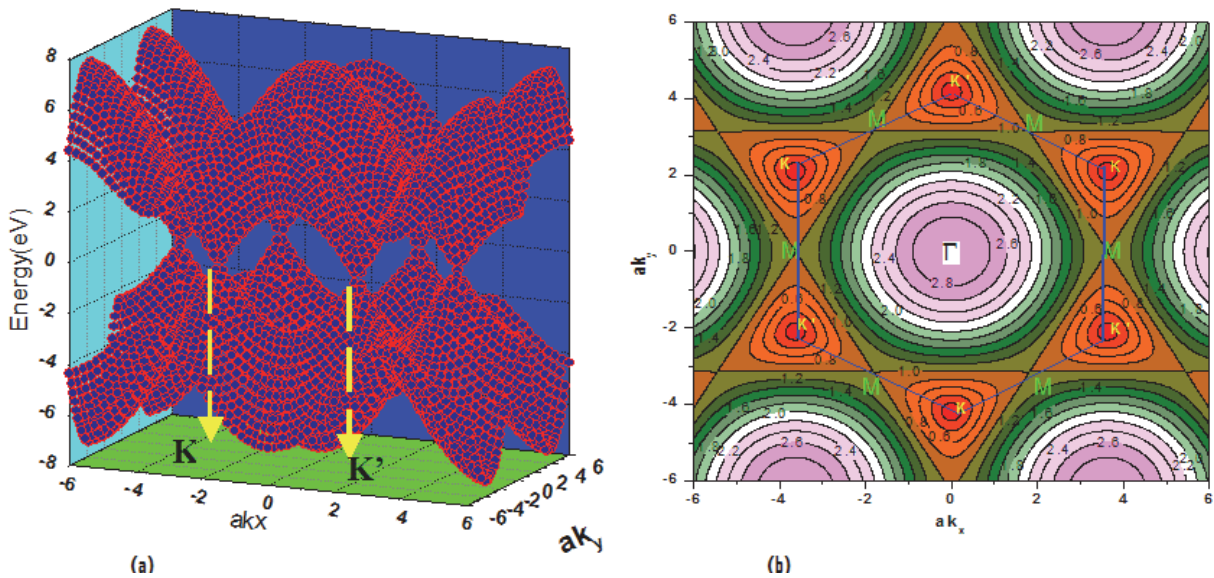


Fig. 2.4. The energy dispersion of the $E(k)$ for the graphene: a) indicates three-dimensional plot and b) the counter plot.

By using Zone-folding approximation, the energy dispersion relation of CNTs can be obtained from the simplified linear energy dispersion relation of the graphene near the Fermi level since a carbon nanotube consisting of one graphene sheet rolled into a cylinder. By applying periodic boundary conditions along the circumference of a SWNT, it is easy to see that, whereas the allowed wave vectors in direction perpendicular to the tube axis are quantized, the wave vectors parallel to the nanotube axis remain continuous since the nanotube has an infinite length. The application of periodic boundary conditions around the tube circumference brings about the following restrictions on the allowed wavefunctions:

$$\psi_{\mathbf{k}}(\vec{r} + \vec{C}) = \exp(i\vec{k} \cdot \vec{C}) \psi_{\mathbf{k}}(\vec{r}) = \psi_{\mathbf{k}}(\vec{r}) \quad (2.15)$$

where vectors \vec{k} and \vec{C} are respectively allowed wave vector undertaken the tube surface and circumference of the nanotube. This is the first equality arising from the Bloch theorem. Thus, the periodic boundary condition imposed along the circumference direction restricted the wave vectors to:

$$\vec{k} \cdot \vec{C} = 2\pi q; \quad q=0, 1, 2, \quad (2.16)$$

The energy dispersion relation near the Fermi-points is the most fascinating: If the distance between the high symmetry points, Γ and K , is defined by the vector $\vec{k}_F = \frac{1}{3}(\vec{b}_1 - \vec{b}_2)$, then the component of the \vec{k}_F on the circumferential direction ($\vec{C} = n\vec{a}_1 + m\vec{a}_2$) can be obtained by a scalar product of these two vectors \vec{k}_F and \vec{C} , with using $\vec{b}_i \cdot \vec{a}_j = 2\pi\delta_{ij}$, as follows:

$$\vec{k}_F \cdot \vec{C} = \frac{1}{3}(\vec{b}_1 - \vec{b}_2) \cdot (n\vec{a}_1 + m\vec{a}_2) = 2\pi \left(\frac{n-m}{3} \right) \quad (2.17)$$

If the origin of the reciprocal lattice is placed to the Fermi point, the distance between \vec{k}_F and one of the allowed states at \vec{k} can be given in the new coordinate system:

$$\Delta\vec{k} = \vec{k} - \vec{k}_F = \vec{k}_{\perp} + \vec{k}_{\parallel} \quad (2.18)$$

where \vec{k}_\perp is along the circumference direction \vec{C} , and \vec{k}_\parallel is along the nanotube axis and \vec{k}_\perp is perpendicular to \vec{k}_\parallel . The scalar product of the Eq 2. 18 with the chiral vector \vec{C} , with using Eqs. 2. 16 and 2. 17, we could easily reach one of the important equation, which indicate that component of the vector $\Delta\vec{k}$ along the circumference direction, $|\vec{k}_\perp| = |\Delta\vec{k}_C^q|$, is quantized and given by:

$$|\vec{k}_\perp| = |\Delta\vec{k}_C^q| = \frac{\Delta\vec{k} \cdot \vec{C}}{|\vec{C}|} = \frac{(\vec{k} - \vec{k}_F) \cdot \vec{C}}{|\vec{C}|} = \frac{2}{3d_t} [3q - (n - m)] \quad (2.19)$$

where d_t is the diameter of the nanotube.

The general form of the energy dispersion relation at vicinity of Fermi level for the 1D nanotube can be obtained by substituting Eq. 2. 19 into Eq. 2. 14 as follow:

$$E(\Delta\vec{k}) = \frac{\sqrt{3}a|\gamma|}{2} |\Delta\vec{k}| = \frac{\sqrt{3}a|\gamma|}{2} \sqrt{|\Delta\vec{k}_C^q|^2 + |\vec{k}_\parallel|^2} \quad (2.20)$$

From equation 2. 20, it is obvious that the nanotube can be either metallic or semiconducting, depending on whether $(n-m)$ is the multiple of 3. For instance, at the Fermi level (at the corner of hexagon, K point), if an allowed \vec{k} line cross the graphene \vec{k}_F point, $\vec{k} - \vec{k}_F = 0$ and we find a selection rule on the metallic and semiconducting nanotube as $3q = n-m$, which indicates that the SWNT is metallic and $E(\Delta\vec{k}) = \frac{\sqrt{3}|\gamma|}{2} |\vec{k}_\parallel|$. If $\vec{k} - \vec{k}_F \neq 0$, $3q \neq n-m$, which denotes that the SWNT is semiconducting and $E(\Delta\vec{k}) \cong \frac{\sqrt{3}a|\gamma|}{2} |\Delta\vec{k}_C^q| = \frac{2\sqrt{3}a|\gamma|}{d_t} q$.

One-dimensional (1D) density-of-states (DOS) of the nanotubes may be defined as the number of accessible electronic states for a given energy interval. The DOS has a great importance for many physical phenomena such as optical absorption-emission, conductivity, etc. Furthermore, the one-dimensional DOS generate the resonant Raman scattering in addition to intensive interband transitions in the spectra of the optical absorption and emission. The DOS is known to depend strongly on the dimension of the system[92]. One-dimensional density-of-states may be calculated by using Eq. 2. 21 [92]:

$$DOS(E) = \frac{2}{N} \sum_q \frac{\delta(E_q(\vec{k}) - E) dE}{\left| \frac{dE_q(\vec{k})}{d\vec{k}} \right|} \quad (2.21)$$

Since the energy dispersion vicinity of Fermi level is linear, then, the density of states (DOS) of metallic nanotube is constant at Fermi level and inversely proportional to the diameter of the nanotube: $DOS(E_F) = \frac{a}{2\pi^2\gamma d_t}$

The average energy position of the peaks depends on the nanotube diameter, which is defined by the linear dispersion approximation (as discussed above). Figure 2.5 provides calculated energy dispersion and DOS for (10, 10) carbon nanotube.

3. Results and discussion

Computational methods: The ground state geometry of the single-walled carbon nanotubes (SWCNTs), double walled carbon nanotubes (DWCNTs), the single-walled boron nitride nanotubes (SWBNNTs) and functionalized-SWCNTs were optimized without symmetry restriction on the initial structures. Both structure optimization and vibrational analysis calculations were implemented by using DFT with functionals, specifically, B3LYP, in which

the exchange functional is of Becke's three parameter type, including gradient correction, and the correlation correction involves the gradient-corrected functional of Lee, Yang and Parr. The basis set of split valence type 6-31G, as contained in the Gaussian 03 software package,[94] was used. The results of the calculations did not produce any imaginary frequencies. The vibrational mode descriptions were made on the basis of calculated nuclear displacements using visual inspection of the animated normal modes (using GaussView03) [94], to assess which bond and angle motions dominate the mode dynamics for the nanotube. The DFT method was chosen because it is computationally less demanding than other approaches as regards inclusion of electron correlation. Moreover, in addition to its excellent accuracy and favorable computation expense ratio, the B3LYP calculation of Raman frequencies has shown its efficacy in numerous earlier studies performed in this laboratory and by other researchers, often proving itself the most reliable and preferable method for many molecular species of intermediate size, including anions and cations[95].

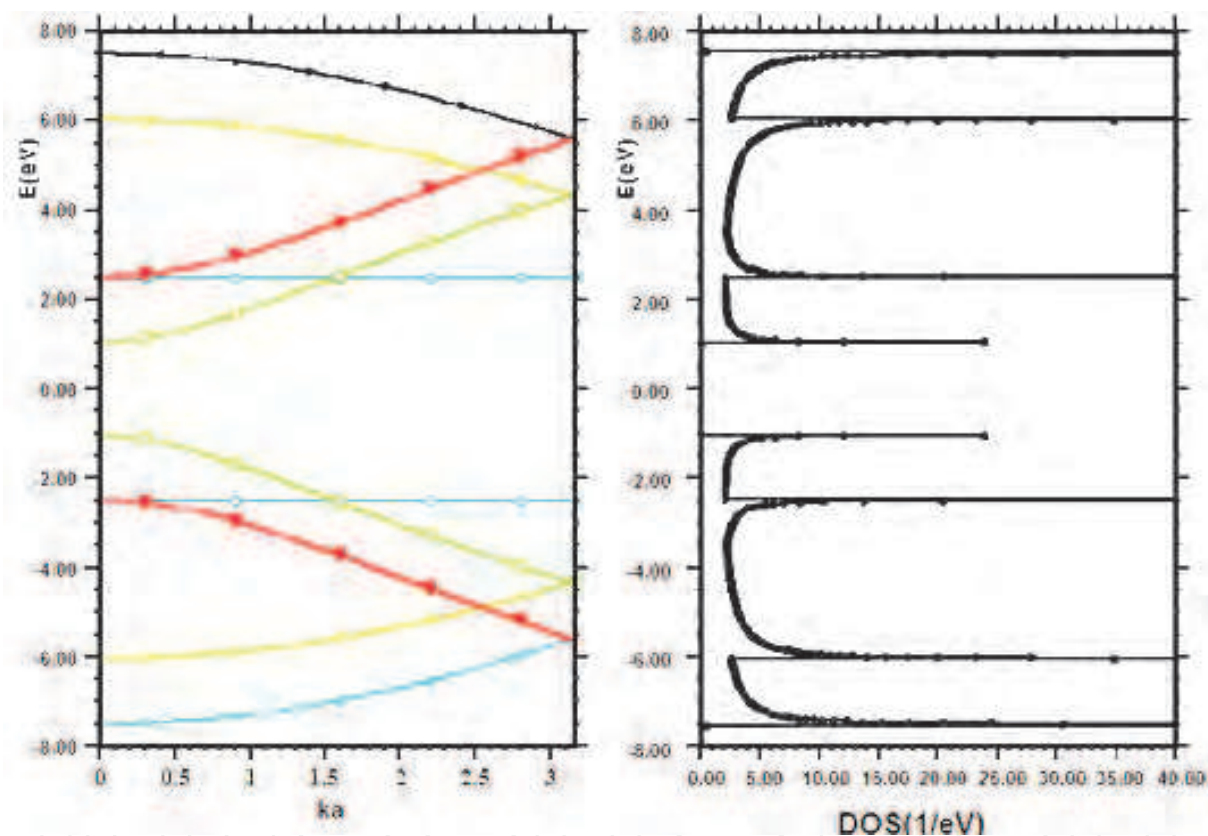


Fig. 2.5. Calculated energy dispersion relation and the density of states (DOS) for a (10,10) nanotube.

In our calculations hydrogen atoms have been placed at the end points of the unit cells. Furthermore, the time-dependent density functional theory at TD-B3LYP level were applied to calculate the vertical electronic transitions for the SWCNTs, SWBNNTs and functionalized (7,0)- and (10,0)-SWCNTs.

3.1 Structure results

Calculated averaged C-C bond distances within the single wall carbon nanotube (SWCNT) for the $(n,0)$ -SWCNTs with $n = 6$ to 19 for the (n,n) -SWCNTs with $n = 3$ to 10 were not only

found to be diameter dependent, but also dependent on length of the tube as seen in Table 3.1.1 and 3.1.2 and Figure 3.1.1. The calculated averaged B-N bond distances within the armchair and zigzag boron nitride nanotubes (BNTs) also indicated similar diameter- and size-dependence (see Table 3.1.1 and 3.1.2). The plot of the calculated averaged bond distances for the $(n,0)$ - and (n,n) -type nanotubes indicated that the bond distances within the nanotube slightly decreases and stabilizes with increasing diameter of the isolated nanotube; the solid curves in Figure 3.1.1 is a fit to the calculated energies using a functional form that depends inversely on nanotube diameter: fitting equations are given in Eq. 1a-1e. As seen in Figure 3.1.1, for the $(n,0)$ -SWCNTs, the plot of the averaged CC bond distance versus the tube diameter indicated that the CC bond distance does not only decrease with increasing tube diameter as expected, but also the bond distances of $(0,2n)$ and $(0,2n+1)$ -type SWCNTs are well separated. This circumstance is also observed in the folding (curvature) energies (Eq2a-2b) and in the Raman spectra of $(0,2n)$ - and $(0,2n+1)$ -type SWCNTs. However, the calculations for the rest of the nanotube studied here did not clearly indicate this observation.

$$R_{CC}((2n, 0); \text{ in nm}) = 0.1422 - \frac{0.0004}{d_t} + \frac{0.0004}{d_t^2} \quad (3.1.1a)$$

$$R_{CC}((2n + 1, 0); \text{ in nm}) = 0.1422 - \frac{0.0003}{d_t} + \frac{0.0003}{d_t^2} \quad (3.1.1b)$$

$$R_{CC}((n, n); \text{ in nm}) = 0.1421 - \frac{0.0003}{d_t} + \frac{0.0003}{d_t^2} \quad (3.1.1c)$$

$$R_{BN}((n, n); \text{ in nm}) = 0.1449 - \frac{0.0002}{d_t} + \frac{0.0003}{d_t^2} \quad (3.1.1d)$$

$$R_{BN}((n, 0); \text{ in nm}) = 0.1433 - \frac{0.0003}{d_t} + \frac{0.0003}{d_t^2} \quad (3.1.1e)$$

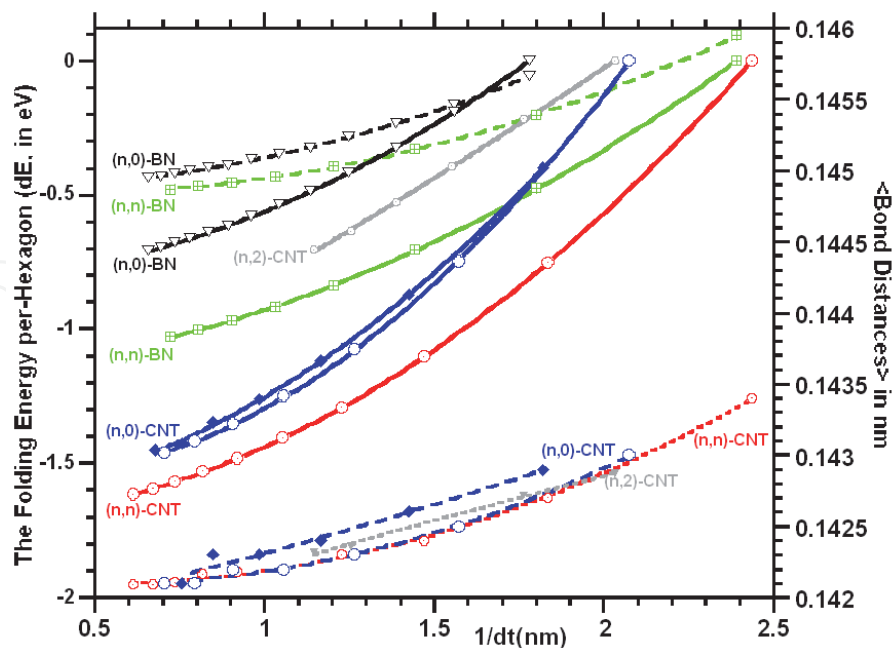


Fig. 3.1.1. The calculated folding (curvature) energies of $(n,0)$ -, (n,n) -SWCNTs/BN-nanotubes and $(n,2)$ -SWCNTs referenced to their the nanotube with the smallest diameter and boron nitride nanotubes with their corresponding bond distances.

Figure 3.1.1 provides the plot of the calculated global energy per-hexagon for the (n,0)- and (n,n)-SWCNTs/SWBNNTs referenced to their corresponding (6,0)- and (3,3)-SWCNT/SWBNNTs energies, respectively. The result of the calculations suggested that the curvature energy (or folding energy) of the nanotubes rapidly decrease and stabilizes with increasing the diameter of the isolated nanotube; the solid curves in Figure 3.1.1 is a fit to the calculated energies using a functional form that depends inversely on nanotube diameter. The fitting parameters are given in equations. 3.1.2a-2e. The plot of the calculated folding energy for the (n,2)-SWCNTs, with n=5 to 10, exemplified similar fitting equations as given in Equation 3.1.2f.

$$\Delta E((n, 0) - \text{CNTs}) = E_{(n,0)} - E_{(6,0)} = -1.64 - \frac{0.04(\text{eV}\cdot\text{nm})}{d_t(\text{nm})} + \frac{0.36(\text{eV}\cdot(\text{nm})^2)}{d_t^2(\text{nm})^2} \quad (3.1.2a)$$

$$\Delta E((n, 0) - \text{CNTs}) = E_{(n,0)} - E_{(6,0)} = -1.52 - \frac{0.25(\text{eV}\cdot\text{nm})}{d_t(\text{nm})} + \frac{0.74(\text{eV}\cdot(\text{nm})^2)}{d_t^2(\text{nm})^2} \quad (3.1.2b)$$

$$\Delta E((n, n) - \text{CNTs}) = E_{(n,n)} - E_{(3,3)} = -1.71 - \frac{0.02(\text{eV}\cdot\text{nm})}{d_t(\text{nm})} + \frac{0.30(\text{eV}\cdot(\text{nm})^2)}{d_t^2(\text{nm})^2} \quad (3.1.2c)$$

$$\Delta E((n, 0) - \text{BNNT}) = E_{(n,0)} - E_{(7,0)} = -0.82 + \frac{0.26(\text{eV}\cdot(\text{nm})^2)}{d_t^2(\text{nm})^2} \quad (3.1.2d)$$

$$\Delta E((n, n) - \text{BNNTs}) = E_{(n,n)} - E_{(3,3)} = -1.17 + \frac{0.06(\text{eV}\cdot\text{nm})}{d_t(\text{nm})} + \frac{0.18(\text{eV}\cdot(\text{nm})^2)}{d_t^2(\text{nm})^2} \quad (3.1.2e)$$

$$\Delta E((n, 2) - \text{CNTs}) = E_{(n,0)} - E_{(6,0)} = -1.54 - \frac{0.67(\text{eV}\cdot\text{nm})}{d_t(\text{nm})} + \frac{0.04(\text{eV}\cdot(\text{nm})^2)}{d_t^2(\text{nm})^2} \quad (3.1.2f)$$

In Eq. 3.1.2a-3.1.2f, $E_{n,m}$ stand for the folding energy (in eV) of the (n,m)-type isolated single-wall carbon and boron nitride nanotubes and d_t corresponds to their tube diameter in nm unit. Clearly, larger diameter SWCNTs/SWBNNTs can be more easily formed than the smaller diameter ones in gas phase. For example, while energy differences for the (7,0) through (12,0)-SWCNT, relative to the (6,0)-SWCNT, rapidly approaches a limiting value, one notes that from the (11,0)- up to the (16,0)-SWCNT a limiting value is nearly reached and changes in energy approach zero. Of course, this is to be expected since the smaller diameter, the more strained are the sp^2 hybridized sigma bonds; or stated another way, the smaller the diameter the more altered from planarity must be the sp^2 hybridized orbitals. It should be noted that the formation of the nanotube in gas phase and in any environment might be different. The size of the nanotube in an environment also depends on cavity size of the environment owing to the electrostatic interactions between the tube and its neighboring. When comparing the folding energy of the (n,0)-type nanotubes with that of the (n,n)-type nanotube, the calculations indicated that folding of the zigzag nanotubes are more easily than that of the armchair-nanotubes for both carbon nanotubes and boron nitride nanotubes. This observed circumstance is expected because of the geometrical reason, for instance, while three of the sigma bonds as a result of the sp^2 -hybridized orbitals in the armchair nanotubes are folded, only two of three sp^2 -hybridized orbitals in the zigzag-form of the nanotubes are folded and one of them along the nanotube axis without folding. This assessment also is found in the bond distances such as the CC bond distances in the (n,n)-type nanotubes are longer than in the (n,0)-type nanotubes as seen in Figure 3.1.1 and Table 3.1.1 or equations 3.1.1a-3.1.1e. Based on part of the calculations, when comparing the carbon nanotubes with the boron

nitride nanotubes, as seen in Figure 3.1.1 and equations 3.1.2a-3.1.2e, the formation of the carbon nanotubes is more easily than the boron nitride nanotubes.

n	SWCNTs						SWBNNTs			
	(0, n)		(n, n)		(2, n)		(0, n)		(n, n)	
	<CC>	dt	<CC>	dt	<CC>	dt	<BN>	dt	<BN>	dt
3			0.143	0.411					0.146	0.418
4			0.143	0.545					0.145	0.555
5			0.142	0.680	0.143	0.493			0.145	0.693
6	0.143	0.473	0.142	0.815	0.143	0.567			0.145	0.831
7	0.143	0.552	0.142	0.951	0.143	0.644	0.146	0.562	0.145	0.969
8	0.142	0.628	0.142	1.087	0.143	0.721	0.146	0.642	0.145	1.107
9	0.143	0.708	0.142	1.222	0.142	0.797	0.145	0.721	0.145	1.245
10	0.142	0.785	0.142	1.357	0.142	0.875	0.145	0.801	0.145	1.383
11	0.142	0.864	0.142	1.492			0.145	0.880		
12	0.142	0.941	0.142	1.628			0.145	0.960		
13	0.142	1.020					0.145	1.040		
14	0.142	1.098					0.145	1.120		
15	0.142	1.177					0.145	1.199		
16	0.142	1.253					0.145	1.279		
17	0.142	1.332					0.145	1.359		
18	0.142	1.410					0.145	1.439		
19	0.141	1.476					0.145	1.518		

Table 3.1.1. The calculated averaged CC and BN bond distances and diameters of the (n, m)-type nanotube in nm.

We also examined the dependence of the curvature energy on the length of the zigzag (n,0)-SWCNTs referenced to the (6,0)-SWCNT, defined as $\Delta E = E_{(n,0)}(m) - E_{(6,0)}(m)$. Where m indicates the number of hexagon along the tube axis, $m = 1$ to 4, and the chiral index n is ranging from 6 to 11. As seen in Figure 3.1.2, the calculated folding energy per hexagon for each m is compatible with each other. The estimated fitting parameters, given in equations 3.1.3a-3.1.3d, are almost the same. When we examined the folding energy per hexagon as function of the number of hexagon along the tube axis (m) for a given (n,0)-SWCNT, for example, (6,0)-SWCNT with $m = 1$ to 4, we found that the folding energy slightly increases (less than 0.1 eV) and stabilizes with increasing the number of hexagon along tube axis (m) of the isolated zigzag nanotube. This consequence also can be easily seen in equations 3.1.3a to 3.1.3d. Table 3.1.2 provides the calculated averaged CC bond distances and diameters of the zigzag and armchair isolated single-wall carbon nanotubes. The calculated averaged CC bond distances also slightly increases and stabilizes with increasing length of the tube. It can be seen that dependence of the geometric parameters and folding energies on the diameter and length of the nanotube is as a result of the deformation in the sp^2 -hybridized orbitals of the CC bonds.

$$E_{(n,0)}(m = 1) - E_{(6,0)}(m = 1) = -1.51 - \frac{0.16(\text{eV}\cdot\text{nm})}{d_t(\text{nm})} + \frac{0.42(\text{eV}\cdot(\text{nm})^2)}{d_t^2(\text{nm})^2} \quad (3.1.3a)$$

$$E_{(n,0)}(m = 2) - E_{(6,0)}(m = 2) = -1.51 - \frac{0.28(\text{eV}\cdot\text{nm})}{d_t(\text{nm})} + \frac{0.48(\text{eV}\cdot(\text{nm})^2)}{d_t^2(\text{nm})^2} \quad (3.1.3b)$$

$$E_{(n,0)}(m = 3) - E_{(6,0)}(m = 3) = -1.51 - \frac{0.17(\text{eV}\cdot\text{nm})}{d_t(\text{nm})} + \frac{0.43(\text{eV}\cdot(\text{nm})^2)}{d_t^2(\text{nm})^2} \quad (3.1.3c)$$

$$E_{(n,0)}(m = 4) - E_{(6,0)}(m = 4) = -1.51 - \frac{0.15(\text{eV}\cdot\text{nm})}{d_t(\text{nm})} + \frac{0.41(\text{eV}\cdot(\text{nm})^2)}{d_t^2(\text{nm})^2} \quad (3.1.3d)$$

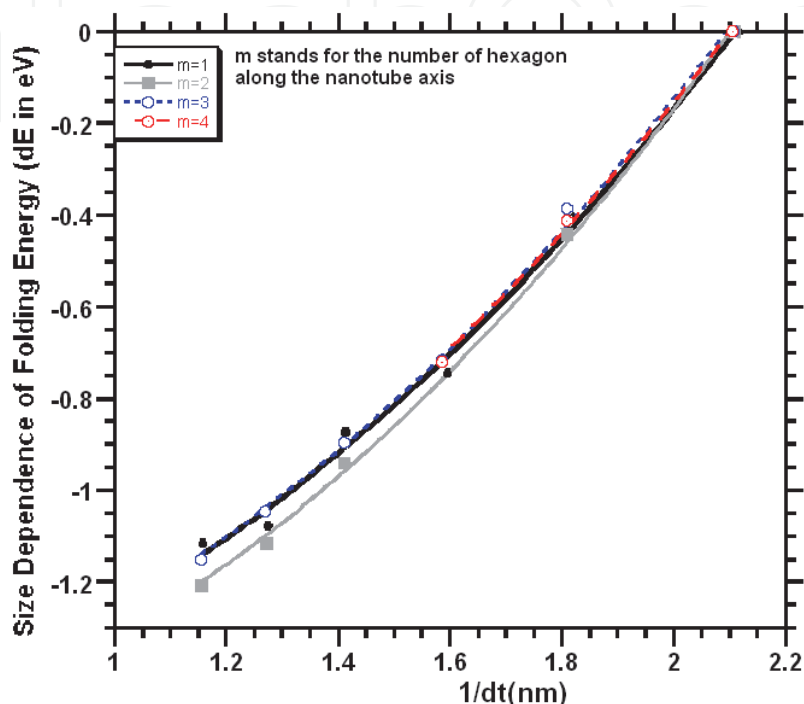


Fig. 3.1.2. The calculated size (the number of hexagon along the nanotube axis (m)) dependence of the folding energies for the (n,0)-SWCNTs, n=6 to 11, referenced to the (6,0)-SWCNT with the same number of m.

SWCNTs													
m	(4,4)		(0,6)		(0,7)		(0,8)		(0,9)		(0,10)		
	<CC>	dt	<CC>	dt	<CC>	dt	<CC>	dt	<CC>	dt	<CC>	dt	
1	0.141	0.540	0.143	0.473	0.143	0.552	0.142	0.627	0.143	0.707	0.142	0.785	
2	0.142	0.544	0.143	0.474	0.143	0.553			0.143	0.709	0.143	0.787	
3	0.143	0.545	0.144	0.475	0.143	0.553	0.143	0.631	0.143	0.709	0.143	0.787	
4	0.143	0.546	0.144	0.475	0.143	0.553	0.143	0.631	SWCNTs		SWBNNT		
5	0.143	0.546	0.144	0.475	0.143	0.553			(0,11)		(0,8)		
6	0.143	0.546							m	<CC>	dt	<CC>	dt
7	0.143	0.547						1	0.142	0.864	0.145	0.642	
8	0.143	0.547						2	0.143	0.865	0.146	0.642	
9	0.143	0.547						3	0.143	0.865	0.146	0.642	
10	0.143	0.547						4			0.146	0.642	
11	0.143	0.547						5			0.146	0.643	

Table 3.1.2. The dependence of calculated averaged CC and BN bond distances on the length and diameters (dt) of the nanotubes in nm. Where m indicates the number of hexagon along the nanotube axis.

The calculated full natural bond orbital analysis (NBO) indicates that three of the four valence electrons of the carbon atoms in SWCNTs are sp^2 -hybridized in the one-dimensional (1D) network, with ~34% s and ~66% p_{xy} character, and the fourth electron is ~100% p_z in character. As expected, each carbon atom contributes three electrons to the sigma bonds within the surface of the CNT and has one electron left in the p_z orbitals that is delocalized over the entire surface. Figure 3.1.3A provides the calculated electron density in some of the upper occupied molecular orbitals and lower unoccupied molecular orbitals. It is to be noted that the HOMO and LUMO are pure nonbonding π -orbitals (resulting from p_z atomic orbitals).

3.2 DWCNT

The DFT technique, at same level of the theory, was performed to calculate the Raman and IR spectra for $(n,0)\&(2n,0)$ -DWCNTs, $(6,0)\&(12,0)$, $(7,0)\&(14,0)$ and $(8,0)\&(16,0)$, as well as their inner- and outer-shell diameters and electron densities in gas phase. The key conclusions of these calculations on DWCNTs are summarized below. The diameter dependence of the curvature energies of the DWCNTs reference to the global energies of their corresponding inner- and outer-SWCNTs is well fitted by a Lannard-Jones potential expression as given in equation 3.2.1,

$$\Delta E(\text{eV}) = E[(2n, 0)\&(n, 0)] - E(2n, 0) - E(n, 0) = 3.676 \left\{ \left(\frac{0.702(\text{nm})}{D_t(\text{nm})} \right)^6 - \left(\frac{0.702(\text{nm})}{D_t(\text{nm})} \right)^{12} \right\} \quad (3.2.1)$$

which may be interpreted such as a van der Waals type intertube interactions for DWCNTs.

Where $\frac{1}{D_t} = \frac{1}{d_t(\text{Inner Shell})} - \frac{1}{d_t(\text{Outer Shell})}$. A comparison the diameters of the inner- and

outer-shells of the DWCNTs with their corresponding SWCNTs diameters showed that the averaged inner-shells diameters decrease ($\sim -0.08\text{\AA}$) and averaged outer-shells diameters increased as much as 0.25\AA . These changes also found in the averaged C-C bond distances; about -0.014 , 0.004 and 0.009\AA in inner-shells and 0.044 , 0.028 and 0.023\AA in outer-shells for $(6,0)\&(12,0)$, $(7,0)\&(14,0)$ and $(8,0)\&(16,0)$ -DWCNTs, respectively, reference to their corresponding averaged C-C bond distances for the SWCNTs. These predictions explicitly indicate the existence of intertube interactions in DWCNT systems, which may be expressed by a van der Waals type interaction, not like chemical bonding interactions in the ground state. Furthermore, Figure 3.2.1B provides the calculated electron density of $(0,6)\&(0,12)$ -DWCNT showed that first four highest occupied molecular orbitals (from HOMO to HOMO-3 with the A_{1u} , A_{2g} and $2E_{1g}$ symmetries, respectively) belong to the outer-shell and the next highest occupied molecular orbitals from HOMO-4 to HOMO-24 include both inner- and outer-shells of $(0,6)\&(0,12)$ -DWCNT. The lowest unoccupied molecular orbital, LUMO (E_{1u}) lies about 0.780 eV above the HOMO (A_{1u}) belongs to the outer-shell and the next one (B_{2u}) belongs to the inner-shell and lies 0.849 eV above the HOMO (A_{1u}). The calculated electron density also indicated that an intratube (inner and outer tube) interaction may possibly take place in the excited state: the LUMO+7 with A_{2u} symmetry and 2.494 eV above the HOMO (A_{1u}), LUMO+8 (E_{1u} and 2.557 eV), LUMO+10 (E_{1g} and 2.563 eV) and LUMO+15 (E_{1g} and 3.637 eV). The intratube CC σ -bonding interaction in the excited state might lead to a probable intertube charge transfer, which can be observed by a significant

change in the tangential modes (TM) range of Raman spectra when the tube excited to its intratube charge transfer state. The TM may not only provide information about the metallic or semiconducting character of nanotubes, but also on the inner-outer tube (intratube) charge transfer. In addition, very recently, Resonant Raman measurements,[96] photoemission measurements and theoretical calculations provide a evidence of charge transfer between the inner- and outer-shells of DWCNTs.

Based on this scenario, the small sized-DWCNTs can be used as energy conversion systems as a consequence of charge transfer between intershells. This illustration also can reflect on the intensity of the Raman bands at the excitation energy where the charge transfer takes place between inner- and outer-shells. For (0,7)&(0,14)- and (0,8)&(0,16)-DWCNTs, the plotted electron densities did not signify any intratube CC antibonding in the excited state up to 4 eV above the ground state.

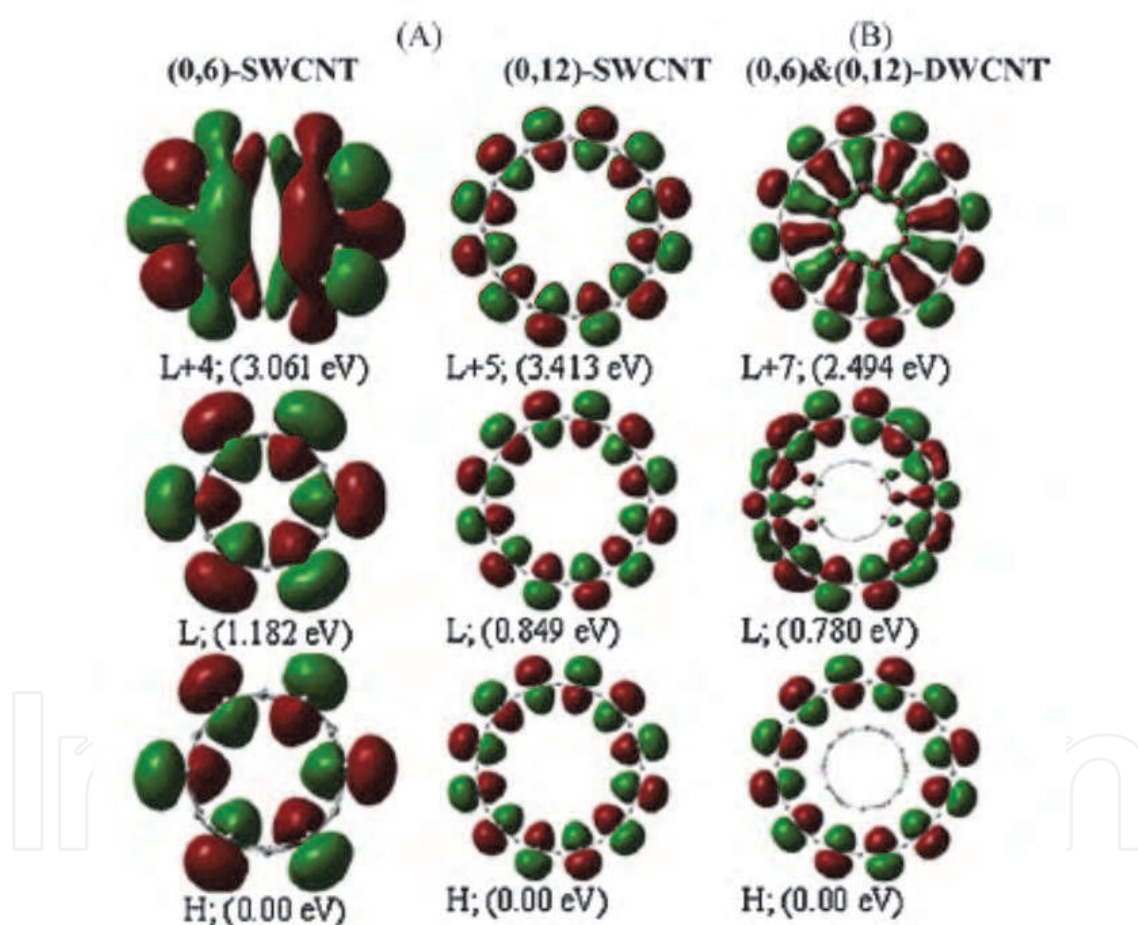


Fig. 3.2.1. Calculated electron densities in the lowest HOMO and LUMO states: (A) for the (0,6)- and (0,12)-SWNTs and (B) for the (0,6)&(0,12)-DWCNT.

3.3 Raman spectra

We calculated Raman spectra of the (n, m) -nanotubes with $n = 6$ to 19 for the zigzag nanotube, $n = m = 3$ to 12 for the armchair nanotube, and $n = 6$ to 10 and $m = 2$ for the chiral nanotube; for the zigzag and armchair single-wall boron nitride nanotubes (SWBNNTs) chiral index (n, m) ranging from $n = 7$ to 19 and $n = m = 3$ to 10, respectively. For the $(n, 0)$ -

SWCNTs with $n = 6$ to 11 and the (8, 0)-boron nitride nanotubes, the length dependence of the Raman spectra was also calculated at the same level of the DFT. The calculated Raman spectra of the carbon and boron nitride nanotubes illustrate similar structure. Therefore, in this chapter, we will comprehensively discuss the (n,0)-SWCNTs only.

3.3.1 Raman spectra of (n,0)-SWCNTs

Figure 3.3.1 provides the calculated Raman spectra of the zigzag (n,0)-SWCNTs with n ranging from 6 to 19. Table 3.3.1 provides vibrational mode assignments and frequencies, while Figure 3.3.2A provides diagrams of the atomic motions associated with the vibrational frequencies for the (11,0)-SWCNT, used as a representative case. All assignments to motions of atoms or groups of atoms in Table 3.3.1 have been accomplished through use of vibration visualization software (specifically, GaussView03). The calculated Raman spectra indicate that there are two additional Raman bands besides the RBM in the low frequency region.

The frequencies of these latter bands are also found to depend on SWCNT diameter, as shown in Figure 3.3.1A, and Figure 3.3.1B indicate the calculated vibrational frequencies as a function diameters of SWCNTs. As seen in Figure 3.3.1B, the RBM (with A_{1g} symmetry) and two other Raman bands (with E_{1g} and E_{2g} symmetries) have frequencies that inversely depend on a nanotube's diameter. A linear fit to the calculate RBM frequency dependence on nanotube diameter is provided; a linear equation, $\omega_{\text{RBM}}(A_{1g}) = 12.04(\text{cm}^{-1}) + \frac{221.4(\text{nm}\cdot\text{cm}^{-1})}{d_t(\text{nm})}$, is in excellent agreement with the empirically determined expression[97]; indeed, a popular one has the value 12.5 for the offset constant and 223.5 for the constant shift parameter that appear on the r-h-s of Eq. 2. Even though a linear equation reproduces the RBMs within about $\pm 3 \text{ cm}^{-1}$ error ranges for the large size SWCNTs, it overestimates RBMs for (0, $n < 7$)-SWCNTs which have diameters smaller than 0.55 nm such as about 14 cm^{-1} for (0,6)-SWCNT. In actual fact, this is not so surprising, because the C-C-C bond strain rapidly increases with decreasing CNTs diameters (as seen in Figure 3.1.1), the plot of curvature energy per hexagon of the isolated-SWCNTs. Therefore, the best fitting may be obtained using a quadratic fitting equation as given in Equation 3.3.1, which reproduces the RBMs within $\pm 2 \text{ cm}^{-1}$ error ranges when comparing with the calculated Raman spectra of the SWCNTs from (0,6) to (0,19) by the DFT technique.

$$\omega_{\text{RBM}}(A_{1g}) = -14.12(\text{cm}^{-1}) + \frac{269.67(\text{nm}\cdot\text{cm}^{-1})}{d_t(\text{nm})} - \frac{20.24(\text{nm}^2\cdot\text{cm}^{-1})}{[d_t(\text{nm})]^2} \quad (3.3.1)$$

Even though the corresponding linear fit to the two other accompanying calculated low frequency bands (ω_{BD} of E_{1g} symmetry and ω_{ED} of E_{2g} symmetry) as functions of the inverse of the SWCNT diameter may be given linear equations such as: $\omega_{\text{BD}}(E_{1g}) = 51.9(\text{cm}^{-1}) + \frac{136.8(\text{nm}\cdot\text{cm}^{-1})}{d_t(\text{nm})}$ and $\omega_{\text{ED}}(E_{2g}) = -43.8(\text{cm}^{-1}) + \frac{80.9(\text{nm}\cdot\text{cm}^{-1})}{d_t(\text{nm})}$, the best fittings are provided in Equations 3.3.3a-b and 3.3.4, respectively. It is to be noted that both the E_{1g} and E_{2g} bands have lower frequencies than the RBM, with the E_{2g} band being of lowest frequency (see Figure 3.3.1B). These two latter bands are labeled as BD for bonding deformation and ED for elliptical deformation, which derives from the predominate motions that define vibrational mode motions, as ascertained with the vibration visualization software mentioned earlier (see Table 3.3.1). Furthermore, the calculated E_{2g} band for (0,2n)-SWCNTs

is not only diameter dependent, but is also dependent on whether the number of hexagons formed in the circumference direction of the SWCNTs (0,2n) type or (0,2n+1) type, respectively are even or odd. As shown in Figure 3.3.1B, the E_{2g} band for (0,2n) and (0,2n+1) type SWCNTs is well separated with decreasing tube diameter, but they again join together at the large tube diameters. Therefore, in order to obtain a more precise fitting equation for this Raman band (of symmetry E_{2g}), we obtained two fitting equations as given in Eq. 3.3.3a for (0, 2n) type SWCNTs and Eq. 3b for (0,2n+1) type SWCNTs.

$$\omega_{BD}(E_{1g}; (2n, 0)) = 4.15(\text{cm}^{-1}) + \frac{227.82(\text{nm} \cdot \text{cm}^{-1})}{d_t(\text{nm})} - \frac{33.60(\text{nm}^2 \cdot \text{cm}^{-1})}{[d_t(\text{nm})]^2} \quad (3.3.3a)$$

$$\omega_{BD}(E_{1g}; (2n + 1, 0)) = -0.43(\text{cm}^{-1}) + \frac{224.23(\text{nm} \cdot \text{cm}^{-1})}{d_t(\text{nm})} - \frac{37.34(\text{nm}^2 \cdot \text{cm}^{-1})}{[d_t(\text{nm})]^2} \quad (3.3.3b)$$

$$\omega_{ED}(E_{2g}; (n, 0)) = -0.31(\text{cm}^{-1}) + \frac{1.13(\text{nm} \cdot \text{cm}^{-1})}{d_t(\text{nm})} + \frac{33.23(\text{nm}^2 \cdot \text{cm}^{-1})}{[d_t(\text{nm})]^2} \quad (3.3.4)$$

Moreover, as seen in Figure 3.3.1B, for large sized SWCNTs, the $\omega_{RBM}(A_{1g})$ and $\omega_{BD}(E_{1g})$ mode frequencies converge. The calculated frequency separation between the RBM and BD to found to be 0, 5, 9 and 14 cm^{-1} , respectively, when n has the values 27, 24, 22 and 20. Thus, one can anticipate the (27,0)-SWCNT would have unresolvable RBM and BD bands. We can anticipate, in general, that the acquisition of Raman spectra for experimental samples consisting of large diameter SWCNT with the purpose of characterizing the sample in terms of electronic properties and purity may be complicated by the existence of this BD band, which can lead to apparent broadening of bands as well as the presence of additional bands that may lead to the erroneous conclusion that more than one type of SWCNT is present in the sample.

As regards other general conclusions that can be drawn from our calculations for the SWCNTs, we note that the lowest frequency $\omega_{ED}(E_{2g})$ mode may not be observable for large diameter nanotube due to Rayleigh scattering; however, our calculation suggests that (6,0) and (7,0) zigzag SWCNTs, with computed ω_{ED} 's of 145.5 and 110.8 cm^{-1} , should be resolvable from Rayleigh scattering. Also, we have found that calculated Raman bands in the mid-frequency region exit nearly size-independent peak positions. While, as indicated in Table 3.3.1 or Figure 3.3.1C and 3.3.1E, in the high-frequency region there are three Raman bands of symmetries $E_{1g}/E_{2g}/A_{1g}$ that lie close to one another. Raman bands A_{1g} symmetry essentially remain constant for (2n,0) type CNTs (with band position $1526 \pm 0.5 \text{ cm}^{-1}$, see Fig. 3.3.1E), but that for (2n+1,0) type CNTs are diameter dependent (Fig. 3.3.1C), $A_{1g}(1486-1525 \text{ cm}^{-1}$ or $1526(\text{cm}^{-1}) + \frac{3.55(\text{nm} \cdot \text{cm}^{-1})}{d_t(\text{nm})} - \frac{14.86(\text{nm}^2 \cdot \text{cm}^{-1})}{[d_t(\text{nm})]^2}$). We further observe that the E_{1g} ($\sim 1547 \pm 25 \text{ cm}^{-1}$) and E_{2g} ($\sim 1532 \pm 12 \text{ cm}^{-1}$) Raman modes first approach one another in frequency then separates as one calculates these frequencies for increase diameter of the SWCNT. These shifts in the peak positions may result from the nanotube curvature effect. The curvature energy (as given by Eq. 1) of the nanotube brings about dissimilar force constants along the nanotube axis and the circumference direction. Therefore, the nanotube geometry causes a force constant reduction along the tube axis compared to that in the circumferential direction. As a result, the curvature effect might play crucial role in the shift of the peak positions of the G-band as well as the RBM band as mentioned earlier. Furthermore, we

might note that these Raman bands, since they are overlapping, might pose a problem in assessing, based on the shape of bands in this transverse vibrations region, whether SWCNT samples are metallic or semiconducting. In addition, the calculated Raman band positions for bands around 1330 cm^{-1} , the disordered graphite region are found to be slightly size dependent, exhibiting a small blue shift with increasing diameter of the SWCNTs.

IntechOpen

	(19,0)	(18,0)	(17,0)	(16,0)	(15,0)	(14,0)	(13,0)	(12,0)	(11,0)	(10,0)	(9,0)	(8,0)	(7,0)	(6,0)	Assignment
E_{1g}	1586.9 1507.7	1508.7	1510.8	1525.6	1536.0	1542.1	1550.8	1558.3	1564.6	1571.2	1575.6	1576.5	1574.0	1550.2	Skeletal deformation due to the asymmetric stretching of the C-C-C bonds: $\nu_{2d}(C-C-C)$
E_{2g}	1525.5	1537.3	1537.6	1539.3	1533.1	1541.8	1533.6	1544.2	1536.8	1543.7	1534.3	1533.8	1515.6	1498.3	Skeletal deformation due to the stretching of the C-C bonds along the tube axis: $\nu(C-C)$; asymmetric stretching of the C-C-C bonds: $\nu_{2d}(C-C-C)$. Note that wagging of CH bonds also occurs
A_{1g}	1524.3	1527.9	1542.7	1527.5	1521.2	1527.6	1518.2	1527.7	1512.9	1528.2	1503.4	1527.8	1486.2	1526.6	Skeletal deformation due to the stretching of the C-C bonds, $\nu(C-C-C)$ and $\nu(C-C)$ along the tube axis
E_{2g}	1399.1	1402.7	1408.3 weak	1410.5	1411.7	1417.5	1417.9	1422.9	1421.6	1423.8	1421.3	1415.9	1411.7	1375.8	Skeletal deformation due to asymmetric and symmetric stretching of the C-C-C bonds: $\nu(C-C-C)$ and $\nu_s(C-C-C)$, and C-C bond stretching along the nanotube axis, $\nu(C-C)$
E_{2g}	472.2	463.9	450.9	464.9 457.8	477.1	471.0 462.6 442.2	479.7	464.2	483.3	467.1 461.2	489.1	478 454.4	500 463 461.2	402.0	Bending deformation of the C-C-C bonds in the radial direction. Also contribution from the wagging of the CH bonds along tube circumference
A_{1g}	158.9	167.6	177.0	188.2	200.3	214.3	230.3	248.7	270.3	295.8	326.8	362.9	410.2	457.1	Radial breathing mode of CNT
E_{1g}	132.9	147.4	148.5	163.9	163.9	183.6	184.9	208.0	209.9	238.5	242.2	278.3	284.4	332.4	Bending deformation of the CNT due to expansion of the CNT along diagonal axis, with the motion of two end groups being in opposite directions
E_{2g}	15.4	17.1	18.9	21.9	24.7	28.3	32.9	38.4	46.1	54.7	68.4	83.7	110.8	145.5	Stretching of the CNT along its diameter, resulting in an elliptical shape

Table 3.3.1 DFT-calculated Raman vibrational frequencies (in cm^{-1}) and assignments for (n,0)-CNT at the B3LYP/6-31G level.

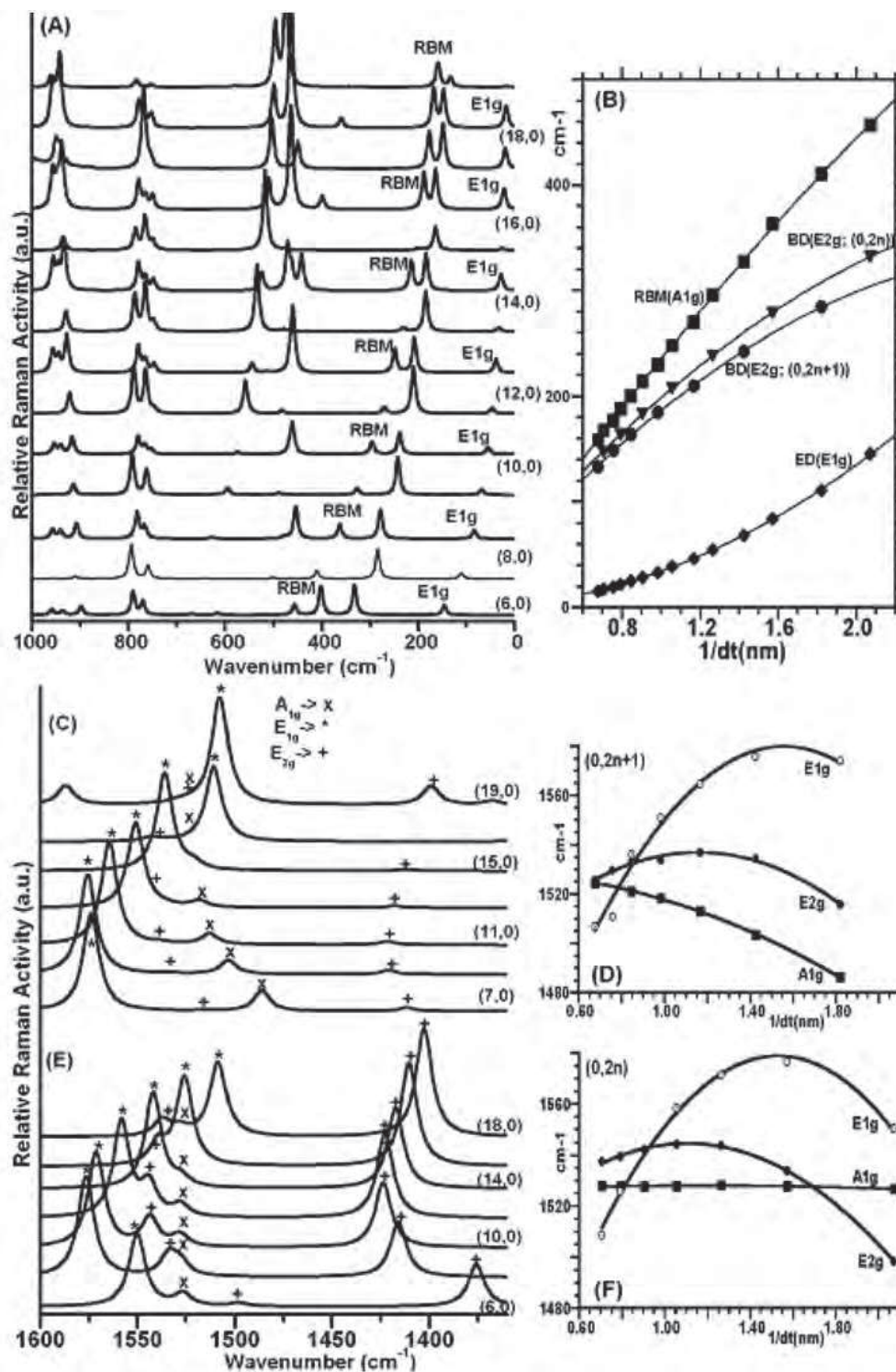


Fig. 3.3.1. Calculated Raman spectra: **(A)** increased resolution in the low frequency region, showing diameter dependence of the calculated Raman band frequencies for the $(n, 0)$ -SWCNTs, $n = 0$ to 19; **(B)** the plots of the frequencies of vibrational modes of symmetries A_{1g} , E_{1g} and E_{2g} versus $1/dt$; in the high energy region: **(C)** for $(2n+1,0)$ -SWCNTs, **(D)** the plots of the frequencies of vibrational modes of symmetries A_{1g} , E_{1g} and E_{2g} versus $1/dt$; **(E)** for $(2n,0)$ -SWCNTs, **(F)** the plots of the frequencies of vibrational modes of symmetries A_{1g} , E_{1g} and E_{2g} versus $1/dt$. Where the signs; x , $*$ and $+$ stand for A_{1g} , E_{1g} and E_{2g} , respectively.

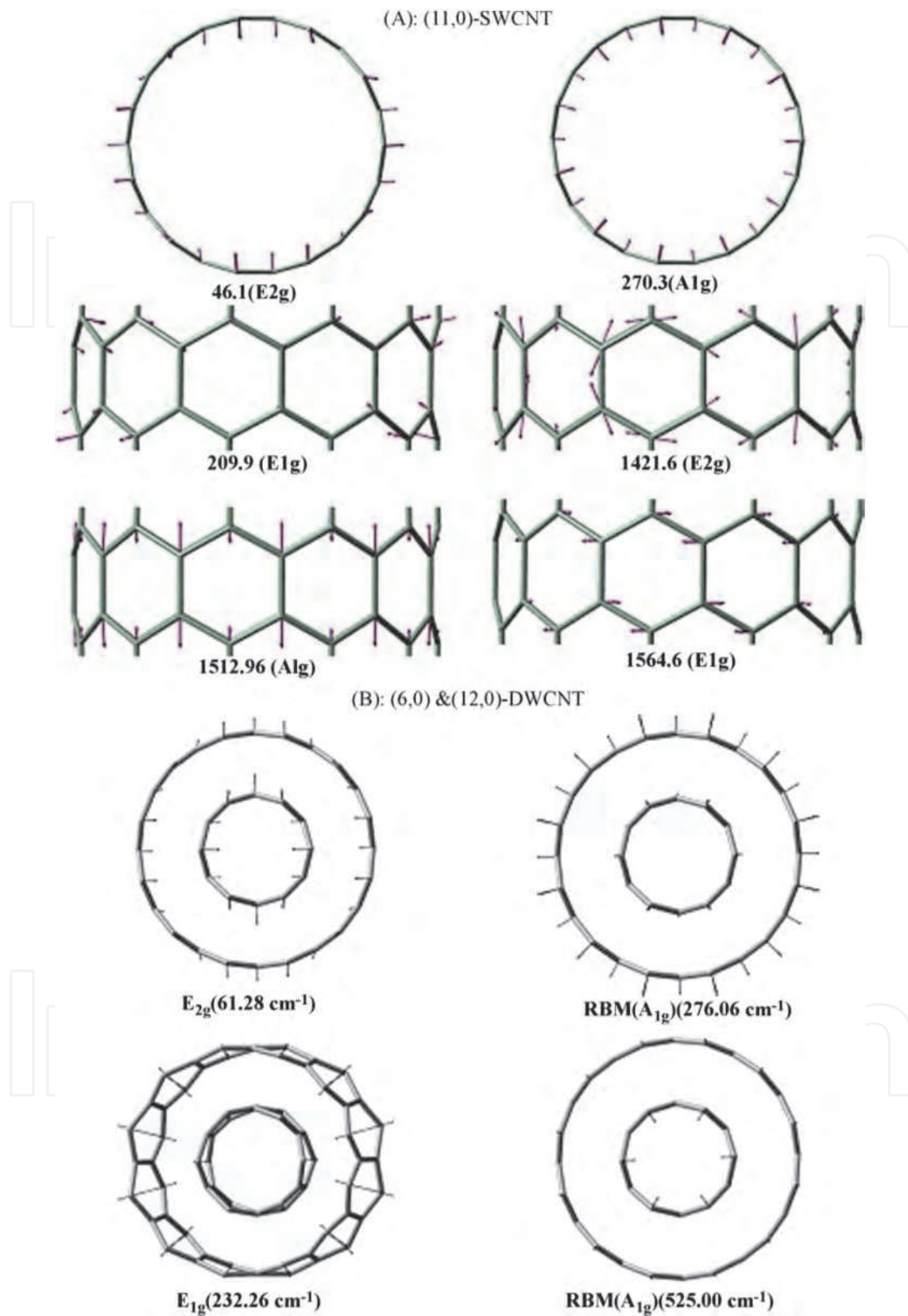


Fig. 3.3.2. Calculated molecular motions for some vibrational bands of the (11,0)-SWNT and (6,0)&(12,0)-DWCNT. The nuclear motions of the other SWNTs studied are provided in Table 3.3.1.

3.3.2 Raman spectra of the (n,n) and (n,2)-SWCNTs

The calculated Raman spectra of armchair (n, n)- and (n,2) SWCNTs exhibited similar structure to these of zigzag-SWCNTs. Figure 3.3.3A provide the calculated Raman spectra of the (n,n)-SWCNTs. As seen in the Figure 3.3.3A-B, RBM(A_{1g}), ED(E_{1g}) and BD(E_{2g}) bands of vibrational frequencies in the Raman spectra are strongly diameter dependent, but there is no significant change in the calculated Raman bands with the symmetry E_{2g} for even and number of chiral index n as observed in the Raman spectra of the (n,0)-SWCNTs (see Figure 3.3.1A-B). Figure 3.3.3B shows the calculated vibrational frequencies as a function of the tube's diameter. As given in Figure 3.3.3A, the RBM (with A_{1g} symmetry) and two other Raman bands (with E_{1g} and E_{2g} symmetries) have frequencies that inversely depend on a nanotube's diameter. A linear fit to the calculate RBM(A_{1g}), ED(E_{1g}) and BD(E_{2g}) frequency dependence on nanotube diameter is given in equations 3.3.5a-c;

$$\omega_{\text{RBM}}(A_{1g}) = -12.13(\text{cm}^{-1}) + \frac{270.52(\text{nm}\cdot\text{cm}^{-1})}{d_t(\text{nm})} - \frac{54.34(\text{nm}^2\cdot\text{cm}^{-1})}{[d_t(\text{nm})]^2} \quad (3.3.5a)$$

$$\omega_{\text{BD}}(E_{2g}) = 24.72(\text{cm}^{-1}) + \frac{136.81(\text{nm}\cdot\text{cm}^{-1})}{d_t(\text{nm})} - \frac{5.33(\text{nm}^2\cdot\text{cm}^{-1})}{[d_t(\text{nm})]^2} \quad (3.3.5b)$$

$$\omega_{\text{ED}}(E_{1g}) = -0.79(\text{cm}^{-1}) + \frac{6.56(\text{nm}\cdot\text{cm}^{-1})}{d_t(\text{nm})} + \frac{22.10(\text{nm}^2\cdot\text{cm}^{-1})}{[d_t(\text{nm})]^2} \quad (3.3.5b)$$

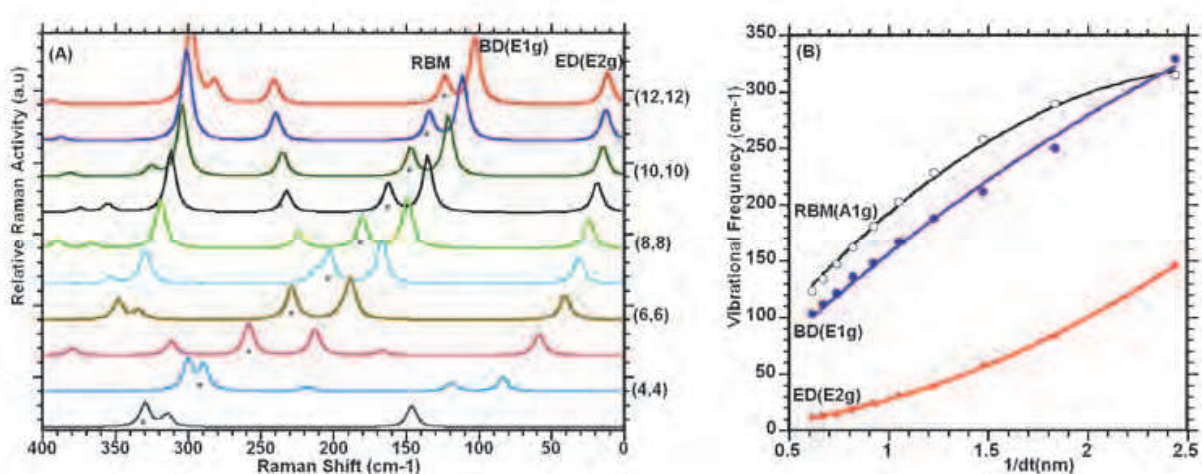


Fig. 3.3.3. Calculated Raman spectra: (A) increased resolution in the low frequency region, showing diameter dependence of the calculated Raman band frequencies for the (n, n)-SWCNTs, $n = 3$ to 12; (B) the plots of the frequencies of vibrational modes of symmetries A_{1g} , E_{1g} and E_{2g} versus $1/dt$.

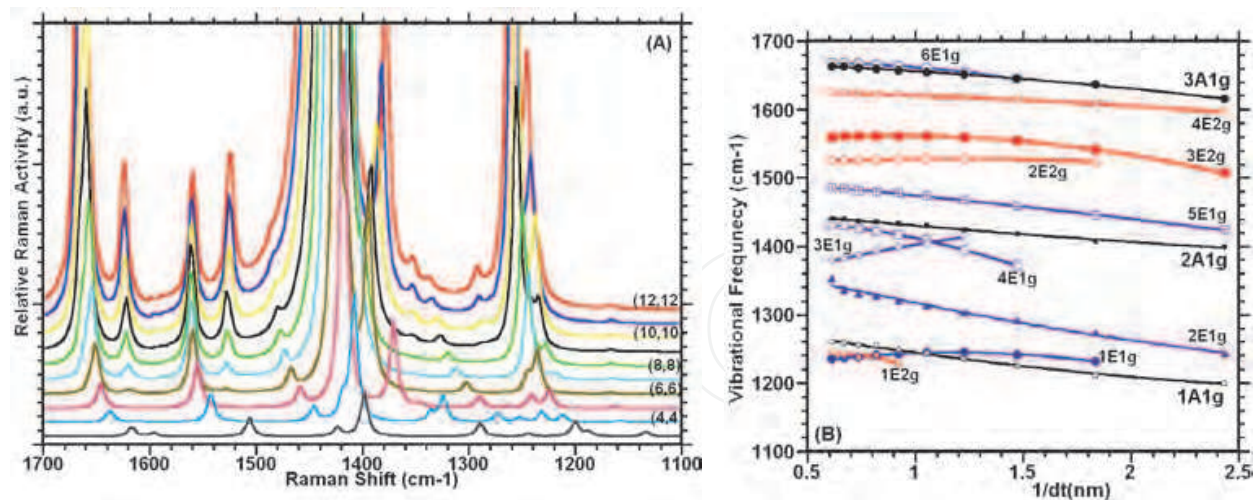


Fig. 3.3.4. Calculated Raman spectra: **(A)** increased resolution in the high frequency region, showing to some extent diameter dependence of the calculated Raman band frequencies for the (n, n) -SWCNTs, $n = 3$ to 12; **(B)** the plots of the frequencies of vibrational modes of symmetries A_{1g} , E_{1g} and E_{2g} versus $1/dt$.

In the high energy region, the calculated Raman spectra exhibit many Raman active spectra in range of 1200-1700 cm^{-1} as seen in Figure 3.3.4A, which are also slightly diameter dependent. As seen in Figure 3.3.4B, a linear fit to the calculate A_{1g} , E_{1g} and E_{2g} frequency dependence on the diameter of the nanotube is given in equations 3.3.6a-l;

$$\omega(3A_{1g}) = 1670.16(\text{cm}^{-1}) - \frac{8.06(\text{nm}\cdot\text{cm}^{-1})}{d_t(\text{nm})} - \frac{5.76(\text{nm}^2\cdot\text{cm}^{-1})}{[d_t(\text{nm})]^2} \quad (3.3.6a)$$

$$\omega(6E_{1g}) = 1662.50(\text{cm}^{-1}) + \frac{24.47(\text{nm}\cdot\text{cm}^{-1})}{d_t(\text{nm})} - \frac{24.77(\text{nm}^2\cdot\text{cm}^{-1})}{[d_t(\text{nm})]^2} \quad (3.3.6b)$$

$$\omega(4E_{2g}) = 1627.18(\text{cm}^{-1}) - \frac{1.88(\text{nm}\cdot\text{cm}^{-1})}{d_t(\text{nm})} - \frac{4.47(\text{nm}^2\cdot\text{cm}^{-1})}{[d_t(\text{nm})]^2} \quad (3.3.6c)$$

$$\omega(3E_{2g}) = 1541.74(\text{cm}^{-1}) + \frac{43.73(\text{nm}\cdot\text{cm}^{-1})}{d_t(\text{nm})} - \frac{23.28(\text{nm}^2\cdot\text{cm}^{-1})}{[d_t(\text{nm})]^2} \quad (3.3.6d)$$

$$\omega(2E_{2g}) = 1515.45(\text{cm}^{-1}) + \frac{21.33(\text{nm}\cdot\text{cm}^{-1})}{d_t(\text{nm})} - \frac{9.08(\text{nm}^2\cdot\text{cm}^{-1})}{[d_t(\text{nm})]^2} \quad (3.3.6e)$$

$$\omega(5E_{1g}) = 1502.66(\text{cm}^{-1}) - \frac{24.66(\text{nm}\cdot\text{cm}^{-1})}{d_t(\text{nm})} - \frac{3.20(\text{nm}^2\cdot\text{cm}^{-1})}{[d_t(\text{nm})]^2} \quad (3.3.6f)$$

$$\omega(2A_{1g}) = 1460.21(\text{cm}^{-1}) - \frac{32.55(\text{nm}\cdot\text{cm}^{-1})}{d_t(\text{nm})} + \frac{2.90(\text{nm}^2\cdot\text{cm}^{-1})}{[d_t(\text{nm})]^2} \quad (3.3.6g)$$

$$\omega(4E_{1g}) = 1437.00(\text{cm}^{-1}) + \frac{16.41(\text{nm}\cdot\text{cm}^{-1})}{d_t(\text{nm})} - \frac{41.16(\text{nm}^2\cdot\text{cm}^{-1})}{[d_t(\text{nm})]^2} \quad (3.3.6h)$$

$$\omega(3E_{1g}) = 1389.42(\text{cm}^{-1}) - \frac{81.32(\text{nm}\cdot\text{cm}^{-1})}{d_t(\text{nm})} + \frac{8.94(\text{nm}^2\cdot\text{cm}^{-1})}{[d_t(\text{nm})]^2} \quad (3.3.6i)$$

$$\omega(2E_{1g}) = 1329.12(\text{cm}^{-1}) + \frac{94.23(\text{nm}\cdot\text{cm}^{-1})}{d_t(\text{nm})} - \frac{20.70(\text{nm}^2\cdot\text{cm}^{-1})}{[d_t(\text{nm})]^2} \quad (3.3.6j)$$

$$\omega(1A_{1g}) = 1295.48(\text{cm}^{-1}) - \frac{58.27(\text{nm}\cdot\text{cm}^{-1})}{d_t(\text{nm})} + \frac{7.64(\text{nm}^2\cdot\text{cm}^{-1})}{[d_t(\text{nm})]^2} \quad (3.3.6k)$$

$$\omega(1E_{1g}) = 1201.23(\text{cm}^{-1}) + \frac{73.99(\text{nm}\cdot\text{cm}^{-1})}{d_t(\text{nm})} - \frac{31.24(\text{nm}^2\cdot\text{cm}^{-1})}{[d_t(\text{nm})]^2} \quad (3.3.6l)$$

The calculated Raman bands with symmetry labeled as $3A_{1g}$ and $6E_{1g}$ are almost overlapping and other bands also close to one other. As observed in low frequency region, the diameter dependence of the Raman band in high energy region is somewhat different than these found in the Raman spectra of the $(n,0)$ -SWCNTs.

The calculated Raman spectra of the $(n,2)$ -SWCNTs (see Figure 3.3.5), with $n = 5$ to 10 , did not only exhibit the dependence on the diameter of the nanotube, but also relatively complicated than the calculated Raman spectra of the armchair- and zigzag-type carbon nanotubes. In order to provide a reliable fitting equations for the diameter dependence of the RBM(A_{1g}), ED(E_{1g}) and BD(E_{2g}) bands of vibrational frequencies in low energy region, the number of calculated Raman spectra for the chiral nanotube is not large enough; therefore, based on the present data, tentative fitting equations for the diameter dependence of these three Raman bands in the low energy region may be given by equations 3.3.7a-c.

$$\omega_{\text{RBM}}(A_{1g}) = -12.11 + \frac{233.62(\text{nm}\cdot\text{cm}^{-1})}{d_t(\text{nm})} + \frac{0.64(\text{nm}^2\cdot\text{cm}^{-1})}{[d_t(\text{nm})]^2} \quad (3.3.7a)$$

$$\omega_{\text{BD}}(E_{2g}) = 20.12 + \frac{94.37(\text{nm}\cdot\text{cm}^{-1})}{d_t(\text{nm})} + \frac{10.29\text{nm}^2\cdot\text{cm}^{-1}}{[d_t(\text{nm})]^2} \quad (3.3.7b)$$

$$\omega_{\text{ED}}(E_{1g}) = 2.45 + \frac{11.63(\text{nm}\cdot\text{cm}^{-1})}{d_t(\text{nm})} + \frac{21.29(\text{nm}^2\cdot\text{cm}^{-1})}{[d_t(\text{nm})]^2} \quad (3.3.7c)$$

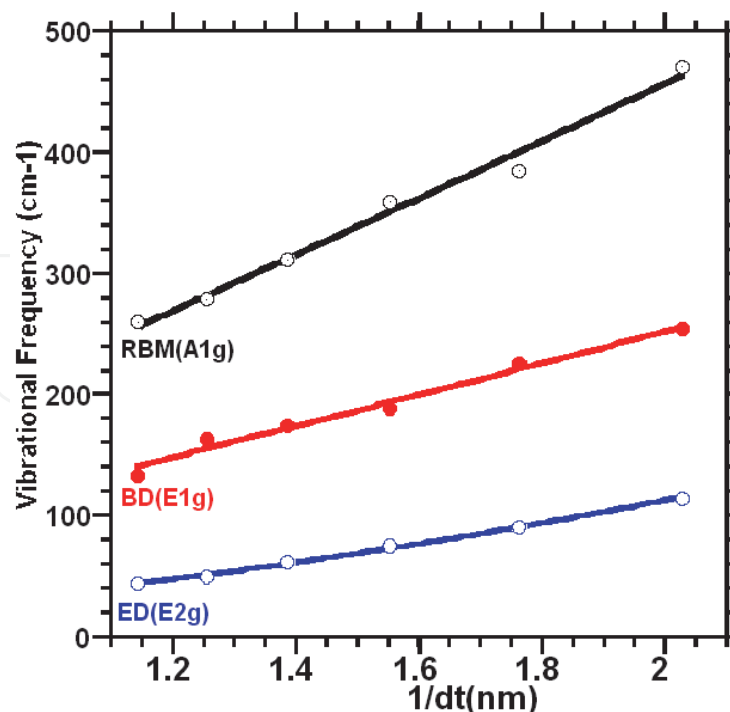


Fig. 3.3.5. The plots of the frequencies of vibrational modes of symmetries A_{1g} , E_{1g} and E_{2g} versus $1/d_t$ for the chiral $(n, 2)$ -SWCNTs with $n = 5$ to 10 .

3.3.3 Dependence of the RBM Band on the length of nanotube

We calculated Raman spectra of the zigzag (n,0)-SWCNTs as a function of m (number of hexagon along the nanotube axis or length of the tube), where n = 6 to 11 and m = 1 to 5, at same level of the DFT. The results of the calculations showed that the RBMs(A_{1g}) is also slightly dependent on the m (length of the nanotube) even if its dependence is not as strongly dependent on the diameter. When we plotted the RBMs as function of the m with a desired nanotube, for instance, for the (6,0)-SWCNT, the dependence of the calculated RBMs on the m are not compatible with one other, except for (10,0) and (11,0)-SWCNT. For these two latter SWCNTs, the RBMs slightly decreased with increasing value of m. On the contrary, as seen in Figure 3.3.6A, the plot of the calculated RBMs as function of diameter for a desired length (m), each curve for the RBMs data is in excellent agreement with one other for each of the number of hexagon along the tube axis (m) as shown in Figure 3.3.6C. The fitting equations for each set of the m are given by equations 3.3.8a-d. The fitting parameters for each set of the m are well consistent with each other. It should be noticed that for the fitting equations, we set the constant parameter to -14.1 cm^{-1} and excluded two RBMs of frequencies at 498.9 cm^{-1} and 445.9 cm^{-1} for the (6,0)- and (7,0)-SWCNT with the $m=3$, respectively, in order to obtain a best fitting to calculated data.

$$\omega_{\text{RBM}}(A_{1g}; m = 1) = -14.1 + \frac{274.93(\text{nm.cm}^{-1})}{d_t(\text{nm})} - \frac{24.57(\text{nm}^2.\text{cm}^{-1})}{[d_t(\text{nm})]^2} \quad (3.3.8a)$$

$$\omega_{\text{RBM}}(A_{1g}; m = 2) = -14.1 + \frac{257.22(\text{nm.cm}^{-1})}{d_t(\text{nm})} - \frac{14.03(\text{nm}^2.\text{cm}^{-1})}{[d_t(\text{nm})]^2} \quad (3.3.8b)$$

$$\omega_{\text{RBM}}(A_{1g}; m = 3) = -14.1 + \frac{248.95(\text{nm.cm}^{-1})}{d_t(\text{nm})} - \frac{9.69(\text{nm}^2.\text{cm}^{-1})}{[d_t(\text{nm})]^2} \quad (3.3.8c)$$

$$\omega_{\text{RBM}}(A_{1g}; m = 4) = -14.1 + \frac{304.09(\text{nm.cm}^{-1})}{d_t(\text{nm})} - \frac{34.53(\text{nm}^2.\text{cm}^{-1})}{[d_t(\text{nm})]^2} \quad (3.3.8d)$$

Figure 3.3.6B-C and Table 3.3.2 provides the calculated ED(E_{1g}) mode of frequencies and the calculations indicated that the ED(E_{1g}) mode of frequencies are almost length independent. Furthermore, we calculated length dependence of the Raman spectra for the (4,4)-SWCNTs. The calculations showed that the length dependence of the RBM bands slightly change with the number of hexagon along the nanotube axis.

m	RBM(A_{1g}) in cm^{-1}						ED(E_{1g}) in cm^{-1}					
	(6,0)	(7,0)	(8,0)	(9,0)	(10,0)	(11,0)	(6,0)	(7,0)	(8,0)	(9,0)	(10,0)	(11,0)
1	457,1	410,2	362,9	326,8	295,8	270,3	145.5	110.8	83.7	68.4	54.7	46.1
2	467,3	414,0		319,0	291,8	266,0	139.38	109.82		67.6	54.4	44.94
3	498,9	445,9	356,6	325,2	284,5	262,1	145.12	106.97	88.6	66.99	56.26	45.76
4	476,7	426,	383,3				146.24	105.27	88.24			
5	484,4	421,6					142.67	105.78				

Table 3.3.2. The calculated length (the number of hexagon along the nanotube axis, m = 1 to 5) dependence of the RBM(A_{1g}) and ED(E_{1g}) modes at B3LYP/6-31G level of the DFT for the zigzag (n,0)-SWCNTs, with n = 6 to 11.

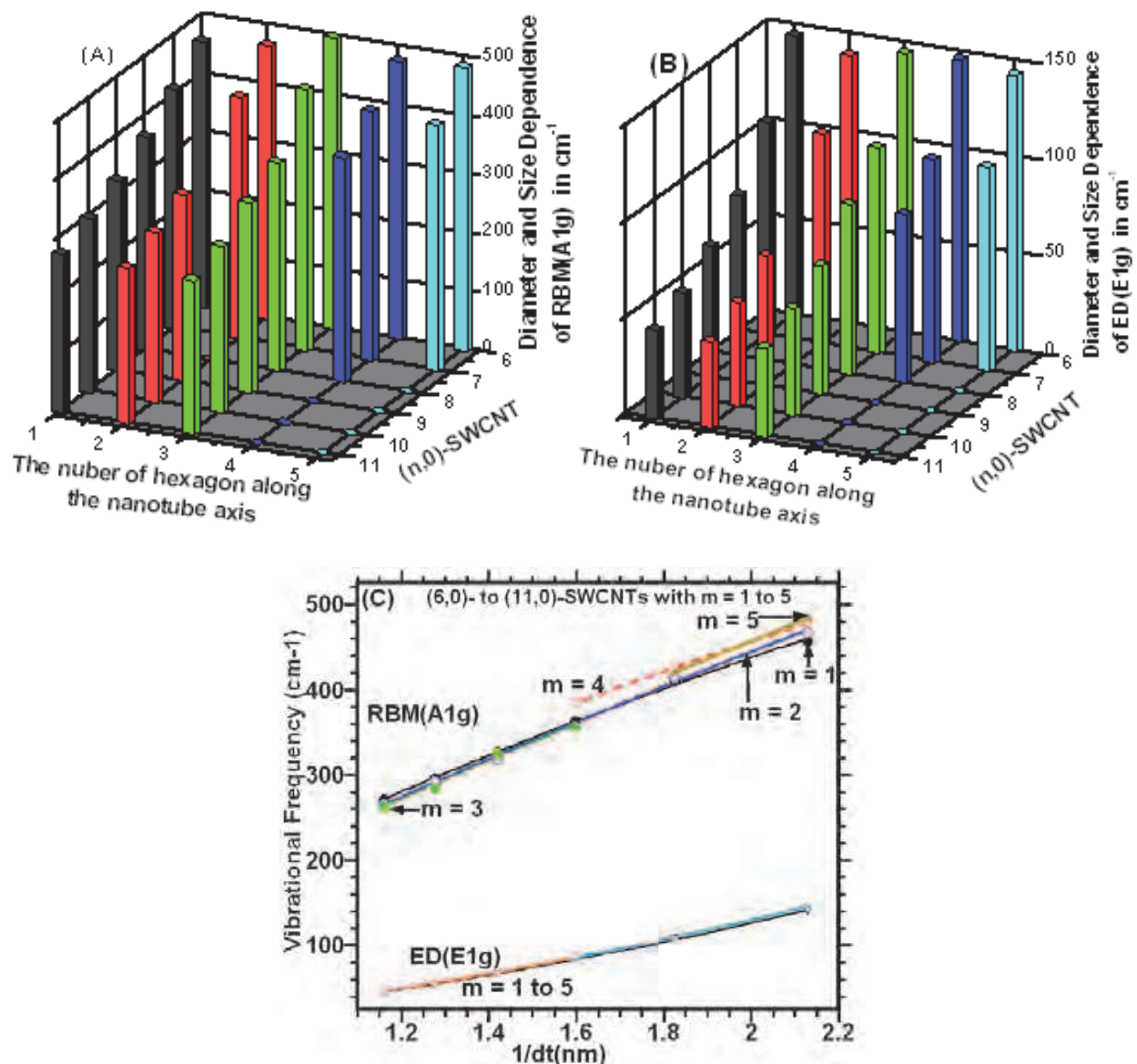


Fig. 3.3.6. The calculated dependence of the Raman modes on the diameter and length (the number of hexagon ($m = 1$ to 5) along the nanotube axis) of the nanotubes: (A) for the RBM(A_{1g}); (B) for the ED(E_{1g}) for the zigzag ($n, 0$)-SWCNTs with $n = 6$ to 11 ; and (C) illustrates the plot of the RBM and ED modes as function of the m .

3.3.4 Raman spectra for DWCNTs

Figure 5 provides the calculated Raman spectra of (0,6)&(0,12) and (0,7)&(0,14)-DWCNTs in the low energy region. The calculations showed that the frequencies of the RBMs and tangential modes (TMs) of DWCNT significantly differ from those calculated for SWCNT. The calculated Raman spectra of these DWCNTs exhibited two RBM modes resulting from the radial motion of the inner- and outer-shells, in-phase and out-of-phase, as seen in Figure 3B, and both of these RBM modes are strongly diameter dependent. A large gap between RBMs of DWCNT decreases with increasing diameter of the inner- and outer-shells. Comparing these calculated RBMs with their corresponding ones in the SWCNTs spectra, we noticed that the RBMs at 457 cm⁻¹ in the Raman spectrum of (6,0)-SWCNT and at 249 cm⁻¹

in the (12,0)-SWCNT spectrum are respectively blue-shifted to 525 cm⁻¹ and 276 cm⁻¹ in the Raman spectrum of (6,0)&(12,0)-DWCNT. Additionally, the RBMs for (7,0)-SWCNT (410 cm⁻¹) and (14,0)-SWCNT (214 cm⁻¹) are respectively upward shifted to 450 cm⁻¹ and 237 cm⁻¹ in the spectrum of (7,0)&(14,0)-DWCNT. The relative distances between RBMs in the spectrum of (n,0)&(2n,0)-DWCNTs are larger than the distances between corresponding RBMs in Raman spectra of (n,0)- and (2n,0)-SWCNTs. Even though we do not have enough data for the calculated RBMs for different sized DWCNTs, a tentative equation for the RBMs may be given by equations below;

$$\omega_{\text{inner}}(\text{RBM}) = 62\text{cm}^{-1} + \frac{138(\text{nm}\cdot\text{cm}^{-1})}{d_t(\text{nm})} + \frac{39(\text{nm}^2\cdot\text{cm}^{-1})}{(d_t(\text{nm}))^2} \quad (3.3.9a)$$

$$\omega_{\text{outer}}(\text{RBM}) = 45\text{cm}^{-1} + \frac{240(\text{nm}\cdot\text{cm}^{-1})}{d_t(\text{nm})} - \frac{30(\text{nm}^2\cdot\text{cm}^{-1})}{(d_t(\text{nm}))^2} \quad (3.3.9b)$$

Where d_t stand for the shell diameter. In the high frequency region, Figure 5 provides the calculated Raman modes (with E_{1g} / A_{1g} / E_{2g} symmetries). When we compare these tangential bands with their band position in the corresponding SWCNT spectra, it can be seen that they are downward shifted (relative to SWCNTs). The animations of the normal modes showed that the strong Raman peaks are mostly resulting from the nuclear motions of the outer-shell.

3.4.1 (n,0)- and (n,n)-boron nitride nanotube

Blase *et al* [98] have theoretically studied the possibility of obtaining boron nitride nanotubes (BNNTs) and initiated an exploration on their characteristic properties [99,100,101], by investigating the connection between hexagonal boron nitride sheets [102] and graphite. Even though a hexagonal boron nitride sheet is made up of alternating atoms of boron and nitrogen, boron nitride surprisingly yields atomic structures like those of graphite. Moreover, the crystallographic parameters of hexagonal boron nitride sheets and graphite are nearly identical. Like CNTs, BNNTs with different chiralities can be formed by rolling up a hexagonal sheet of boron nitride in different chiral directions.

BNNTs have many properties similar to those of CNTs [103,104]. For example, chemical inertness [105], high heat conduction, piezoelectricity [106], exceptional elastic properties [107,108,109,110], high mechanical strength [111,112,113,114], and diameter dependence of the Raman bands [99]. In contrast, whereas CNTs are highly toxic for the human body, and can be semiconductors and conductors depending on their chirality, BNNTs show good biocompatibility and are always semiconducting with a large band gap [99], regardless of their chirality.

The diameter dependence of the vibrational frequency of SWBNNTs has been investigated by many researchers [115]. Sanchez-Portal and Hernandez [116] calculated the dependence of the vibrational properties of the SWBNNTs using TB approximation. By using first principles, Wirtz and Rubio [117] calculated the phonon-dispersion relation for Raman and infrared active modes of (n,0)- and (n,m)-type of the BNNTs. A comparative study of the radial breathing mode was also conducted [118] showed that the frequencies of BNNTs are lower than those of CNTs whose diameter are close to that of BNNTs. Furthermore, the surface buckling that is sole to BNNTs was observed in consequence of the different hybridizations of boron and nitrogen in the bent nanotube surfaces [108,117,119]. Even though numerous theoretical studies have been done on the diameter dependence of the

RBM modes of frequency, a systematic study has not yet been undertaken, although BNNTs has applications in a broad range of fields, such as nanoresonators, nanosensors, actuators and transducers. [120,121,122]. Up to now, SWBNNTs have been especially considered as circular nano-cylinders like SWCNTs. However, Chowdhury *et al*[99] pointed out that this may not be always true as the iconicity of the BN bonds responsible for the surface buckling in hoop direction, could also lead to distortion of the optimized configuration in the axial direction when BNNTs are used with practical end constraints.

The present work aims to achieve a realistic configuration of the optimized SWBNNTs structure, and conduct a detailed study on geometric and spectroscopic properties. These properties include diameter dependence of the Raman and IR spectra of SWBNNTs at same level of the density functional theory (DFT) as used for SWCNTs.

3.4.2 Raman spectra of the (n,0)- and (n,n)-SWBNNTs

We calculated the spectroscopic and geometric parameters of the (n,0)-SWBNNTs with $n = 7$ to 19 and (n,n)-SWBNNTs ($n=3$ to 10) at the same level of the DFT used for the SWCNTs. The assignments to motions of atoms or groups of atoms have been carried out through use of vibration visualization software (GaussView03) that is similar to the assignment made for the (n,0)-SWCNTs as seen in Table 3.3.1, and therefore, are given here. As found for the CNTs, the calculated Raman spectra of the (n,0)- and (n,n)-SWBNNTs in the low frequency region indicated that three of the Raman bands of frequencies are strongly diameter dependent. If the motion of the boron and nitrogen atoms within the nanotube is due to the stretching of the BNNT along its diameter, this result in an elliptical shape abbreviated as ED mode. If it is due to the bending deformation of the BNNT, which results from expansion of the nanotube along diagonal axis, with the motion of two end groups being in opposite directions, this is abbreviated as ED mode. Finally, if the motion of the atoms is in the radial direction in the same phase, this is referred to radial breathing mode, RBM. The calculations exhibited by these Raman bands are also strongly diameter dependent as shown in Figure 3.4.1A-B and Figure 3.4.2A-B for the (n,0)- and (n,n)-SWBNNTs, respectively. The best fit were obtained using a quadratic fitting equation, given by Eq. 3.4.1a-c and Eq. 3.4.2a-c for the (n,0)- and (n,n)-SWBNNTs, respectively. These reproduced the calculated RBMs within $\sim \pm 0.6 \text{ cm}^{-1}$ error ranges, when compared to their corresponding calculated Raman spectra by the DFT technique.

$$\text{RBM}_{(n,0)} = -14.34 + \frac{242.57(\text{nm.cm}^{-1})}{d_t(\text{nm})} - \frac{24.94(\text{nm}^2.\text{cm}^{-1})}{[d_t(\text{nm})]^2} \quad (3.4.1a)$$

$$\text{BD}_{(n,0)} = -0.51 + \frac{214.21(\text{nm.cm}^{-1})}{d_t(\text{nm})} - \frac{38.23(\text{nm}^2.\text{cm}^{-1})}{[d_t(\text{nm})]^2} \quad (3.4.1b)$$

$$\text{ED}_{(n,0)} = -9.81 + \frac{21.41(\text{nm.cm}^{-1})}{d_t(\text{nm})} + \frac{15.55(\text{nm}^2.\text{cm}^{-1})}{[d_t(\text{nm})]^2} \quad (3.4.1c)$$

$$\text{RBM}_{(n,n)} = -27.51 + \frac{270.53(\text{nm.cm}^{-1})}{d_t(\text{nm})} - \frac{75.46(\text{nm}^2.\text{cm}^{-1})}{[d_t(\text{nm})]^2} \quad (3.4.2a)$$

$$\text{BD}_{(n,n)} = 1.09 + \frac{153.87(\text{nm.cm}^{-1})}{d_t(\text{nm})} - \frac{14.25(\text{nm}^2.\text{cm}^{-1})}{[d_t(\text{nm})]^2} \quad (3.4.2b)$$

$$\text{ED}_{(n,n)} = -17.13 + \frac{34.04(\text{nm.cm}^{-1})}{d_t(\text{nm})} + \frac{7.13(\text{nm}^2.\text{cm}^{-1})}{[d_t(\text{nm})]^2} \quad (3.4.2c)$$

Furthermore, as mentioned in Section 3.3.1, the calculated BD band for $(n,0)$ -SWCNTs is not only diameter dependent, but is also dependent on whether the number of hexagons formed in the circumference direction of the SWCNTs $(0,2n)$ type or $(0,2n+1)$ type, respectively are even or odd. However, the calculated ED band for the SWBNNTs did not exhibit dependence on even and odd number of the hexagon in the circumference direction of the $(n,0)$ -SWBNNTs. Moreover, as seen in Figure 3.4.1A-B and 3.4.2A-B, for large sized SWBNNTs, the ω_{RBM} and ω_{BD} mode frequencies converge. The calculated frequency separation between the RBM and BD to found to be 11 cm^{-1} for the $(19,0)$ -SWBNNT and 20 cm^{-1} for the $(10,10)$ -SWBNNTs. It should be noticed that the RBM and BD bands would have unresolvable for the $(n>20,0)$ -SWBNNT, such that found for the $(n,0)$ -SWCNTs.

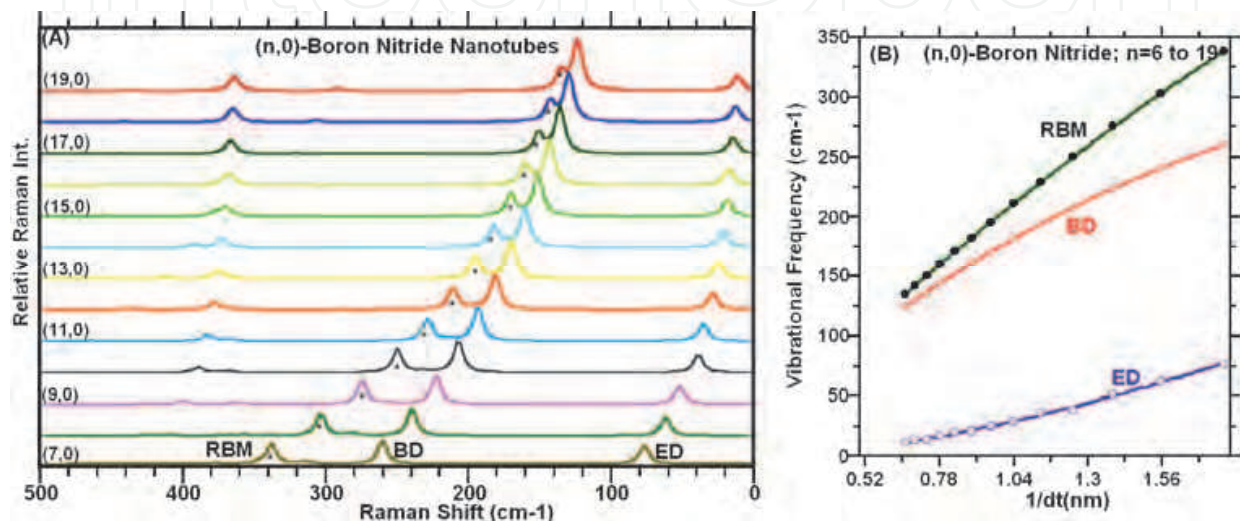


Fig. 3.4.1. Calculated Raman spectra: (A) increased resolution in the low frequency region, showing diameter dependence of the calculated Raman band frequencies for the $(n, 0)$ -SWBNNTs, $n = 7$ to 19 ; (B) the plots of the frequencies of vibrational modes (ED, BD and RBM) versus $1/dt$.

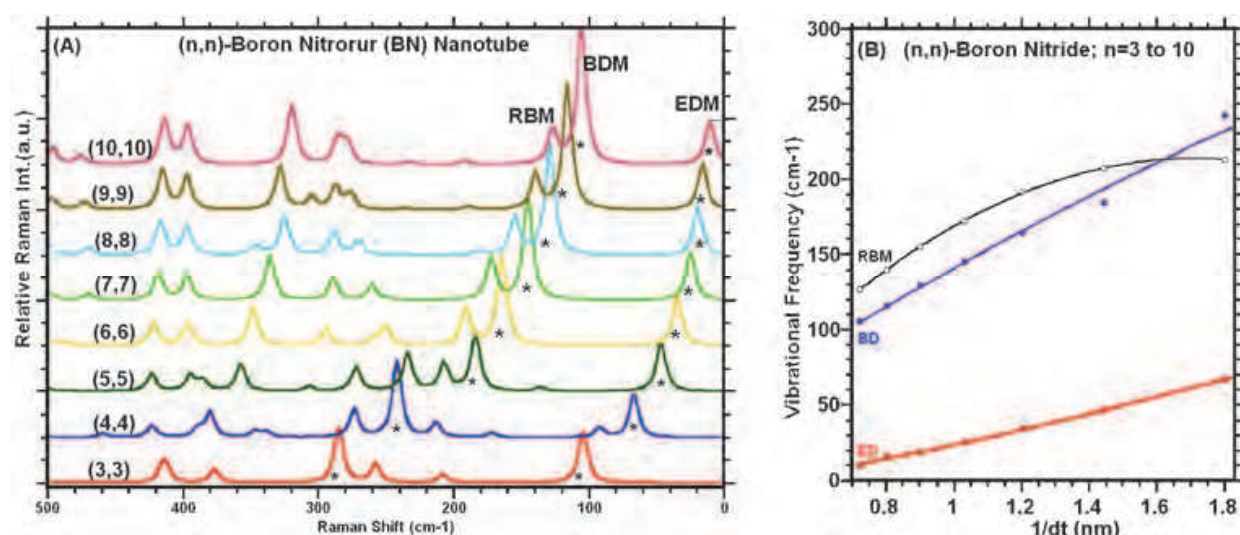


Fig. 3.4.2. Calculated Raman spectra: (A) increased resolution in the low frequency region, showing diameter dependence of the calculated Raman band frequencies for the (n, n) -SWBNNTs, $n = 3$ to 10 ; (B) the plots of the frequencies of vibrational modes (ED, BD and RBM) versus $1/dt$.

We can anticipate, as mentioned earlier for the $(n,0)$ -SWCNTs, in general, that the acquisition of Raman spectra for experimental samples consisting of large diameter SWBNNT with the purpose of characterizing the sample in terms of electronic properties and purity may be complicated by the existence of this BD band, which can lead to apparent broadening of bands as well as the presence of additional bands that may lead to the erroneous conclusion that more than one type of the nanotube is present in the sample.

Also, we have found that calculated Raman bands of the $(n,0)$ - and (n,n) -SWBNNTs in the mid-frequency region (500 - 1000 cm^{-1}) exit almost diameter-independent peak positions. While, as seen in Figure 3.4.3A, in the high-frequency region there are three major Raman bands that are diameter-dependent; two of them lie between 1400 - 1550 cm^{-1} region and another one lie between 1200 - 1300 cm^{-1} region. However, the Raman peaks at about 1200 cm^{-1} remain almost constant. The latter two Raman approach one another with decreasing the tube diameter. For the (n,n) -SWBNNTs, the pattern of the Raman peak in the region of 1000 - 1550 cm^{-1} are similar to these of the $(n,0)$ -SWBNNTs. While the Raman peak at about 1170 cm^{-1} remain almost constant, the other major peaks indicated the dependence on the diameter of the (n,n) -SWBNNTs as shown in Figure 3.4.3B. As discussed earlier, the curvature energy (as given by Eq. 3.1.1) of the nanotube brings about dissimilar force constants along the nanotube axis and the circumference direction. Therefore, the nanotube geometry causes a force constant reduction along the tube axis compared to that in the circumferential direction. As a result, based on the calculations, the curvature effect might play a crucial role in the shift of the peak positions of the G-band as well as the RBM band. Furthermore, It should be noticed that these three major peaks (in the region of ~ 1200 - 1500 cm^{-1}) consist of more than one Raman peak with the different symmetry like A_g and E_g .

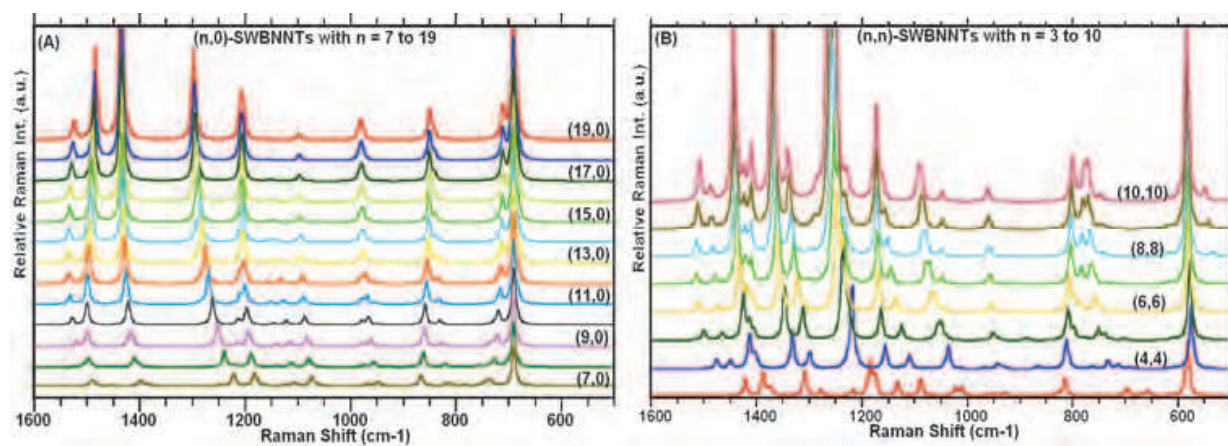


Fig. 3.4.3. Calculated Raman spectra: increased resolution in the high frequency region, showing diameter dependence of the calculated Raman band frequencies: **(A)** for the $(n, 0)$ -SWBNNTs, $n = 7$ to 19 and **(B)** for the (n, n) -SWBNNTs, $n = 3$ to 10 .

Since the atomic motion for each symmetry is in different directions, one (for instance, with symmetry of A_g or E_g) might be enhanced or slightly shifted by a functional group connected to the nanotube by means of covalently bonding or electrostatic interactions. This enhancement or shift in the Raman active peak(s) position might provide some useful information about the structure of functionalized-nanotube, for instance, which of the side of a given functional group covalently bonded or interacts with the nanotube surface or functional group attached to the nanotube along the tube axis or perpendicular to it. This is

important because the absorption of the nanotube in the perpendicular direction is much greater than absorption in the parallel direction; therefore, the availability of photons with polarization parallel to the nanotube axis is greater than that of photons with polarization perpendicular to it. It means that nanotube creates a local electric field aligned along the axis of the nanotube and facilitating the interaction of functional group with the nanotube. Even it may provide charge transfer mechanism for the functionalized-nanotube as the charge transfer from nanotube to molecule as observed between the molecule and nanoparticles by surface enhanced Raman spectroscopy (SERS).[123]

3.5.1 IR spectra of (n,0)- and (n,n)-SWCNTs/SWBNTs

Figures 3.5.1A-B provide calculated IR spectra for the (n,0)- and (n,n)-SWCNTs, respectively, where n ranges from 6 to 19 for the zigzag and from 3 to 12 for the armchair nanotube. As evidenced in Figure 3.5.1A-B, there are two IR active vibrational modes, of A_{2u} and E_{1u} symmetries, whose frequencies are strongly diameter dependent. Least squares fits to the computed frequencies as functions of diameter for the zigzag- and armchair-SWCNTs are shown in Figure 3.5.2A. The fit to the data, for the two bands (of A_{2u} and E_{1u} symmetries) are respectively given by Eqs. 3.5.1a-b for the zigzag- and by the Eqs. 3.5.1c-d for the armchair-SWCNTs. The principal motions these bands correspond to, have been determined by the visualization software mentioned earlier. For the A_{2u} band, the wagging of the SWCNT is along its radial direction, where the motion of the two end groups move in opposite directions. For the E_{1u} band, the principal motion involves wagging of the SWCNT along its circumference direction. Our short hand notation for these two principal vibrations are the subscripts shown on the frequencies, where RW and CW, respectively, specify radial and circumference wagging.

$$\omega_{RW}(A_{2u}; (n, 0)) = -1.85 + \frac{209.38(\text{nm}\cdot\text{cm}^{-1})}{d_t(\text{nm})} - \frac{3.71(\text{nm}^2\cdot\text{cm}^{-1})}{[d_t(\text{nm})]^2} \quad (3.5.1a)$$

$$\omega_{CW}(E_{1u}; (n, 0)) = 7.33 + \frac{322.62(\text{nm}\cdot\text{cm}^{-1})}{d_t(\text{nm})} - \frac{8.46(\text{nm}^2\cdot\text{cm}^{-1})}{[d_t(\text{nm})]^2} \quad (3.5.1b)$$

$$\omega_{RW}(A_{2u}; (n, n)) = 265.42 + \frac{9.48(\text{nm}\cdot\text{cm}^{-1})}{d_t(\text{nm})} + \frac{35.46(\text{nm}^2\cdot\text{cm}^{-1})}{[d_t(\text{nm})]^2} \quad (3.5.1c)$$

$$\omega_{CW}(E_{1u}; (n, n)) = 367.66 + \frac{39.55(\text{nm}\cdot\text{cm}^{-1})}{d_t(\text{nm})} + \frac{5.51(\text{nm}^2\cdot\text{cm}^{-1})}{[d_t(\text{nm})]^2} \quad (3.5.1d)$$

It is to be noted (for completeness sake), that in the high frequency vibrational region of Figure 3.5.1A-B, as revealed upon close inspection, there are three IR vibrational mode of frequencies $\sim 1520 \text{ cm}^{-1}$ (E_{1u} symmetry), $\sim 1365 \text{ cm}^{-1}$ (E_{1u}) and $\sim 1332 \text{ cm}^{-1}$ (A_{2u}) whose positions show weak dependence on diameter; additionally, in the mid frequency region, there is one IR-mode of frequency $\sim 780 \text{ cm}^{-1}$ (A_{2u}) that is also weakly diameter dependent. Hence, the strong diameter dependence of the two low frequency bands may be useful for determining structural indices of SWCNT samples. A more detailed description of the assignments for bands in the IR spectra for the various (n,0)-SWCNTs is contained in Table 3.5.1.

Figure 3.5.3A-B provide the calculated IR spectra of the zigzag-(n,0) and armchair-(n,n) single-wall boron nitride nanotube (SWBNNTs) exhibits similar band structure to their corresponding SWCNTs with the same chiral index (n,0) and (n,n), when comparing the

calculated IR spectra of the (n,0)- and (n,n)-SWBNNTs with the (n,0)- and (n,n)-SWCNTs (see Figure 3.5.1A-B). Least squares fits to the computed frequencies as functions of diameter for the zigzag- and armchair-SWBNNTs are shown in Figure 3.5.2B. The fits to the data, for the two bands (ω_{RW} and ω_{CW}) are respectively given in Eqs. 3.5.2a-b for the (n,0)- and given in the Eqs. 3.5.2c-d for the (n,n)-SWBNNTs.

$$\omega_{RW}(A_{2u}; (n, 0)) = -12.40 + \frac{239.27(\text{nm.cm}^{-1})}{d_t(\text{nm})} - \frac{23.64(\text{nm}^2.\text{cm}^{-1})}{[d_t(\text{nm})]^2} \quad (3.4.2a)$$

$$\omega_{CW}(E_{1u}; (n, 0)) = -38.67 + \frac{397.76(\text{nm.cm}^{-1})}{d_t(\text{nm})} - \frac{81.00(\text{nm}^2.\text{cm}^{-1})}{[d_t(\text{nm})]^2} \quad (3.4.2b)$$

$$\omega_{RW}(A_{2u}; (n, n)) = 104.50 + \frac{167.86(\text{nm.cm}^{-1})}{d_t(\text{nm})} - \frac{12.14(\text{nm}^2.\text{cm}^{-1})}{[d_t(\text{nm})]^2} \quad (3.4.2c)$$

$$\omega_{CW}(E_{1u}; (n, n)) = 298.17 - \frac{48.00(\text{nm.cm}^{-1})}{d_t(\text{nm})} + \frac{62.56(\text{nm}^2.\text{cm}^{-1})}{[d_t(\text{nm})]^2} \quad (3.4.2d)$$

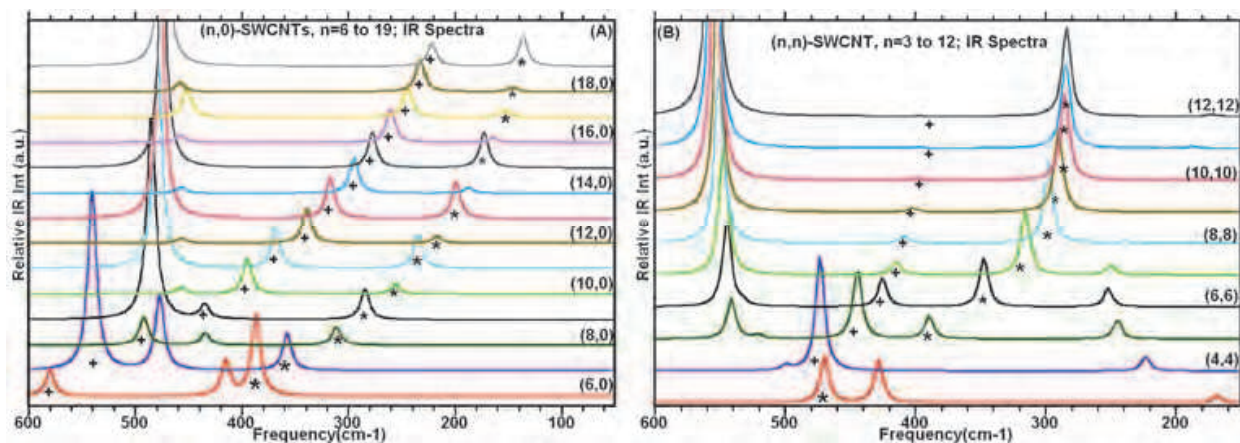


Fig. 3.5.1 Calculated IR spectra (A) for the (n,0)-SWCNTs, with n varying from 0 to 19; (B) for the (n,n)-SWCNTs with n = 3 to 12. Where signs * and + stand for the IR active modes of frequencies; $\omega_{RW}(A_{2u})$ and $\omega_{RW}(A_{2u})$, respectively.

Furthermore, for DWCNTs (not shown here), the calculated IR bands with A_{2u} symmetries at 387 and 216 cm^{-1} for (0,6)- and (0,12)-SWCNTs are blue-shifted to 395 and 253 cm^{-1} in IR spectrum of (0,6)&(0,12)-DWCNTs, respectively. The IR bands with A_{2u} symmetries at 358 and 187 cm^{-1} in spectra of (0,7)- and (0,14)-SWCNTs correspond to the bands at 411 and 247 cm^{-1} in spectrum of (0,7)&(0,14)-DWCNT. Furthermore, the IR bands with E_{1u} symmetries at 580 and 339 cm^{-1} for (0,6)- and (0,12)-SWCNTs are also blue-shifted to 617 and 350 cm^{-1} in the spectrum of (0,6)&(0,12)-DWCNT, respectively. The bands (with E_{1u} symmetries) at 541 and 295 cm^{-1} in spectra of (0,7)- and (0,14)-SWCNTs correspond to the bands at 567 and 300 cm^{-1} in the spectrum of (0,7)&(0,14)-DWCNT, respectively.

3.6.1 Calculated vertical transitions of the SWCNTs and SWBNNTs

As mentioned earlier in Section 2, the chiral index (n,m) of the nanotube indicates whether the tube is metallic or semiconducting. When the $(n-m) = 3q$ ($q = 0, 1, 2, 3 \dots$), all the tubes are metallic, if not, semiconducting. Therefore, all armchair tubes are metallic. The calculated density of states (DOS) of the nanotube using tight binding approximation (TBA)

does not comprise one smooth band, but shows a number of side-bands with spikes around the Fermi level separated from each other [92,124], which are called the van Hove singularities. The side-bands represent 1D channel for conduction along the nanotube. The side-bands and their sharp onsets have been observed in their tunneling DOS obtained from scanning tunneling spectroscopic measurements [125].

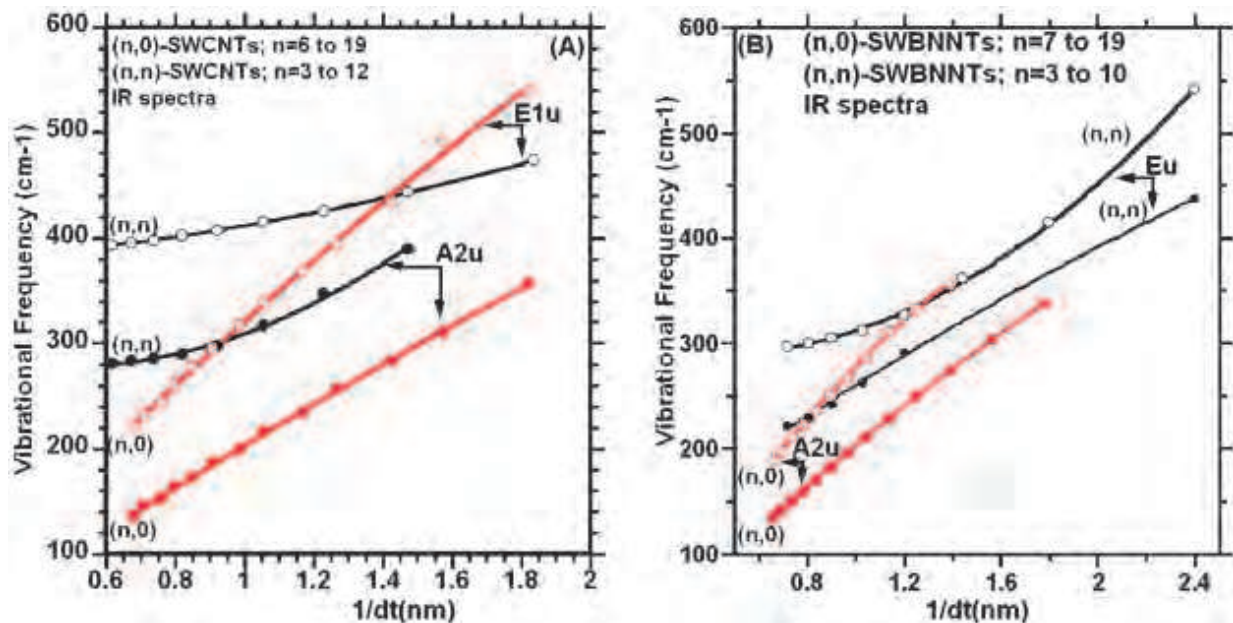


Fig. 3.5.2 The plots of the dependence of calculated IR frequencies, in the low frequency region, as a function of nanotube diameter for vibrational modes of symmetries A_{2u} and E_{1u}; (A) for the SWCNTs and (B) for the SWBNNTs.

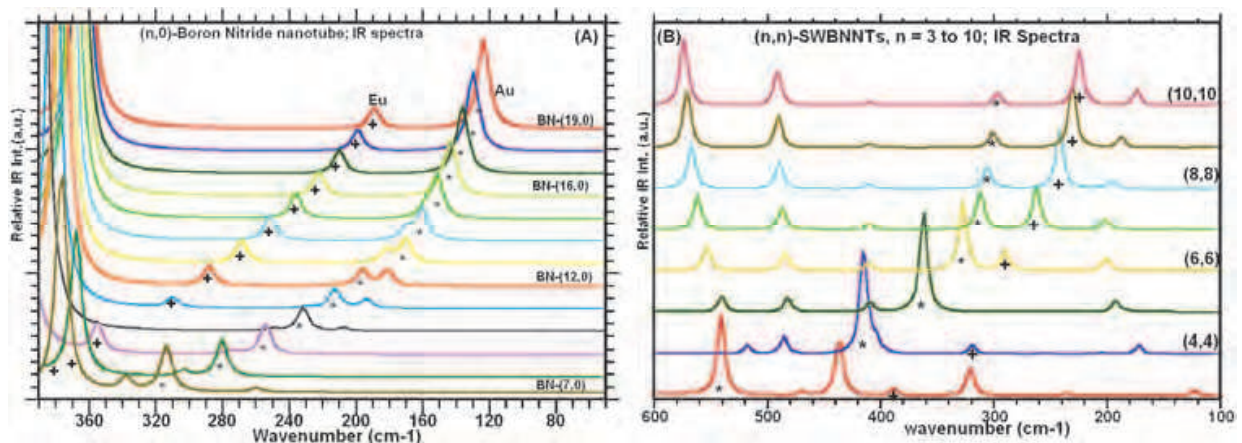


Fig. 3.5.3 (A) Calculated IR spectra of the (n,0)-SWNTs, with n varying from 7 to 19; (B) illustrate for the (n,n)-SWBNNTs with n = 3 to 10.

For larger-diameter tubes, the singularities move close together and combine, thus making the DOS similar to that of a graphene layer. In contrast, for smaller-diameter nanotubes, the singularities are well separated specially near the Fermi level and can give initial and final states for a resonance Raman scattering (RRS) process. In a simplified representation, neglecting all the curvature effects and considering the linear dispersion of π and π^* bands

of graphene only, the energy gap between q^{th} van Hove singularity in valence and conduction bands for metallic tubes[126] is $E_{qq}^M = \frac{6q\gamma_{acc}}{d_t} = 3E_{qq}^S$ ($q = 1, 2, 3, \dots$) and $E_{qq}^S = \frac{2q\gamma_{acc}}{d_t}$ for semiconducting tubes as discussed in Section 2. In the case of metallic tubes, the linear crossing of π and π^* bands near the Fermi level yields a small constant DOS leading to sharp van Hove singularities at energies away from the Fermi energy. In contrast, for semiconducting tubes, the DOS at Fermi energy is zero with sharp van Hove singularities away from the Fermi energy [92,127].

The electronic structures of the SWBNNTs were theoretically investigated by Rubio *et al.* [56] using the tight binding approximation (TBA). All SWBNNTs were found to be semiconducting materials with band gaps larger than 2 eV. BNNTs with larger diameters have a larger band gap, with a saturation value corresponding to the band gap of a hexagonal boron nitride (BN) as calculated by Rubio *et al.*[56] or see the Figure 4 in Ref.[57]. The subsequent studies based on local-density-functional (LDA) calculations proved that it is energetically more favorable to fold a hexagonal boron nitride sheet into a BNNT than to form a CNT from a graphite sheet [58]. This observation is also supported by our calculations at B3LYP/6-31G level of DFT as discussed in Section 3. Based on the band-folding analysis, SWBNNTs are semiconductors with large-gap for the zigzag- and armchair-SWBNNTs. This is due to the strong hybridization effects may take place because tube curving reduces the BNNT's band gap remarkably. For the $(n, 0)$ BNNTs, with $n > 12$ the hybrid state was found not to play any role in determining tube gaps. The gaps are steady at around 4 eV as indicated by LDA. In another calculation using density functional theory, the band gaps of BNNTs were eventually saturated at 5.03 eV with an increase in diameter [128,129,130,131,132]. Based our calculated dipole allowed vertical electronic transitions, for the $(n, 0)$ -BNNTs with $n > 11$, the gaps are steady around 5.9 eV, see Figure 3.6.1B and Table 3.6.4. For the (n,n) -SWBNNTs, with $n > 10$, the band gaps slightly increases with increasing tube diameter and seem to be steady at around 5.84 eV according to our DFT calculations as seen Figure 3.6.1B and Table 3.6.4. It should be noted that there are many forbidden electronic transition lie below the allowed one. Based on our experience on the calculated electronic transitions for many organic compounds at B3LYP level and at the BLYP level of DFT for the transition metals [95], the calculated value of the electronic transitions are somewhat higher than their experimental values, as much as 0.4 eV. Therefore, the calculated values of the electronic band gaps for the nanotubes might be reasonable.

Various methods have been developed to tune the electronic structure of BNNTs is nicely discussed by Chunyi Zhi *et al.*[57], for instance, applying electric field [133,134,135,136,137,138] or strain [139], or chemical methods, like doping [140,141,142,67], introducing defects [143,144,145] or surface modification [60,146,147]. The methods and species chosen are summarized in Table 2 in Ref. 57. Physical methods could directly reduce the band gap of BNNTs, while chemical methods were found to tune the band gap by introducing localized energy levels inside the gap [57]. For example, by applying an 2 V/nm electric field, the band gap of a $(12, 12)$ BNNT was directly reduced from 4.5 eV to about 2.5 eV [135], while F-doping induced an unoccupied localized state in the gap of BNNTs [148]. In addition, chemical modification methods of BNNTs were sometimes found to enrich the properties of BNNTs, for instance, polarization field was induced by chemical adsorption [149] or ferromagnetism appeared in doped BNNTs.

For electronic structure of multi-walled BNNTs (MWBNTs), it has been reported that there is hybridization between p and s states of inner and outer tubes [150,151]. This effect leads to the top valence and bottom conduction bands localization on the outer and inner tubes, respectively [57]. The band gap of DWBNNTs is slightly narrower than that of the inner tubes. This is because the downward shifts of the p states of the inner tube are larger than those of the outer tube. Furthermore, in the interwall region the peculiar charge redistribution is induced by the near-free-electron states of BNNTs [57,152]. The fluorine doping can significantly modify the DWBNNTs' inter-wall interactions and thus both tube walls turn into effective conducting channels. This leads to a remarkably improved electrical transport in them [151].

There are strong interactions between electrons and holes in BNNTs [54,55]. The excitonic effects were indeed shown to be more important in BNNTs than in CNTs. Bright and dark excitons in BNNTs alter the optical response qualitatively. For example, the absorption spectrum of the (8, 0) BNNT is dominated by a peak at 5.72 eV, due to an exciton with a binding energy of 2.3 eV. The binding energy for the first excitonic peak is more than 3 eV for the (2, 2) nanotube, which will fast converge to around 2.1 eV of the hexagonal single BN sheet as a result of strongly localized nature of this exciton [57], which is consistent with the results by the Louie's group [54]: a 2.3 eV binding energy for a (8, 0) BNNT.

In this section, we provided the calculated vertical electronic transitions of the (n,0)- and (n,n)-type nanotubes using time-dependent DFT methods at the TD-B3LYP/6-31G level. Table 3.6.1 and Table 3.6.2 provide the calculated electronic transitions from (7,0) to (11,0) and (14,0) and from (3,3) to (10,10) for the SWCNTs, respectively. The transitions from the (7,0) to (14,0) and from (3,3) to (10,10) for the zigzag- and armchair-SWBNNTs are given in Table 3.6.3 and Table 3.6.4, respectively.

The diameter dependence of the calculated dipole allowed electronic transitions are shown in Figure 3.6.1A-B. As seen in Figure 3.6.1A, the allowed electronic transitions lie in the range from 0.5 eV to 3.0 eV for the (n,0)-SWCNTs, with $n = 7$ to 14, and lie in the range from 2.8 eV to 4.4 eV for the (n,n)-SWCNTs, with $n=3$ to 10. Furthermore, the plot of the calculated dipole allowed electronic transitions showed that while the allowed transitions rapidly decrease and stabilize (around 0.5 eV) with increasing the diameter of the (n,0)-SWCNTs, for the armchair SWCNTs, the electronic transitions are diameter dependent, but also these transitions converge and become constant (around 3 eV) with increasing tube diameters of the (n,n)-SWCNTs. For the SWBNNTs, the result of the calculations indicated that the dipole allowed electronic transitions are not only diameter dependent, but also the electronic transitions lie in the range from 5.7 eV to 6.6 eV as seen in Figure 6.3.1B, which is higher than the calculated electronic transitions for the SWCNTs. This large band gap in SWBNNTs relative to SWCNTs is not so surprising since the B-N bond contains a significant ionic component. This polarity can extremely alter both molecular and solid-state electronics as well as optical properties of the system by modifying the character of the frontier molecular orbitals [57]. Furthermore, the calculated band gap of BNNTs between 5.7 and 6.6 eV is independent to tube chirality. This provides good electrical insulation, in spite of the fact that CNTs can be a metal or a narrow band-gap semiconductor. This discrepancy in electronic structure results in different luminescence emission: SWBNNTs have violet or ultraviolet luminescence under excitation by electrons or photons, while SWCNTs can emit infrared light and the wavelengths depend on their chiralities.

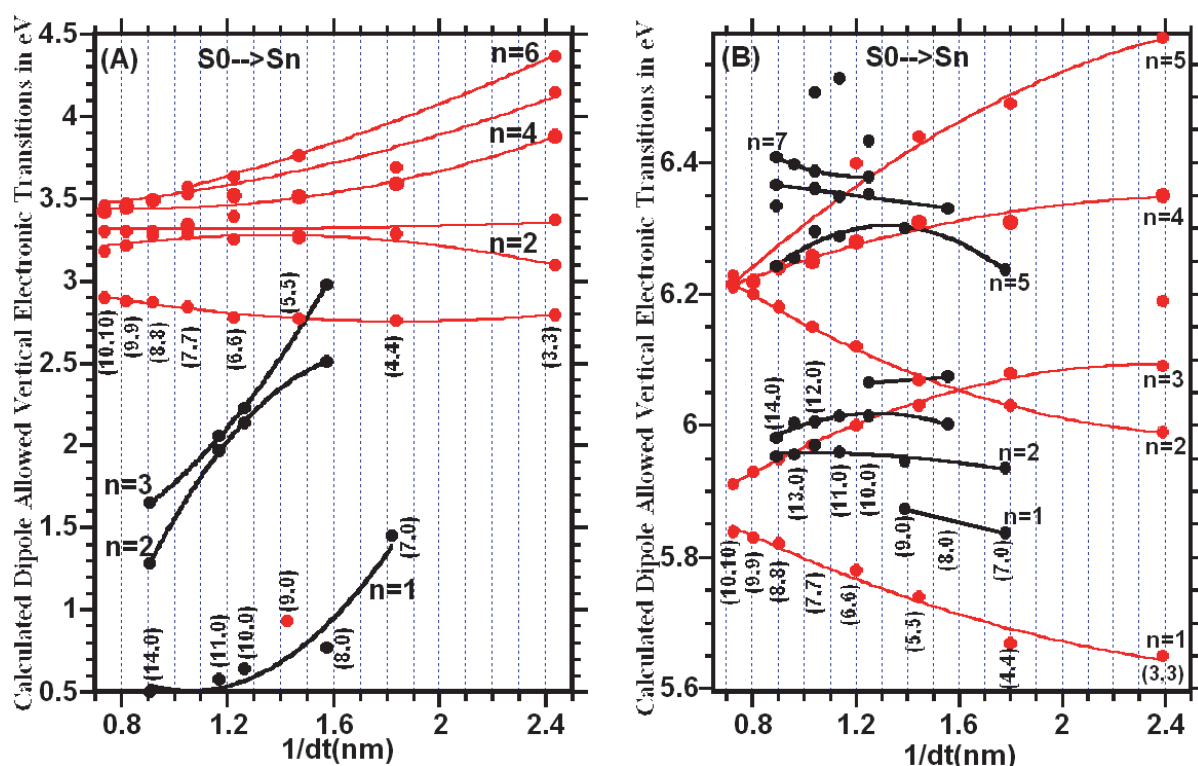


Fig. 3.6.1. Diameter dependence of calculated dipole allowed vertical electronic transitions of: a) SWCNTs and b) SWBNNTs at B3LYP/6-31G level of DFT.

	(7,0)		(8,0)		(9,0)		(10,0)		(11,0)		(14,0)	
m	TB	DFT	f	TB	DFT	f	TB	DFT	f	TB	DFT	f
1	0.91	1.04	0.77	0.02	0.56	1.10	0.64	0.01	0.36	0.758	0.50	0.0042
2	1.25		1.46		0.80	1.09		0.51		0.63		
3	1.25		1.46		0.80	1.09		0.52		0.63		
4	1.42	1.45	0.06	2.44	0.93	0.04	1.77	0.98	0.58	0.02	0.89	
5	2.52	2.40	2.51	0.36	2.32	2.04	1.80	1.10				
6	2.53	2.51	0.36	2.32	2.04	1.80	1.10					
7	2.93	2.53	2.50	2.20	2.14	0.50	1.78	1.97	0.50	1.29	0.0872	
8	2.93	2.00	2.50	2.14	0.50	1.97	0.50	1.436	1.65	0.7917		
9	3.02	2.78	2.64	2.23	0.12	2.06	0.12	1.65	0.7925			
10	3.02	2.78	2.64	2.53	2.06	1.95						
11	3.08	2.77	2.72	2.75	2.14	1.96						
12	3.08	2.98	0.13	2.72	2.14	2.20						
dt	0.56	0.64	0.71	0.79	0.87	1.10						

Table 3.6.1. DFT-calculated vertical singlet-singlet transitions ($S_0 \rightarrow S_m$ in eV) of the (n,0)-SWCNTs, $n = 7$ to 11, at the B3LYP/6-31G level. Oscillator strengths (f) and results of the calculated energy from the tight-binding (TB) approximation for each nanotube are provided for comparison. The value of γ was taken to be 2.7 eV in the TB calculations. The d_t stands for diameter in nm.

m	(3,3)		(4,4)		(5,5)		(6,6)		(7,7)		(8,8)		(9,9)		(10,10)	
	DFT	f	DFT	f												
1	1.35		1.84		2.15		2.36		2.58		2.69		2.77		2.83	
2	2.40		2.76	0.0033	2.77	0.0072	2.78	0.0106	2.84	0.0108	2.87	0.0132	2.88	0.0153	2.90	0.0173
3	2.40		2.77		2.89		2.93		2.99		2.99		2.98		2.98	
4	2.79	0.0003	2.77		2.90		2.93		2.99		2.99		2.98		2.98	
5	3.08		3.22		3.26	0.1197	3.25	0.1118	3.25		3.18		3.14		3.11	
6	3.08		3.22		3.26		3.29		3.29	0.1042	3.28	0.0036	3.22	0.0081	3.18	0.0197
7	3.10	0.0082	3.25		3.27		3.29		3.34	0.0012	3.28	0.0036	3.22	0.0081	3.18	0.0197
8	3.10	0.0082	3.25		3.28	0.0007	3.29		3.34	0.0012	3.30	0.0963	3.25		3.20	
9	3.37	0.1209	3.29	0.1281	3.29		3.29		3.34		3.30		3.25		3.20	
10	3.82		3.59	0.0040	3.50		3.34		3.34		3.30		3.30	0.0878	3.30	0.0779
11	3.88	0.0001	3.59	0.0040	3.51	0.0001	3.39	0.0002	3.35		3.35		3.35		3.34	
12	3.88	0.0001	3.69	0.0003	3.51	0.0005	3.39	0.0002	3.35		3.35		3.35		3.34	
13	3.94		3.69	0.0003	3.58		3.52	0.0017	3.53	0.0099	3.49	0.0294	3.45	0.0328	3.39	
14	3.95		3.76		3.58		3.52	0.0017	3.53	0.0099	3.49	0.0294	3.45	0.0328	3.39	
15	3.95		3.85		3.74		3.63		3.57	0.0132	3.51		3.45		3.42	0.0359
16	3.99		3.96	0.0954	3.76	0.0606	3.63	0.0450	3.57	0.0132	3.51		3.45		3.42	0.0359
17	3.99		3.96	0.0954	3.77	0.0658	3.63	0.0450	3.58		3.51		3.45		3.42	
18	4.15	0.1277	3.99		3.82		3.68		3.64		3.54		3.47	0.0164	3.46	0.1043
19	4.15	0.1275	3.99		3.82		3.68		3.64		3.54		3.47	0.0165	3.46	0.1043
20	4.37	0.0009	3.99		3.85		3.72		3.66		3.58		3.53		3.48	
dt	0.41		0.55		0.68		0.81		0.95		1.09		1.22		1.36	

Table 3.6.2. DFT-calculated vertical singlet-singlet transitions ($S_0 \rightarrow S_m$ in eV) and oscillator strengths (f) of the (n,n)-SWCNTs, $n = 3-10$, at the B3LYP/6-31G level. The d_t stands for diameter in nm.

Moreover, the properties of triplet states in the nanotubes may play a circular role in the number of fundamental physics phenomena such as singlet-triplet splitting in low-dimensional materials is a degree of electronic correlation strength and exchange effects [153], like that of exciton binding energy. Also, how relaxation of photo-excitations takes place in CNTs is not well known as a result of being weakly-emissive materials [154,155], this properties are called as the 'dark' singlet excitons below the optically allowed states [156].

The calculated singlet-triplet electronic energy levels of the (7,0)-SWCNT is given in Figure 3.6.2A. As seen in the figure, for the (7,0)-SWCNT, while the calculations exhibited only one dipole allowed electronic transition ($S_0 \rightarrow S_4$) below about 3 eV; however, there are many forbidden or very weak electronic transitions (oscillator strength less than 0.0001) in this energy region. The distance between these electronic transitions are ~ 0.47 eV between S_1 and S_4 electronic energy levels and ~ 0.15 eV between S_2 ($\sim S_3$) and S_4 states. The calculations indicated similar situations for the (8,0)-SWCNT. The distance between the energy levels of the first excited singlet state (S_1) and second triplet state (T_2) is about 0.05 eV. As consequence, these results may imply that there would be an intersystem crossing (IC) from S_4 to S_2 and

S_1 electronic energy levels, followed by an intersystem crossing (ISC) process to the second the lowest triplet energy level (T_2). This process may lead to quenching the fluorescence by nonradiative decay.

m	(3,3)		(4,4)		(5,5)		(6,6)		(7,7)		(8,8)		(9,9)		(10,10)	
	DFT	f														
1	5.28		5.45		5.61		5.71		5.75		5.76		5.77		5.76	
2	5.50		5.67	0.0107	5.74	0.0029	5.78	0.0005	5.80		5.82	0.0001	5.83	0.0003	5.84	0.0006
3	5.50		5.68		5.79		5.84		5.86		5.87		5.87		5.87	
4	5.65	0.0174	5.68		5.79		5.84		5.86		5.87		5.87		5.87	
5	5.99	0.0127	5.94		5.94		5.93		5.94		5.95	0.5283	5.93	0.7425	5.91	0.9893
6	5.99	0.0127	5.94		5.99		6.00	0.2125	5.97	0.3482	5.95	0.5284	5.93	0.7424	5.91	0.9893
7	6.09	0.0802	6.00		5.99		6.00	0.2125	5.97	0.3512	5.97		5.99		5.97	
8	6.12		6.03	0.1050	6.03	0.1173	6.01		6.01		6.00		5.99		5.97	
9	6.12		6.08	0.0532	6.03	0.1171	6.01		6.01		6.00		6.00		6.00	
10	6.13		6.08	0.0532	6.07	0.1338	6.12	0.1620	6.08		6.05		6.02		6.00	
11	6.19	0.0418	6.13		6.14		6.12		6.08		6.05		6.02		6.02	
12	6.19	0.0418	6.13		6.14		6.12		6.15	0.1907	6.18	0.2230	6.14		6.10	
13	6.35	0.0421	6.30		6.17		6.16		6.18		6.18		6.14		6.10	
14	6.35	0.0421	6.30		6.17		6.16		6.18		6.20		6.15		6.12	
15	6.37		6.31	0.1307	6.31	0.2425	6.28	0.4262	6.24		6.20		6.15		6.12	
16	6.37		6.31	0.1307	6.31	0.2423	6.28	0.4262	6.24		6.20		6.20	0.2572	6.21	1.3747
17	6.39		6.39		6.35		6.33		6.24		6.20		6.22		6.21	1.3750
18	6.53		6.45		6.42		6.40	0.2929	6.25	0.6546	6.24	0.8986	6.22		6.21	0.2906
19	6.59	0.0100	6.49	0.1349	6.44	0.2154	6.40	0.2928	6.26	0.6538	6.24	0.8979	6.22	1.1396	6.23	
20	6.59	0.0100	6.49	0.1349	6.44	0.2173	6.41		6.32		6.31		6.22	1.1396	6.23	0.0005
d_t	0.42		0.56		0.69		0.83		0.97		1.11		1.25		1.38	

Table 3.6.3. DFT-calculated vertical singlet-singlet transitions ($S_0 \rightarrow S_m$ in eV) and oscillator strengths (f) of the (n,n)-SWBNNTs, $n = 3-10$, at the B3LYP/6-31G level. The d_t stands for the diameter in nm.

For the (8,0)-SWCNT, the calculations indicated that there are two dipole allowed electronic transitions below 3 eV. Dipole allowed second electronic state (S_2) lies about 0.03 eV above the second triplet excited state (T_2), see Figure 3.6.2A. If an ISC process between the S_2 and T_2 electronic states take place, then, there would be a $T_2 \rightarrow T_1$ transition followed by a triplet-singlet electronic transition $T_1 \rightarrow S_0$, see Appendix in Section 4 for detailed discussions for the singlet-triplet transitions. As a consequence, as mentioned in Ref. 153 that the triplet states play any crucial role for the nonradiative decay of photo-excitations and this property is called the “dark” singlet excitons below the optically allowed states [153,156].

Similarly, the calculated vertical transitions for the (8,0)- and (4,4)-SWBNNTs, up to ~6 eV, indicated that there are many forbidden or very weak electronic transitions (oscillator strength (f) less than 0.0001) that lie below the first dipole allowed singlet-singlet electronic transition. The first dipole allowed singlet-singlet electronic transition has almost the same energy with the spin forbidden singlet-triplet electronic transitions in addition to many dipole forbidden singlet-singlet transitions below the first dipole allowed electronic transitions as seen in Figure 3.6.2B. Thus, these calculated findings may suggest that there

would be a IC and/or ISC processes for the (4,4)- and (8,0)-SWBNNTs, which might lead to a nonradiative decay.

m	(7,0)		(8,0)		(9,0)		(10,0)		(11,0)		(12,0)		(13,0)		(14,0)	
	DFT	f														
1	5.05		5.61		5.77		5.87		5.82		5.83		5.84		5.82	
2	5.05		5.61		5.86		6.01		5.92		5.95		5.95		5.92	
3	5.67		5.69		5.86		6.01		5.92		5.95		5.95		5.92	
4	5.67		5.80		5.87	0.0215	6.01	0.0481	5.95	0.1456	5.97	0.0871	5.96	0.1029	5.95	0.1456
5	5.68		5.87		5.87	0.0215	6.01	0.0481	5.95	0.1456	5.97	0.0871	5.96	0.1029	5.95	0.1456
6	5.68		6.00	0.0255	5.95	0.0135	6.07	0.0251	5.98	0.0233	6.01	0.0239	6.00	0.0186	5.98	0.0233
7	5.73		6.00	0.0255	6.06		6.24		6.07		6.19		6.11		6.07	
8	5.84	0.0095	6.02		6.06		6.24		6.07		6.19		6.11		6.07	
9	5.84	0.0094	6.02		6.06		6.34		6.24	1.4646	6.30	0.8777	6.26	0.0094	6.24	1.4646
10	5.87		6.04		6.06		6.34		6.24	1.4646	6.30	0.8777	6.26	0.0094	6.24	1.4646
11	5.87		6.07	0.0164	6.09		6.35		6.33	0.0700	6.36	0.0256	6.26	1.3216	6.33	0.0700
12	5.90		6.11		6.09		6.35		6.33	0.0700	6.39	0.0168	6.26	1.3217	6.33	0.0700
13	5.90		6.11		6.16		6.35	0.4783	6.37	0.0226	6.39	0.0168	6.36		6.37	0.0226
14	5.93	0.0180	6.14		6.16		6.35	0.4784	6.40		6.43		6.37		6.40	
15	6.04		6.14		6.28		6.38	0.0317	6.40		6.51	0.5031	6.37		6.40	
16	6.04		6.16		6.28		6.43		6.41	0.2283	6.51	0.5031	6.40	0.0557	6.41	0.2283
17	6.09		6.16		6.30	0.0918	6.43	0.1102	6.41	0.2283	6.52		6.45		6.41	0.2283
18	6.09		6.17		6.30	0.0918	6.43	0.1102	6.43		6.52		6.45		6.43	
19	6.24	0.1460	6.18		6.35		6.50		6.48		6.59	0.0012	6.50		6.48	
20	6.24	0.1468	6.33	0.2616	6.35		6.62		6.48		6.59	0.0012	6.60		6.48	
d_t	0.56		0.64		0.72		0.80		0.88		0.96		1.04		1.12	

Table 3.6.4. DFT-calculated vertical singlet–singlet transitions ($S_0 \rightarrow S_m$ in eV) and oscillator strengths (f) of the (n,0)-SWBNNTs, n = 7–14, at the B3LYP/6-31G level. The d_t stands for the diameter in nm.

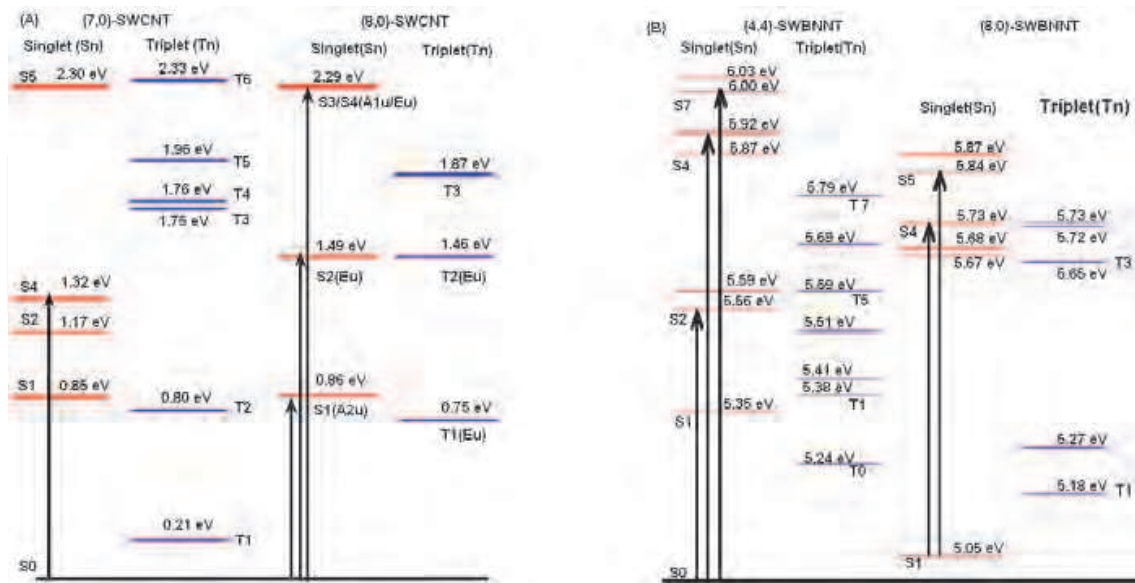


Fig. 3.6.2. Calculated singlet and triplet vertical electronic transitions: (A) for the (7,0)- and (8,0)-SWCNT and (B) for the (4,4)- and (8,0)-SWBNNTs at TD-B3LYP/6-31G(d,p) level of DFT. The vertical solid lines indicate dipole allowed vertical electronic transitions.

3.7 Functionalization of single-wall carbon nanotubes

Single-walled carbon nanotubes (SWNTs) demonstrate useful properties for different prospective applications counting miniature biological devices, such as used as electrodes for detecting biomolecules in solutions. Furthermore, the electrical properties of SWNTs are sensitive to surface charge transfer and changes in the surrounding electrostatic environment, undergo severe changes by adsorptions of desired molecules or polymers [157,158]. SWNTs are subsequently promising for chemical sensors for detecting molecules in the gas phase and biosensors for probing biological processes in solutions. Nevertheless, significant effort is necessary to realize interactions between nanotubes and organic molecules or biomolecules and how to impart explicitness and selectivity to nanotube-based bioelectronic devices [159].

Functionalized carbon nanotube with inorganic and biological macromolecules like deoxyribonucleic acid (DNA) makes possible the formation of hybrid materials with interesting properties. Biological functionalization, particularly deoxyribonucleic acid (DNA) functionalization has attracted much scientific attention because of the possible development of sensitive and ultrafast detection systems for molecular electronics. As a result of the existence of a large number of delocalized π -electrons on its bases, DNA can be used as molecular wire [160]. Furthermore, the functionalization of CNTs with DNA molecules magnifies the CNT solubility in organic media and promotes application and development in DNA based nanobiotechnology. Also, the functionalization character of CNTs with DNA molecules may be used to distinguish metallic CNT from semiconducting CNTs. DNA chains have various functional structural groups available for covalent interaction with CNTs for construction of DNA-based devices through the sequence-specific pairing interactions. Functionalized carbon nanotubes (CNT) are proficient for biomedical applications [161,162]. They can be used for biosensing [163] or act as nano-heaters [164], temperature sensors [165] and drug-carrier systems for therapy and diagnosis at the cellular level [166]. Functionalization of the outer surface of CNT with biomolecules such as nucleic acids, proteins, peptides and polymers makes possible their definite internalization into the cell [167,168,169]. On the other hand, the acceptable uptake mechanism remains a contentious problem since it may depend on cell type, bio-functionalized scheme, size of the nanotube and other factors [170,171,172,173].

Müller et al.[174] have reported that the Raman signal of functionalized carbon nanotube, specially the intensity of the radial breathing mode, suffer from its chemical functionalization. They concluded that chemical reaction appears to be diameter selective under certain reaction conditions, possibly accompanied by an effect related to the tube species. Sayes *et al.*[175] used Raman spectroscopy and thermogravimetric analysis to analysis the phenylated-SWNTs (SWNT-phenyl-SO₃H and SWNT-phenyl-SO₃Na). They have reported that Raman spectroscopy provide a direct evidence of covalent sidewall functionalization. They mentioned that Raman spectrum of the starting purified SWNTs shows a small disorder mode (D-band) at 1290 cm⁻¹ (in Fig. 2A of Ref.[175]). The spectra of the least, medium and most functionalized samples exhibit progressively increasing disorder modes relative to the large tangential modes (G-band) at ~1590 cm⁻¹.

In this section, we provided the calculated the calculated Raman and IR spectra of functionalized (7,0)-SWCNT, using the B3LYP functional with the basis sets 6-31G on carbon and hydrogen atoms and 6-311G(d,p) basis set used for oxygen and nitrogen atoms. All functional groups used here (-phenyl-SO₃H, carboxy (-CO₂H), and 3-methoxy-6-methyl-4-[(2-nitro-4-methylphenyl) azo] benzene) are covalently bonded to the (7,0)-SWCNT. The calculated Raman spectrum of the functionalized carbon nanotube is given in Figure 3.7.1,

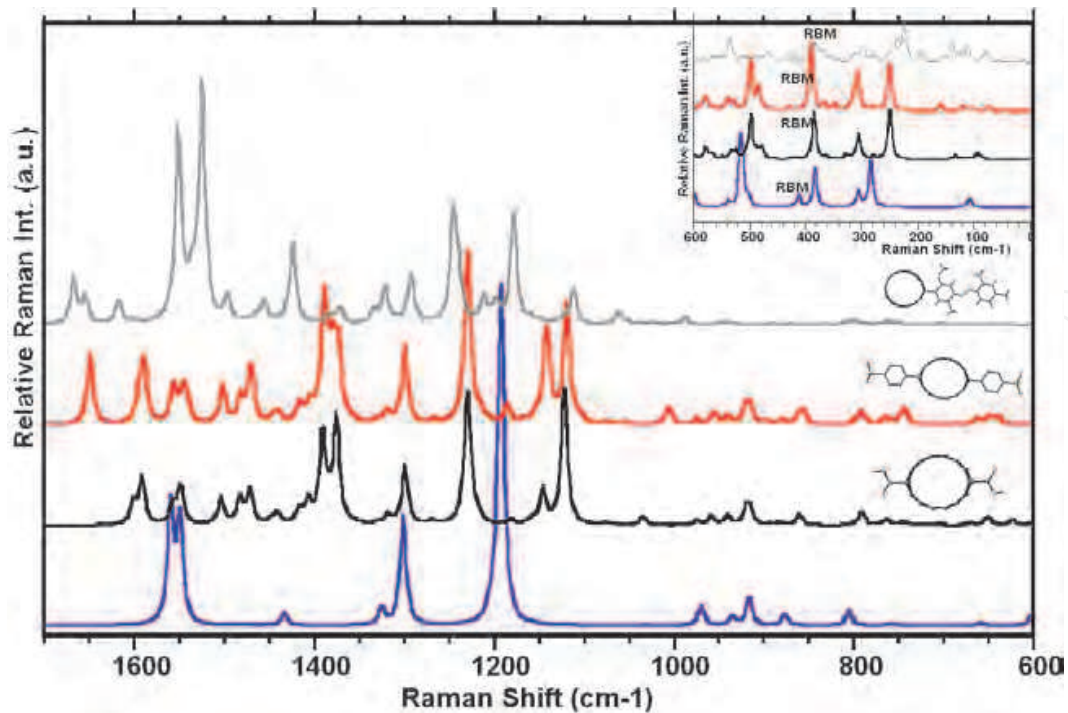


Fig. 3.7.1. Calculated Raman spectra of functionalized and isolated (7,0)-SWCNT.

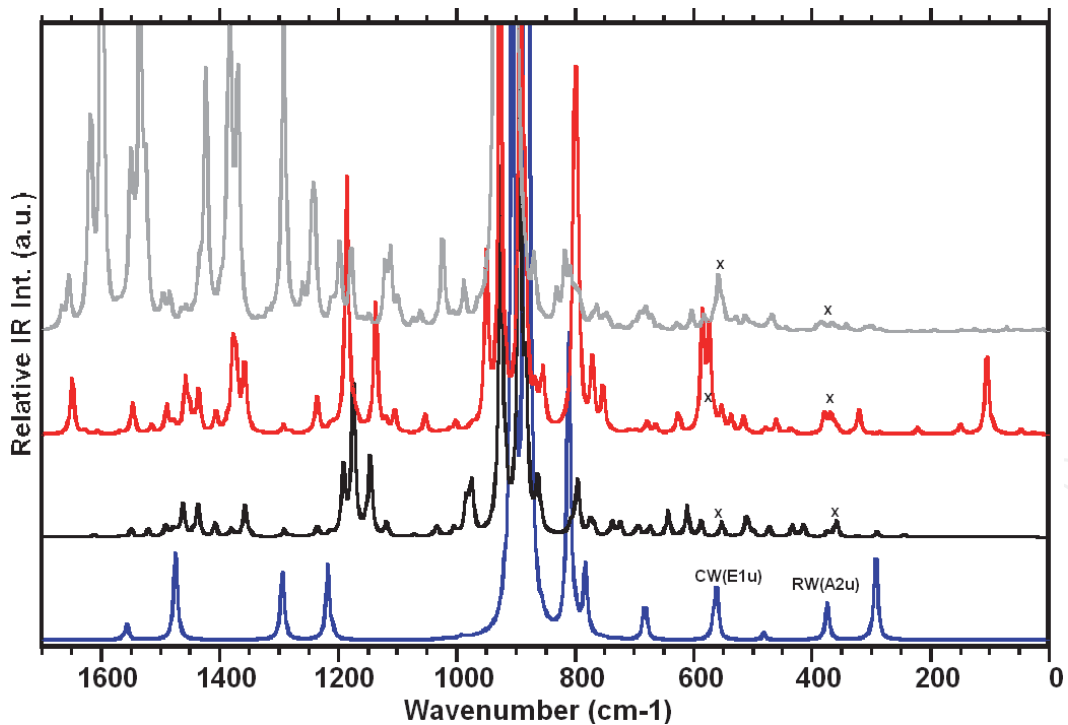


Fig. 3.7.2. Calculated IR spectra of functionalized and isolated (7,0)-SWCNT.

with the spectrum of the (7,0)-SWCNTs for comparison. As shown in the figure, there is slight shift in the peak positions, however, the relative intensities of specially G-, D- and RBM modes changed with the functional group, which is consistent with the experimental observations as discussed above. It should be pointed out that the calculated Raman spectrum was for the nonresonance case; however, the experimental measurements usually

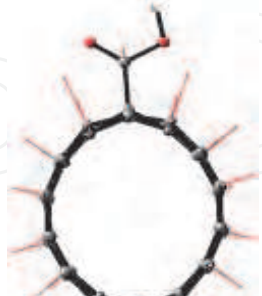
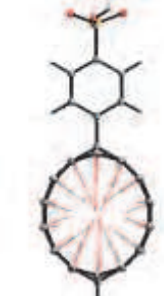
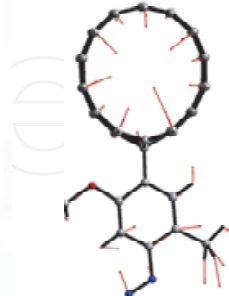
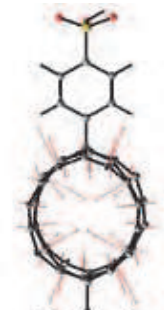
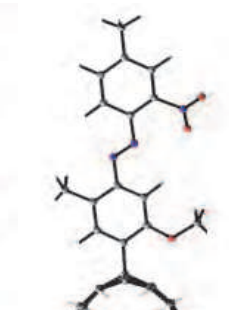
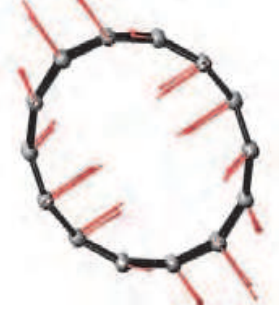
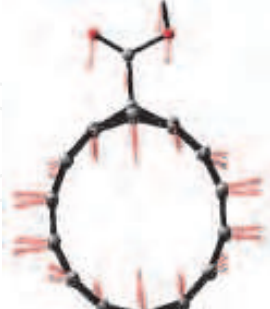
	(7,0)-SWCNT	carboxy (-CO ₂ H)- (7,0)-SWCNT	phenyl-SO ₃ H- (7,0)-SWCNT	3-methoxy-6-methyl-4- [(2-nitro-4-methylphenyl) azo] benzene- (7,0)-SWCNT
RBM(A_{1g})	 414.04	 385.78	 390.48	 385.82
BD(E_{1g})	 308.03	 306.27	 307.27	 311.05
ED(E_{2g})	 109.82	 95.26	 120.83	 111.98

Fig. 3.7.3. Calculated molecular motions for selected vibrational bands of the functionalized (7,0)-SWCNT and the calculated values of vibrational frequencies in cm⁻¹.

at the resonance case. Therefore, the relative intensities of corresponding peaks in the observed spectrum at the resonance may be expected to somewhat differ in intensity reference to their nonresonance spectrum. Figure 3.7.2 provides the calculated IR spectra of the functionalized (7,0)-SWCNT with these functional group. The IR spectra of these functionalized-CNT showed that the IR spectrum of isolated (7,0)-SWCNT differ than its functionalized structure. Figure 3.7.3 shows the vibrational motion for the selected vibrational modes of the frequency in low energy region.

The calculated electronic transitions of the functionalized (7,0)-SWCNT with various functional groups showed that the functionalized (7,0)-SWCNT produce many dipole allowed electronic transition in low energy region, while the isolated (7,0)-SWCNT exhibited only one allowed transition in the same region (see Table 3.7.1). The calculated dipole allowed vertical electronic transition for the 3-methoxy-6-methyl-4- [(2-nitro-4-methylphenyl) azo] benzene functionalized (7,0)-SWCNT (with the calculated electron densities in molecular orbitals as seen in Figure 3.7.4) suggested that there might be a charge transfer (CT) mechanism as result of the transitions from the HOMO of the SWCNT to the LUMO of the molecule.

HOMO(a)-1 HOMO(a) LUMO(a) LUMO(a)+1 HOMO(b) LUMO(b) LUMO(b)+1

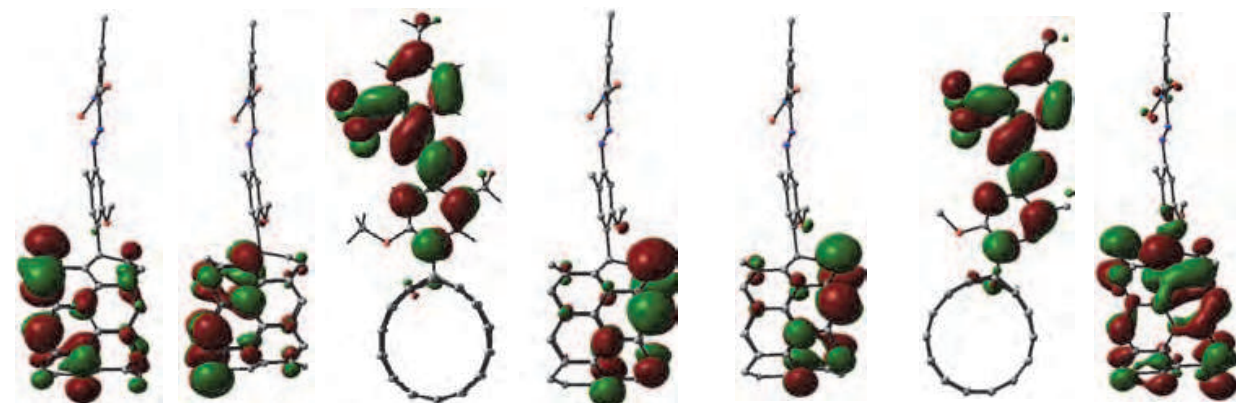


Fig. 3.7.4. Plot of the electron densities in the HOMOs and LUMOs for the 3-methoxy-6-methyl-4- [(2-nitro-4-methylphenyl) azo] benzene-(7,0)-SWCNT system.

Furthermore, we also calculated dipole allowed vertical electronic transitions for two of the 3-methoxy-6-methyl-4- [(2-nitro-4-methylphenyl) azo] benzene molecules covalently bonded to (7,0)-SWCNT, see Table 3.7.2. Figure 3.7.5 provides the calculated electron densities in molecular orbitals. The results of calculated dipole allowed vertical electronic transitions suggested that the $S_0 \rightarrow S_3$ transition is favorable candidate for the charge transfer from the (7,0)-SWCNT to the 3-methoxy-6-methyl-4- [(2-nitro-4-methylphenyl) azo] benzene molecule in consequence of the transitions from the highest occupied molecular orbital of the CNT to the lowest unoccupied molecular orbital of the 3-methoxy-6-methyl-4- [(2-nitro-4-methylphenyl) azo] benzene molecules as shown in Figure 3.7.5. It should be noted that the spin forbidden electronic transition ($S_0 \rightarrow T_2$; 0.728 eV) lies between the $S_0 \rightarrow S_2$ (0.766 eV) and $S_0 \rightarrow S_3$ (0.776) dipole allowed electronic transitions as seen in Table 3.7.2. This result indicates a possibility of the ISC process for this doubly functionalized (10,0)-SWCNT system.

0→n	H→L	CI	eV	f	0→n	H→L	CI	eV	f
0→1	H(b) →L(b)	0.29	1.30	0.0012	0→6	H(a) →L(a)	0.32	1.54	0.0011
	H(b) →L(b)+1	0.93				H(a) →L(a)+2	0.67		
0→2	H(b) →L(b)	0.94	1.44	0.0003	0→7	H(a)-1→L(a)	0.86	1.55	0.0021
	H(b) →L(b)+1	-0.28				H(a) →L(a)+2	0.28		
0→3	H(a)-1→L(a)+2	0.69	1.47	0.0030	0→8	H(a)-1→L(a)+1	0.80	1.56	0.0025
	H(b)-1→L(b)+3	0.16				H(a) →L(a)+2	0.50		
0→4	H(a) →L(a)	0.80	1.51	0.0008	0→9	H(a)-7→L(a)	0.64	1.57	0.0003
	H(a) →L(a)+1	0.54				H(a)-1→L(a)	0.38		
0→5	H(a) →L(a)	-0.47	1.52	0.0042	0→10	H(b) →L(b)+1	0.12	1.65	0.0055
	H(a) →L(a)+1	0.79				H(b) →L(b)+2	0.95		

Table 3.7.1. Calculated vertical doublet-doublet electronic transitions ($D_0 \rightarrow D_n$) energies and oscillator strengths (f) of the functionalized (7,0)-SWCNT at TD-B3LYP/6-31G(d,p) level of the theory. Where the functional group, 3-methoxy-6-methyl-4- [(2-nitro-4-methylphenyl) azo] benzene, is covalently bonded to the (7,0)-SWCNT (see Fig. 3.7.4). While the upper case letters H and L indicate the highest occupied molecular orbitals (HOMO) and the lowest unoccupied molecular orbitals (LUMO), respectively, the lower case letters (a) and (b) stand for the alpha and beta spin states, respectively. CI represents configurationally interaction coefficient.

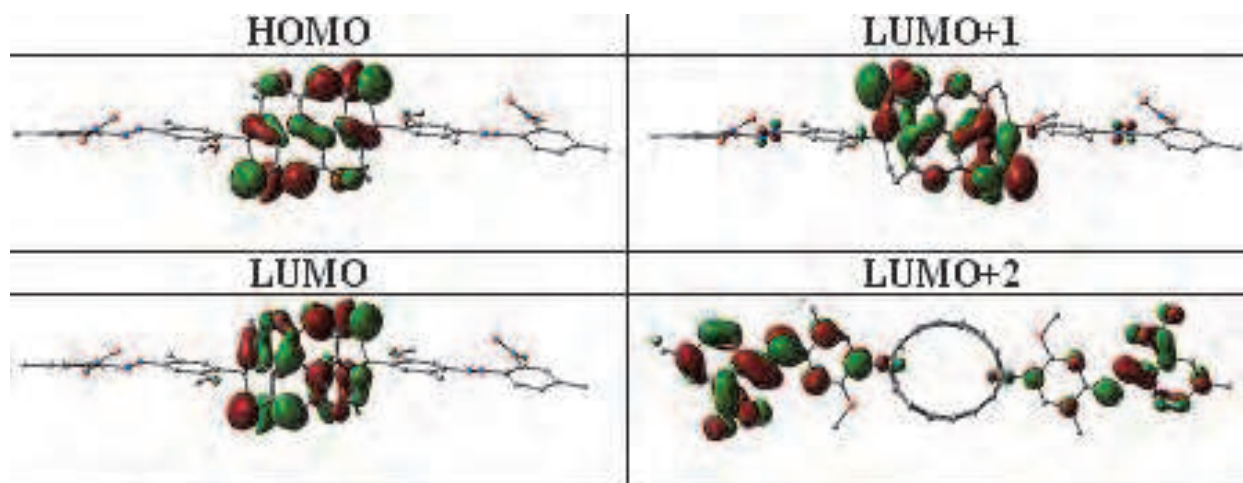


Fig. 3.7.5. Plot of the electron densities in the HOMOs and LUMOs for the 3-methoxy-6-methyl-4- [(2-nitro-4-methylphenyl) azo] benzene-(7,0)-SWCNT system.

We optimized the functionalized (10,0)-SWCNT, with four of the 3-methoxy-6-methyl-4- [(2-nitro-4-methylphenyl) azo] benzene molecules which covalently bonded to (10,0)-SWCNT. Because of the technique reason, we could not calculate the electronic transitions. However, when we plot the electron density in the molecular orbitals as seen in Figure 3.7.6, the HOMO, LUMO and LUMO+1 belongs to (10,0)-SWCNT, the molecular orbitals from

$S_0 \rightarrow S_n$	HOMO→LUMO	CI	eV	f	$S_0 \rightarrow T_n$	HOMO→LUMO	CI	eV
$S_0 \rightarrow S_1$	HOMO→LUMO+1	0.64	0.375		$S_0 \rightarrow T_1$	HOMO-1→LUMO	-0.15	0.174
$S_0 \rightarrow S_2$	HOMO→LUMO	0.36	0.766	0.0232		HOMO→LUMO+1	0.94	
	HOMO→LUMO+2	-0.23			$S_0 \rightarrow T_2$	HOMO-2→LUMO	0.13	0.728
$S_0 \rightarrow S_3$	HOMO→LUMO+2	0.65	0.776	0.0009		HOMO→LUMO+4	0.78	
	HOMO→LUMO+3	0.23			$S_0 \rightarrow T_3$	HOMO→LUMO+1	0.11	0.758
$S_0 \rightarrow S_4$	HOMO→LUMO	-0.29	0.810	0.0407		HOMO→LUMO+2	0.69	
	HOMO→LUMO+2	-0.10			$S_0 \rightarrow T_4$	HOMO→LUMO+3	0.69	0.775
	HOMO→LUMO+3	0.50				HOMO→LUMO+4	0.14	
$S_0 \rightarrow S_5$	HOMO-2→LUMO	-0.14	0.988	0.0070				
	HOMO→LUMO+4	0.63						
$S_0 \rightarrow S_6$	HOMO-1→LUMO	0.67	1.062					

Table 3.7.2. Calculated vertical singlet-singlet ($S_0 \rightarrow S_n$) and singlet-triplet ($S_0 \rightarrow T_n$) electronic transitions for two of the 3-methoxy-6-methyl-4- [(2-nitro-4-methylphenyl) azo] benzene molecule covalently bonded to (7,0)-SWCNT. Where The calculations were performed at TD-B3LYP/6-31G(d,p) level of the DFT. CI stands for configurationally interaction coefficient.

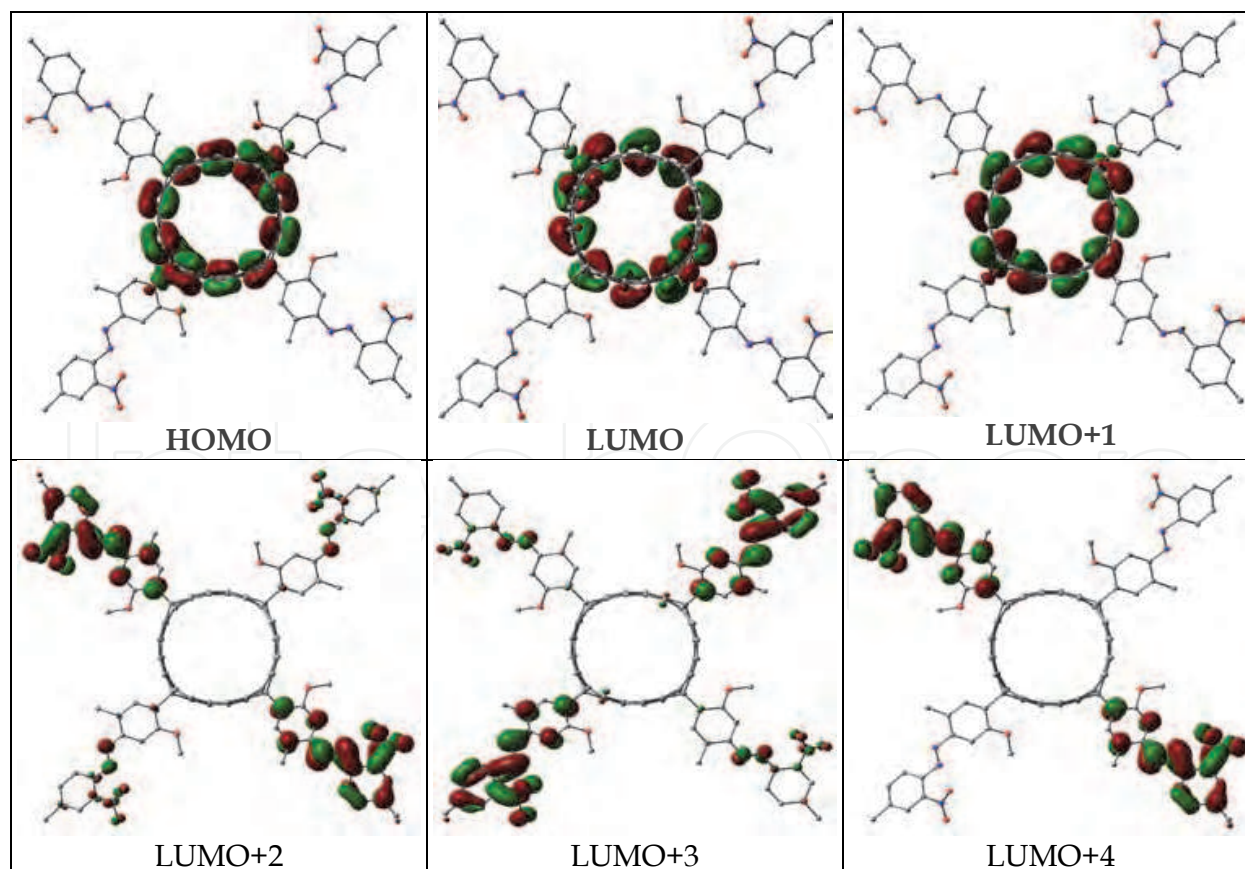


Fig. 3.7.6. Plot of the electron densities in the HOMOs and LUMOs for the 3-methoxy-6-methyl-4- [(2-nitro-4-methylphenyl) azo] benzene-(7,0)-SWCNT system.

LUMO+2 to LUMO+5 belongs to the 3-methoxy-6-methyl-4- [(2-nitro-4-methylphenyl) azo] benzene molecules. This results again suggested the charge transfer from the (10,0)-SWCNTs to the molecule in low energy region.

4. Acknowledgment

We wish to thank Dr. Abdullah Cavus, Dr. Nathan Stevens, and Miss Oya Onar for their assistance and suggestions in this work.

5. References

- [1] S. Iijima, *Nature*. 354 (1991) 56.
- [2] Nepal D, Sohn JI, Aicher WK, et al. *Biomacromolecules* 6(6) (2005) 2919.
- [3] Karajanagi SS, Yang HC, Asuri P, et al. *Langmuir*, 22(4) (2006) 1392.
- [4] Hod Finkelstein, Peter M. Asbeck, Sadik Esener, 3rd IEEE Conference on Nanotechnology (IEEE-NANO), vol.1, (2003) 441.
- [5] D.S. Wen, Y.L. Ding, *International Journal of Heat and Mass Transfer* 47 (2004) 5181.
- [6] H. Masuda, A. Ebata, K. Teramae, N. Hishiunma, *Netsu Bussei (Japan)* 4 (1993) 227.
- [7] Carissa S. Jones, Xuejun Lu, Mike Renn, Mike Stroder, and Wu-Sheng Shih. *Microelectronic Engineering*; DOI: 10.1016/j.mee.2009.05.034.
- [8] S.M. Jung, H.Y. Jung, J.S. Suh. *Sensors and Actuators B*. 139 (2009) 425.
- [9] T. Rueckes, K. Kim, E. Joselevich, G.Y. Tseng, C.L. Cheung and C.M. Lieber, *Science* 289 (2000) 94.
- [10] M. J. O'Connell *et al.*, *Science* 297 (2002) 593.
- [11] S. M. Bachilo, M. S. Strano, C. Kittrell, R. H. Hauge, R. E. Smalley, and R. B. Weisman, *Science* 298 (2002) 2361.
- [12] A. Hartschuh, H. N. Pedrosa, L. Novotny, and T. D. Krauss, *Science* 301 (2003) 1354.
- [13] J. Maultzsch, R. Pomraenke, S. Reich, E. Chang, D. Prezzi, A. Ruini, E. Molinari, M. S. Strano, C. Thomsen¹, and C. Lienau, *Phys. Stat. Sol. (b)* 243, No. 13 (2006) 3204.
- [14] E. Chang, G. Bussi, A. Ruini, and E. Molinari, *Phys. Rev. Lett.* 92 (2004) 196401.
- [15] C. D. Spataru, S. Ismail-Beigi, L. X. Benedict, and S. G. Louie, *Phys. Rev. Lett.* 92 (2004) 077402.
- [16] V. Perebeinos, J. Tersoff, and P. Avouris, *Phys. Rev. Lett.* 92 (2004) 257402.
- [17] Won-Il Park, Hun-Sik Kim, Soon-Min Kwon, Young-Ho Hong, Hyoung-Joon Jin, *Carbohydrate Polymers*. 77 (2009) 457.
- [18] Lingjie Meng, Chuanlong Fu, and Qinghua Lu, *Natural Science*, 19 (2009) 801.
- [19] C.T. Hsieh, Y.T. Lin, *Microporous Mesoporous Mater.* 93 (2006) 232.
- [20] Davis JJ, Coleman KS, Azamian BR, et al. *Chem Eur J.*, 9(16) (2003) 3732.
- [21] Poenitzsch VZ, Winters DC, Xie H, et al. *J Am Chem Soc*, 129(47) (2007) 14724.
- [22] H. Zhao and S. Mazumdar, *Phys. Rev. Lett.* 93 (2004) 157402.
- [23] C. L. Kane and E. J. Mele, *Phys. Rev. Lett.* 93 (2004) 197402.
- [24] T. Ando, *J. Phys. Soc. Jpn.* 66 (1997) 1066.
- [25] F. Wang, G. Dukovic, L. E. Brus, and T. F. Heinz, *Science* 308 (2005)838.

- [26] E. B. Barros, R.B. Capaz, A.Jorio, G.G. Samsonidze, A.G. Souza Filho, S. Ismail-Beigi, C. D. Spataru, S. G. Louie, G.Dresselhaus, and M.S. Dresselhaus," Phys. Rev. B 73 (2006) 241406.
- [27] H. Zhao , S. Mazumdar C.-X. Sheng, M. Tong, and Z. V. Vardeny, Phys. Rev. B 73 (2006) 075403.
- [28] H.Kishida, Y.Nagasawa, S.Imamura, and A.Nakamura, Phys Rev Lett 100 (2008) 097401.
- [29] N.G.Kalugin, Y.Rostovtsev, Opt.Lett.31, (2006) 969.
- [30] M. Jain, H.Xia, G. Y. Yin, A. J. Merriam, and S. E. Harris, Phys.Rev.Lett.77 (1996) 4326.
- [31] O.Kocharovskaya, Ya.I.Khanin, ZhETPh 90 (1986) 1610.
- [32] V.A.Sautenkov, Y.V.Rostovtsev, C.Y.Ye, G.R.Welch, O.Kocharovskaya, and M.O.Scully, Phys. Rev. A 71 (2005) 063804.
- [33] Elefterios Lidorikis and Andrea C. Ferrari, ACSNANO, 3(5) (2009) 1238.
- [34] Y. Wang, X. Wang, J. Rybczynski, D. Z. Wang, K. Kempa, and Z. F. Ren, Appl. Phys. Lett. 86 (2005) 153120.
- [35] Oliver Kiowski, Katharina Arnold, Sergei Lebedkin, Frank Hennrich, and Manfred M. Kappes, Phys. Rev. Lett. 99 (2007) 237402.
- [36] R. M. Russo, E. J. Mele, C. L. Kane, I. V. Rubtsov, M. J. Therien, and D. E. Luzzi, Phys. Rev. B 74 (2006) 041405.
- [37] J. Maultzsch, R. Pomraenke, S. Reich, E. Chang, D. Prezzi, A. Ruini, E. Molinari, M. S. Strano, C. Thomsen, and C. Lienau, Phys. Rev. B 72 (2005) 241402(R).
- [38] T. G. Pedersen, Phys. Rev. B 67 (2003) 073401.
- [39] T. Ogawa and T. Takagahara, Phys. Rev. B 44 (1991) 8138.
- [40] H. B. Zhao and S. Mazumdar, Phys. Rev. Lett. 93 (2004) 157402.
- [41] J Moreno, K Kasai, M David, H Nakanishi and H Kasai. *J. Phys. Condens. Matter*, 21 (2009) 064219.
- [42] B.K. Pradhan, A.R. Harutyunyan, D. Stojkovic, J.C. Grossman, P. Zhang, M.W. Cole, V. Crespi, H. Goto and J. Fujiwara., *J. Mater. Res.*,17(9) (2002).
- [43] P. Kim, L. Shi, A. Majumdar, and P.L. McEuen, *Phys. Rev. Lett.*, 87 (2001) 215502-1.
- [44] J. Hone, M. Whitney, C. Piskoti, and A. Zettl, *Phys. Rev. Lett. B.*, 59(4) (1999) R2514.
- [45] Motoo Fujii, Xing Zhang, Huaqing Xie, Hiroki Ago, Koji Takahashi, Tatsuya Ikuta,Hidekazu Abe, and Tetsuo Shimizu3, *Phys. Rev. Lett. B.* 95 (2005) 065502.
- [46] Quoc Ngo, Brett A. Cruden, Alan M. Cassell, Megan D. Walker, Qi Ye, Jessica E. Koehne, M. Meyyappan, Jun Li, and Cary Y. Yang, *Mat. Res. Soc. Symp. Proc.* 812 (2004) F3.18.1
- [47] G. S. Choi, K. H. Son, D. J. Kim, *Microelectronic Engineering*, 66(1/4) (2003) 206.
- [48] N.G. Chopra, et al., *Science*. 269 (1995) 966.
- [49] D. Golberg, Y. Bando, W. Han, K. Kurashima, T. Sato, *Chem. Phys. Lett.*, 308 (1999) 337.
- [50] C. C. Tang, Y. Bando, T. Sato, K. Kurashima, *Chem. Commun.* 12 (2002) 1290.
- [51] M. S. Dresselhaus, G. Dresselhaus, P. C. Eklund, *Science of Fullerenes and Carbon Nanotubes*, Academic Press, San Diego, CA (1996).
- [52] D. Zhang, R. Q. Zhang, *Chem. Phys. Lett.*, 371 (2003) 426.
- [53] M. Mirzaei, N. L. Hadipour, *Physica E*, 40 (2008) 800.

- [54] C.H. Park, C.D. Spataru, S.G. Louie, *Physical Review Letters* 96 (2006) 126105.
- [55] L. Wirtz, A. Marini, A. Rubio, *Physical Review Letters* 96 (2006) 126104.
- [56] A. Rubio, J.L. Corkill, M.L. Cohen, *Physical Review B* 49 (1994) 5081.
- [57] Chunyi Zhi, Yoshio Bando, Chengchun Tang, Dmitri Golberg *Materials Science and Engineering R* 70 (2010) 92.
- [58] X. Blase, A. Rubio, S.G. Louie, M.L. Cohen, *Europhysics Letters* 28 (1994) 335.
- [59] C.Y. Won, N.R. Aluru, *Journal of the American Chemical Society* 129 (2007) 2748.
- [60] G. Mpourmpakis, G.E. Froudakis, *Catalysis Today* 120 (2007) 341.
- [61] Z. Zhou, J.J. Zhao, Z.F. Chen, X.P. Gao, T.Y. Yan, B. Wen, P.V. Schleyer, *Journal of Physical Chemistry B* 110 (2006) 13363.
- [62] X.J. Wu, J.L. Yang, J.G. Hou, Q.S. Zhu, *Journal of Chemical Physics* 124 (2006) 54706.
- [63] J.R. Cheng, R. Ding, Y. Liu, Z.F. Ding, L.B. Zhang, *Computational Materials Science* 40 (2007) 341.
- [64] I. Cabria, M.J. Lopez, J.A. Alonso, *Nanotechnology* 17 (2006) 778.
- [65] E. Durgun, Y.R. Jang, S. Ciraci, *Physical Review B* 76 (2007) 073413.
- [66] S.H. Jhi, D.J. Roundy, S.G. Louie, M.L. Cohen, *Solid State Communications* 134 (2005) 397.
- [67] G.Y. Gou, B.C. Pan, L. Shi, *Journal of the American Chemical Society* 131 (2009) 4839.
- [68] R.Q. Wu, L. Liu, G.W. Peng, Y.P. Feng, *Applied Physics Letters* 86 (2005) 122510.
- [69] F. Lii, Z.H. Zhu, M.W. Zhao, Y.Y. Xia, *Journal of Physical Chemistry C* 112 (2008) 16231.
- [70] F. Li, Z.G. Zhu, X.D. Yao, G.Q. Lu, M.W. Zhao, Y.Y. Xia, Y. Chen, *Applied Physics Letters* 92 (2008) 102515.
- [71] J.B. Wu, W.Y. Zhang, *Chemical Physics Letters* 457 (2008) 169.
- [72] J.B. Wu, W.Y. Zhang, *Solid State Communications* 149 (2009) 486.
- [73] G. Rahman, S.C. Hong, *Journal of Nanoscience and Nanotechnology* 8 (2008) 4711.
- [74] L. Wang, J. Lu, L. Lai, W. Song, M. Ni, Z.X. Gao, W.N. Mei, *Journal of Physical Chemistry C* 111 (2007) 3285.
- [75] P. Saxena, S.P. Sanyal, *Physica E* 24 (2004) 244.
- [76] I. Savic, N. Mingo, D.A. Stewart, *Physical Review Letters* 101 (2008) 165502.
- [77] G.Y. Gou, B.C. Pan, L. Shi, *Journal of Physical Chemistry C* 112 (2008) 19353.
- [78] J. Song, J. Wu, Y. Huang, K.C. Hwang, *Nanotechnology* 19 (2008) 445705.
- [79] J.T. Tanskanen, M. Linnolahti, A.J. Karttunen, T.A. Pakkanen, *Chemphyschem* 9 (2008) 2390.
- [80] J.W. Kang, H.J. Hwang, *Journal of Physics* 16 (2004) 3901.
- [81] C.Y. Won, N.R. Aluru, *Journal of Physical Chemistry C* 112 (2008) 1812.
- [82] X.Y. Li, W. Yang, B. Liu, *Nano Letters* 7 (2007) 3709.
- [83] W.H. Moon, H.J. Hwang, *Materials Letters* 58 (2004) 2331.
- [84] V. Meunier, C. Roland, J. Bernholc, M.B. Nardelli, *Applied Physics Letters* 81 (2002) 46.
- [85] M.D. Ganji, A. Mohammadi-Nejad, *Physics Letters A* 372 (2008) 4839.
- [86] F.W. Zheng, G. Zhou, Z.R. Liu, J. Wu, W.H. Duan, B.L. Gu, S.B. Zhang, *Physical Review B* 78 (2008) 205415.
- [87] M. Ishigami, J.D. Sau, S. Aloni, M.L. Cohen, A. Zettl, *Physical Review Letters* 97 (2006) 176804.

- [88] J. Zhang, K.P. Loh, M. Deng, M.B. Sullivan, J.W. Zheng, P. Wu, *Journal of Applied Physics* 99 (2006) 104309.
- [89] K.S. Ryu, Y.I. Kim, J.K. Jung, Y. Chen, C.H. Lee, *Journal of Nanoscience and Nanotechnology* 8 (2008) 5193.
- [90] Z. Zhou, J. Zhao, Z. Chen, X. Gao, T. Yan, B. Wen, P.V.R. Schleyer, *Journal of Physical Chemistry B* 110 (2006) 13363.
- [91] M.B. Belonenko, N.G. Lebedev, *Technical Physics* 54 (2009) 338.
- [92] Saito R, et al., *Physical Properties of Carbon Nanotubes*. Imperial College Press, London; 1998
- [93] L. Yang, M. P. Anantram, J. Han, and J. P. Lu, *Physical Review B*, vol. 60, (1999) 13874.
- [94] Gaussian, Inc., Carnegie Office Park-Bulding 6, Pittsburgh, PA106, USA.
- [95] (a) C. Guo, M. Aydin, H. R. Zhu, D. L. Akins, *J. Phys. Chem. B* 106 (2002) 5447; (b) H, Guo, X. Zhang, M. Aydin, W. Xu, H. R. Zhu, D. L. Akins, *Journal of Molecular Structure* 689 (2004) 153; (c) M. Aydin, F. Jean-Mary, N. Stevens, D. L. Akins, *J. Phys. Chem. B* 108(2004) 9695; (d) W. Xu, M. Aydin, S. Zakia, D. L. Akins, *J. Phys. Chem. B* 108 (2004) 5588; (e) M. Aydin, J. R. Lombardi, *J. Phys. Chem. A* 113 (2009) 2809; (f) Metin Aydin, *Photofragmentation Spectroscopy*. VDM Publishing House Ltd., 2009.
- [96] R. Pfeiffer, F. Simon, H. Kuzmany, and V. N. Popov, *Phys. Rev. B* 72 (2005) 161404(R).
- [97] A. Lan, Y. Zhang, X. Zhang, Z. Iqbal, H. Grebel, *Chem. Physics Lett.* 379 (2003) 395.
- [98] Blase X, Rubio A, Louie S and Cohen M L *Europhys. Lett.* 28 (1994) 335
- [99] R Chowdhury, C Y Wang, S Adhikari and F Scarpa *Nanotechnology* 21 (2010) 365702
- [100] Chopra N, Luyken R, Cherrey K, Crespi V, Cohen M, Louie S and Zettl A *Science* 269 (1995) 966.
- [101] Golberg D, Bando Y, Tang C and Zhi C *Adv. Mater.* 19 (2007) 2413-32
- [102] Won C Y and Aluru N R *J. Phys. Chem. C* 112 (2008) 1812.
- [103] Santosh M, Maiti P K and Sood A K *J. Nanosci. Nanotechnol.* 9 (2009) 5425.
- [104] Yuan J and Liew K M *Nanotechnology* 19 (2008) 445703
- [105] Zhi C Y, Bando Y, Tang C C, Huang Q and Golberg D *J. Mater. Chem.* 18 (2008) 3900.
- [106] Oh E S *Mater. Lett.* 64 (2010) 859.
- [107] Xu F, Bando Y, Golberg D, Ma R, Li Y and Tang C *J. Chem. Phys.* 119 (2003) 3436.
- [108] Moon W H and Hwang H J *Physica E* 23 (2004) 26.
- [109] Verma V, Jindal V K and Dharamvir K *Nanotechnology* 18 (2007) 435711
- [110] Song J, Wu J, Huang Y and Hwang K C *Nanotechnology* 19 (2008) 445705
- [111] Suryavanshi A, Yu M, Wen J, Tang C and Bando Y *Appl. Phys. Lett.* 84 (2004) 2527.
- [112] Chopra N and Zettl A *Solid State Commun.* 105 (1998) 297.
- [113] Zhi C, Bando Y, Tang C, Honda S, Kuwahara H and Golberg D *J. Mater Res.* 21 (2006) 2794.
- [114] Huang Q, Bando Y, Xu X, Nishimura T, Zhi C, Tang C, Xu F, Gao L and Golberg D *Nanotechnology* 18 (2007) 485706.
- [115] M. Aydin and L. Akins *Vib. Spectrosc.* 53 (2010) 163.

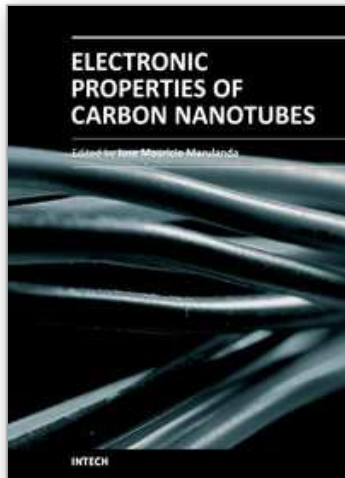
- [116] Sanchez-Portal D and Hernandez E *Phys. Rev. B* 66 (2002) 235415
- [117] Wirtz L and Rubio A *IEEE Trans. Nanotechnol.* 2 (2003) 341.
- [118] Akdim B, Pachter R, Duan X F and Adams W W *Phys. Rev. B* 67 (2003) 245404
- [119] Zhang Z H, Guo W L and Dai Y T *J. Appl. Phys.* 105 (2009) 084312
- [120] Jensen K, Kim K and Zettl A *Nat. Nanotechnol.* 3 (2008) 533
- [121] Chowdhury R, Adhikari S and Mitchell J *Physica E* 42 (2009) 104
- [122] Li C Y and Chou T W *Appl. Phys. Lett.* 84 (2004) 5246–8
- [123] Chang, J.; Cañamares, M. V.; Aydin, M.; Vetter, W.; Schreiner, M.; Xu, W. ve Lombardi, J. R., *Journal of Raman Spect.*, 40 (2009) 1557.
- [124] Shankar Ghosh, Pallavi V. Teredesai, and A. K. Sood *Pure Appl. Chem.*, 74 (9) (2002) 1719.
- [125] P. Delaney, H. J. Choi, I. Ihm, S. G. Louie, M. L. Cohen. *Nature (London)* 391 (1998) 466.
- [126] C. S. Sunder, P. Ch. Sahu, V. S. Sastry, G. V. N. Rao, V. Sridharan, M. Premila, A. Bharathi, Y. Hariharan, T. S. Radhakrishnan, D. V. S. Muthu, A. K. Sood. *Phys. Rev. B* 53 (1996) 8180.
- [127] M. J. Peters, L. E. McNeil, J. P. Lu, D. Kahn. *Phys. Rev. B* 61 (2000) 5939.
- [128] A.S. Barnard, I.K. Snook, S.P. Russo, *Journal of Materials Chemistry* 17 (2007) 2892.
- [129] Y.M. Chou, H.W. Wang, Y.J. Lin, W.H. Chen, B.C. Wang, *Diamond and Related Materials* 18 (2009) 351.
- [130] A.V. Osadchy, E.D. Obraztsova, S.V. Terekhov, V.Y. Yurov, *Journal of Theoretical Physics Letters* 77 (2003) 405.
- [131] G.Y. Guo, S. Ishibashi, T. Tamura, K. Terakura, *Physical Review B* 75 (2007) 245403.
- [132] X.M. Li, W.Q. Tian, X.R. Huang, C.C. Sun, L. Jiang, *Journal of Nanoparticle Research* 11 (2009) 395.
- [133] K.H. Khoo, M.S.C. Mazzoni, S.G. Louie, *Physical Review B* 69 (2004) 201401.
- [134] C. Attacalite, L. Wirtz, A. Marini, A. Rubio, *Physica Status Solidi B* 244 (2007) 4288.
- [135] C.W. Chen, M.H. Lee, S.J. Clark, *Nanotechnology* 15 (2004) 1837.
- [136] S.L. Hu, Z.Y. Li, X.C. Zeng, J.L. Yang, *Journal of Physical Chemistry C* 112 (2008) 8424.
- [137] C.H. Park, S.G. Louie, *Nano Letters* 8 (2008) 2200.
- [138] H.P. Lan, L.H. Ye, S.A. Zhang, L.M. Peng, *Applied Physics Letters* 94 (2009) 183110.
- [139] Z.G. Wang, Z. Li, D.M. Cheng, *European Physical Journal* 46 (2009) 20601.
- [140] R.J. Baierle, T.M. Schmidt, A. Fazzio, *Solid State Communications* 142 (2007) 49.
- [141] R.X. Wang, R.X. Zhu, D.J. Zhang, *Chemical Physics Letters* 467 (2008) 131.
- [142] L. Lai, W. Song, J. Lu, Z.X. Gao, S. Nagase, M. Ni, W.N. Mei, J.J. Liu, D.P. Yu, H.Q. Ye, *Journal of Physical Chemistry B* 110 (2006) 14092.
- [143] Y.F. Li, Z. Zhou, D. Golberg, Y. Bando, P.V. Schleyer, Z.F. Chen, *Journal of Physical Chemistry C* 112 (2008) 1365.
- [144] P.N. Dpsilyachkov, D.V. Makaev, *Journal of the Physics and Chemistry of Solids* 70 (2009) 180.
- [145] T.M. Schmidt, R.J. Baierle, P. Piquini, A. Fazzio, *Physical Review B* 67 (2003) 113407.

- [146] Y.F. Li, Z. Zhou, J. Zhao, *Journal of Chemical Physics* 127 (2007) 184705.
- [147] Z.H. Zhang, W.L. Guo, *Journal of the American Chemical Society* 131 (2009) 6874.
- [148] Z. Zhou, J.J. Zhao, Z.F. Chen, P.V. Schleyer, *Journal of Physical Chemistry B* 110 (2006) 25678.
- [149] J. Zhang, K.P. Loh, P. Wu, M.B. Sullivan, J.W. Zheng, *Journal of Physical Chemistry C* 112 (2008) 10279.
- [150] V.A. Margulis, E.E. Muryumin, E.A. Gaiduk, *Physical Review B* 78 (2008) 035415.
- [151] H.T. Liu, G. Zhou, Q.M. Yan, J. Wu, B.L. Gu, W.H. Duan, D.L. Zhao, *Physical Review B* 75 (2007) 125410.
- [152] S. Okada, S. Saito, A. Oshiyama, *Physical Review B* 65 (2002) 165410.
- [153] Tretiak, S. *Nano Lett.*, 7(8) (2007) 2201.
- [154] Gambetta, A.; Manzoni, C.; Menna, E.; Meneghetti, M.; Cerullo, G.; Lanzani, G.; Tretiak, S.; Piryatinski, A.; Saxena, A.; Martin, R. L.; and Bishop, A. R. *Nature Phys.*, 2 (2006) 515.
- [155] Korovyanko, O. J.; Sheng, C. X.; Vardeny, Z. V.; Dalton, A. B.; and Baughman, R. H. *Phys. Rev. Lett.*, 92 (2004) 017403.
- [156] Capaz, R. B.; Spataru, C. D.; Ismail-Beigi, S.; and Louie, S. G. *Phys. Rev. B* 74 (2006) 121401.
- [157] Shim, M.; Javey, A.; Kam, N. W. S.; Dai, H. *J. Am. Chem. Soc.* 123 (2001) 11512.
- [158] Kong, J.; Franklin, N.; Zhou, C.; Chapline, M.; Peng, S.; Cho, K.; Dai, H. *Science* 287 (2000) 622.
- [159] Moonsub Shim, Nadine Wong Shi Kam, Robert J. Chen, Yiming Li, and Hongjie Dai *Nano Lett.*, Vol. 2, No. 4, (2002)
- [160] Ambarish Paul and Baidurya Bhattacharya, *Materials and Manufacturing Processes*, 25 (2010) 891
- [161] Lacerda L, Bianco A, Prato M and Kostarelos K *Adv. Drug Deliv. Rev.* 58 (2006) 1460
- [162] Bianco A, Kostarelos K and Prato M *Expert Opin. Drug Deliv.* 5 (2008) 331
- [163] Wang J and Lin Y H *TRAC Trends Anal. Chem.* 27 (2008) 619.
- [164] Gannon C J *et al Cancer* 110 (2007) 2654
- [165] Vyalikh A *et al Nanomedicine* 3 (2008) 321
- [166] Liu Z *et al Cancer Res.* 68 (2008) 6652
- [167] Lu Q *et al Nano Lett.* 4 (2004) 2473
- [168] Kam N W and Dai H *J. Am. Chem. Soc.* 127 (2005) 6021
- [169] Kam N W S, Liu Z A and Dai H *J Angew. Chem. Int. Edn* 45 (2006) 577
- [170] Lacerda L, Raffa S, Prato M, Bianco A and Kostarelos K *Nano Today* 2 (2007) 38
- [171] Kostarelos K *et al Nat. Nanotechnol.* 2 (2007) 108
- [172] Becker M L *et al Adv. Mater.* 19 (2007) 939
- [173] C Lamprecht, I Liashkovich, V Neves, J Danzberge, E Heiste, M Rangl, H M Coley, J McFadden, E Flahaut, H J Gruber, P Hinterdorfe, F Kienberge and A Ebne *Nanotechnology* 20 (2009) 434001
- [174] M. Müller, J. Maultzsch, D. Wunderlich, A. Hirsch, and C. Thomsen *phys. stat. sol. (b)* 244, No. 11, (2007), 4056.

- [175] Christie M. Sayes, Feng Liang, Jared L. Hudsona, Joe Mendez, Wenhua Guob, Jonathan M. Beach, Valerie C. Moore, Condell D. Doyle, Jennifer L. West, W. Edward Billups, Kevin D. Ausman, Vicki L. Colvin. *Toxicology Letters* 161 (2006) 135.

IntechOpen

IntechOpen



Electronic Properties of Carbon Nanotubes

Edited by Prof. Jose Mauricio Marulanda

ISBN 978-953-307-499-3

Hard cover, 680 pages

Publisher InTech

Published online 27, July, 2011

Published in print edition July, 2011

Carbon nanotubes (CNTs), discovered in 1991, have been a subject of intensive research for a wide range of applications. These one-dimensional (1D) graphene sheets rolled into a tubular form have been the target of many researchers around the world. This book concentrates on the semiconductor physics of carbon nanotubes, it brings unique insight into the phenomena encountered in the electronic structure when operating with carbon nanotubes. This book also presents to reader useful information on the fabrication and applications of these outstanding materials. The main objective of this book is to give in-depth understanding of the physics and electronic structure of carbon nanotubes. Readers of this book should have a strong background on physical electronics and semiconductor device physics. This book first discusses fabrication techniques followed by an analysis on the physical properties of carbon nanotubes, including density of states and electronic structures. Ultimately, the book pursues a significant amount of work in the industry applications of carbon nanotubes.

How to reference

In order to correctly reference this scholarly work, feel free to copy and paste the following:

Metin Aydin and Daniel Akins (2011). Geometric and Spectroscopic Properties of Carbon Nanotubes and Boron Nitride Nanotubes, *Electronic Properties of Carbon Nanotubes*, Prof. Jose Mauricio Marulanda (Ed.), ISBN: 978-953-307-499-3, InTech, Available from: <http://www.intechopen.com/books/electronic-properties-of-carbon-nanotubes/geometric-and-spectroscopic-properties-of-carbon-nanotubes-and-boron-nitride-nanotubes>

INTECH
open science | open minds

InTech Europe

University Campus STeP Ri
Slavka Krautzeka 83/A
51000 Rijeka, Croatia
Phone: +385 (51) 770 447
Fax: +385 (51) 686 166
www.intechopen.com

InTech China

Unit 405, Office Block, Hotel Equatorial Shanghai
No.65, Yan An Road (West), Shanghai, 200040, China
中国上海市延安西路65号上海国际贵都大饭店办公楼405单元
Phone: +86-21-62489820
Fax: +86-21-62489821

© 2011 The Author(s). Licensee IntechOpen. This chapter is distributed under the terms of the [Creative Commons Attribution-NonCommercial-ShareAlike-3.0 License](#), which permits use, distribution and reproduction for non-commercial purposes, provided the original is properly cited and derivative works building on this content are distributed under the same license.

IntechOpen

IntechOpen